Monte Carlo Simulations for Neutron Shielding in Radiotherapy Bunkers

Rafael A. Khatchadourian

Master of Science

Medical Physics Unit

McGill University

Montreal, Quebec

April 2013

A thesis submitted to McGill University in partial fulfilment of the requirements of the degree of Master of Science in Medical Radiation Physics

This thesis took an additional six months to complete. At times when it felt like a a never-ending story, I would remember a quote from Prof. Bielajew: "Old age happens when you dwell more on the past than on the future." By this definition, I had at least the consolation of having found eternal youth insofar as this thesis was concerned ;)

Abstract

Photoneutrons generated in the linac head are a byproduct of the radiotherapy process and can be potentially harmful to clinical personnel. The lack of accuracy associated with analytical photoneutron shielding methods has generated much interest in the Monte-Carlo (MC) method as a more flexible and precise tool for radiotherapy bunker design.

The purpose of this work was to use MC simulations to characterize photoneutron fluence, dose, and spectrum throughout various radiotherapy bunker configurations and for various room design features, such as the presence of a maze, a bulkhead, and the addition of borated polyethylene on the maze walls. Three existing rooms at the MUHC and two hypothetical doorless rooms were modelled with the MCNP5 code and using the Visual Editor GUI. The analytical spectrum of an 18 MV linac served as the point source of photoneutrons and was surrounded with a 10 cm radius tungsten sphere placed 100 cm above the isocenter. The next-event estimator variance reduction technique was used and simulations were performed with 20 million particle histories yielding uncertainties under 1%.

Physical measurements were also attempted with bubble detectors and a ^{3}He neutron spectrometer. The latter was unsuccessful because of pulse pile-up caused by the Linac's pulsed mode of operation, whereas the former gave us qualitative information on neutron equivalent dose distribution in the maze and around the linac.

Simulation results showed a marked decrease in neutron equivalent dose near the bunker entrance when maze walls are lined with BPE and when a bulkhead is added in the inner maze passage. It was found that the high thermal neutron cross-section of BPE was key in reducing the portion of thermal photoneutrons in the spectrum along the maze. The bulkhead was also useful in reducing photoneutron fluence entering the maze and hence reducing overall photoneutron dose near the entrance of the bunker.

Future work will focus on validating simulations with accurate physical measurements and refining the MC code to make it more user friendly and flexible in reproducing bunker geometry.

Résumé

Les photoneutrons générés par le linac sont un produit secondaire de la radiothérapie et peuvent être nuisibles au personnel médical. Le manque de précision des équations analytiques pour le blindage contre les photoneutrons a accéléré le développement des méthodes Monte-Carlo (MC), qui sont considérées plus flexibles et précises pour le design des salles de radiothérapie.
L'objectif de cette étude est d'utiliser les simulations MC afin de caractériser le flux, la dose, et le spectre des photoneutrons pour différentes configurations de salles de radiothérapie, telles que la présence d'un corridor, d'un bloc d'atténuation, et l'addition de borate de polyéthyléne sur les murs du corridor. Trois chambres du MUHC et deux chambres hypothétiques ont été modélisées avec le code MCNP5 et le logiciel Visual Editor. Le spectre d'énergie analytique d'un linac opérant à 18 MV a été utilisée comme source ponctuelle de photoneutrons. Ce point est entouré d'une sphére de Tungsténe de 10 cm de rayon positionnée 100 cm au dessus de l'isocentre. L'estimateur du prochain événement est la technique de réduction de variance qui a été utilisée et les simulations ont été effectuées avec 20 millions de particules résultant en des incertitudes inférieures à 1%.
Des mesures physiques ont aussi été tentées à l'aide de compteurs à bulles et un spectrométre de neutrons à ^{3}He. Ce dernier n'a pas eu de succés à cause de l'effet d'accumulation du signal pulsé. Les tests avec compteurs de bulles ont permis d'avoir une idée qualitative sur la distribution de la dose équivalente dans le corridor et autour du linac.

Les résultats des simulations ont montré une diminution de la dose équivalente de neutron prés de l'entrée de la chambre quand les murs du corridor sont couverts de borate de polyéthyléne et quand un bloc d'atténuation est présent dans le passage de la chambre centrale vers le corridor. Il a été confirmé que la haute probabilité d'interaction des neutrons de basses énergies avec le borate de polyéthyléne est essentiel à la réduction de la portion de photoneutrons à basses énergies à travers le corridor. Le bloc atténuateur contribue aussi à la réduction du flux de photoneutrons entrant dans le corridor et réduit ainsi la dose totale à l'entrée de la chambre.

La suite des travaux vise à mettre l'emphase sur la validation des simulations à l'aide de mesures expérimentales et sur le perfectionnement du code MC pour donner plus de flexibilité à l'utilisateur dans la reproduction des salles de radiothérapie.

Acknowledgements

First of all, I would like to thank my direct supervisor, Dr. John Kildea for providing me with intellectual guidance in all stages of this work, for sharing with me his enthusiasm for science, and of course for his patience! It was a pleasure working with you John.

Many thanks go to my co-supervisor Michael Evans who was instrumental in the realization of this project with his in depth knowledge of all matters related to health physics. I would also like to thank the CNSC for its financial support and the valuable training it offered me throughout this work.

This project was the result of a collaboration between scientists, clinicians, as well as institutions. Special thanks go to Angel Licea from the CNSC who introduced me to MCNP and taught me the code in the context of shielding design. Suffice it to say that the project would not have succeeded without him. Similarly, Dr. Stephen Davis from the MUHC was key in all matters related to the Monte-Carlo simulations. His experience in, and knowledge of, Monte-Carlo theory and the related software aspects were extremely helpful.

I am grateful to Prof. Leo Nikkinen from the physics department for lending us his spectrometer with all of the electronic equipment. Additional thanks must be included for guiding us in the entire process of making it work through numerous tests, discussions, and road trips. I thank Dr. Francois DeBlois from the JGH for giving us access to his bubble counting software, and Pierre Leger from the MUHC for giving us his oscilloscope. I would also like to thank Yani Picard from the CNSC for helping us with spectrometer and bubble detector calibration.

I am especially grateful to active faculty members Prof. Jan Seuntjens and Prof. Issam El Naqa, as well as to the clinical physics team, for everything they taught me during these two years. I learned much from you and from your example. Also, thank you William Parker for letting me attend Tuesday afternoon clinical meetings.

Warm regards to my fellow student colleagues who became friends. Special regards go to Sangkyu, Pavlos, Pete, Tanner, and Desmond for all the memorable moments and laughs we had, whether it was at the office or in a car during fourteen hour road trips.

I'm very grateful to Areni for her moral support during the challenging first year. Finally, and most importantly, I am forever indebted to my mother, my grandmother, and my brother for having always stood by me.

Contents

List of Figures

List of Tables

Chapter 1
Introduction

1.1 Context and structure of thesis

Cancer is one of the leading causes of death in the world and especially in developed countries. About 186 400 new cases of cancer and 75 700 deaths from cancer occurred in Canada in 2012 [1] [2] with over half of the cases being lung, colorectal, prostate, and breast cancers. Age is the main risk factor of cancer with 69% of new cases and 62% of deaths occurring in the 50 to 79 year age group [1]. Although increases in the number of new cancer cases in Canada are due mainly to a growing and aging population, the distribution of cancer incidence by tumour type - and consequently the distribution of corresponding treatments - varies through time. Thus, specific trends such as relatively large increases for liver and thyroid cancer or decreases of larynx and cervix uteri cancers can be observed [2].

During their treatment, about 50% of all cancer patients will undergo some sort of radiotherapy [3], which involves the use of ionizing radiation to shrink tumours and kill cancer cells by damaging their DNA. This is most often accomplished with the use of linear accelerators (linacs) that generate photon and electron beams to destroy tumours in a technique known as external beam radiotherapy (EBRT).

Linacs can generate radiation beams of different energies and can take different forms associated to special techniques such as Tomotherapy or Cyberknife [4]. Most radiotherapy today is performed at megavoltage (MV) energies with photons (X-rays). The patient lies on a couch and the linac is moved to irradiate the target according to specifications of the treatment plan, which is essentially a set of instructions on how the linac should deliver radiation. Modern treatment planning optimizes the coordination of the radiation delivery sequence with beam collimation and allows for the delivery of high doses to the target volume with a steep fall-off of the dose to adjacent healthy organs [4]. This is increasingly achieved with dynamic multi-leaf collimators (MLC), which are able to shape the photon beam into a variety of forms and thus minimize healthy tissue exposure in a technique known as intensity modulated radiation therapy (IMRT). Other techniques such as stereotactic radiosurgery (SRS) may use fixed-size collimators that limit beam size to the millimetre range.

Although modern EBRT is based on mature technologies that yield precise and accurate results and gain in sophistication year after year, their use still presents a number of technical challenges to medical and health physicists. A major problem stems from the fact that the radiation that destroys tumours and saves lives, can also cause negative side effects for the patient and even cause cancer, the very disease it is meant to eradicate. One reason for this is that as the electron beam is converted into a photon beam, a portion of the radiation is lost to the surroundings exposing various sections of the room, the patient's body, or the clinical personnel to unintended ionizing radiation. This is the reason sophisticated shielding methods have been developed to isolate the patient and the medical personnel from radiation.

EBRT is executed in special rooms known as *bunkers*, which are specifically designed to minimize all unintended radiation from leaving the radiotherapy room and affect the clinical personnel or the public. Given the potential impact on public health, bunker configuration is achieved by following clear and stringent guidelines from national or international regulatory organizations (CNSC, IAEA, ICRP, NCRP) that deal with radiation protection. Thanks to shielding theory and recommendations summarized in publications from these groups [5], bunker design is a well understood branch of medical physics, where research focuses on optimizing the configuration of the room with increasingly sophisticated tools. One such tool is the Monte-Carlo (MC) stochastic simulation technique which is the gold standard in radiotherapy dose calculations and is gaining acceptance as the method of choice for deriving shielding quantities. This is in clear contrast with most of the existing literature based on deterministic models [5] [6] that often lack accuracy for specific types of radiation such as neutrons. Indeed, because of their uncharged nature and high ionizing potential, neutrons (or more precisely *photoeneutrons* as they are known in the context of radiation therapy) represent a challenge for radiation protection professionals and their transport is better explained and modelled using numerical methods than analytical equations [7].

It is in this context that we decided to apply MC simulations for neutron shielding calculations. More specifically, the goal of this work is to improve bunker shielding calculations for neutrons by validating practical MC simulations with physical measurements performed in selected linac rooms of the McGill University Health Centre (MUHC). We hope that our work will eventually yield a useful in-house tool for neutron shielding calculations and bunker design.

In terms of the thesis structure, this first chapter will introduce fundamental notions of medical physics and basic concepts of radiation protection from a radiotherapy and radiation protection perspective. Although described briefly and superficially, the concepts of chapter 1 represent a mandatory minimum background required for the study of any health physics problem. Chapter

2 is the section entirely focused on explaining the physics of neutrons, their role in linac bunkers, and the associated detection techniques. Chapter 3 will introduce theoretical and practical aspects of the neutron shielding formalism found in reports 79 and 151 of the NCRP, as well as briefly review related MC simulation work on medical photoneutrons. Chapter 4 will detail our approach to neutron shielding simulations and present our results. Finally, the conclusion and future work directions will be developed in Chapter 5.

1.2 Ionizing radiation in medical physics

Radiological physics is the science aimed at understanding the interaction between matter and ionizing radiation, whereas radiation dosimetry is a related field focusing on the quantitative determination of the energy absorbed by matter during that interaction [8]. As the name indicates, the key property of ionizing radiation is its ability to ionize atoms. It must carry kinetic energies above 4-25 eV because this is the energy range needed to cause a valence electron to escape an atom.

1.2.1 Types of ionizing radiation

A brief and simple description of ionizing radiation types frequently encountered in medical physics follows.

γ-rays

Gamma radiation (photons also known as γ-rays) is emitted by excited nuclei in their transition to lower-lying nuclear levels. Since nuclear states have well-defined energies, the energies of gamma rays emitted in state-to-state transitions are also specific and monoenergetic. Gamma ray emission follows a β decay (emission of electron or positron) or an electron capture interaction (absorption of an orbital electron by the nucleus). The β decay, characterized by half-lives typically on the order of days, leads to the population of the excited state in the daughter (post-decay) nucleus. In contrast to β decay, excited daughter nuclear states have very short lifetimes on the order of picoseconds and femtoseconds.

X rays

X rays are high-energy photons that can be produced in monoenergetic or polyenergetic (spectrum) form. The former occurs when the configuration of orbital electrons is modified following an excitation process. This results in the emission of a characteristic x-ray photon whose energy is proportional to the energy levels involved in the electron distribution rearrangement. The latter, also known as bremsstrahlung, occurs when fast electrons interact in matter and lose part of their energy as electromagnetic radiation. The higher the electron energy or atomic number of the absorbing material, the higher is the conversion rate to bremsstrahlung.

Electrons and positrons

Electrons and positrons result from different interactions and are named accordingly. Beta minus (β^-) decay is the emission of a negative charge (or electron) from the nucleus, whereas beta plus (β^+) is the complementary effect involving the emission of a positive charge (or positron). β^+ and β^- decays result in a continuum of energies (spectra), whereas monoenergetic electrons are called Auger electrons or internal conversion electrons. The latter occurs when the energy of a γ-ray is transferred to an orbital electron, whereas the former is an analogue process produced instead with characteristic X-rays.

Heavy charged particles

As the name indicates, these are the nuclei of hydrogen atoms or its isotopes or atoms of a higher atomic number. They are usually generated by cyclotrons and heavy-particle linear accelerators, or result from the Alpha decay of some radioactive materials. Types include:

- Proton, deuteron, and triton, which are hydrogen atoms (a proton) with 0, 1, and 2 neutrons respectively.
- Alpha particle, which is the helium nucleus (^{4}He)
- Other nuclei of heavier atoms such as carbon or oxygen.
- Negative pions (negative π-mesons) produced by interaction of fast electrons or protons with fast nuclei.

Neutrons

Neutrons, the particles of interest in this thesis and the physics of which will be detailed in chapter 2, are neutral particles obtained from nuclear reactions since it is impossible to accelerate them electrostatically. They are of interest in medical physics and especially in health physics because of their significant potential to cause damage as well as their application in specific radiotherapy techniques such as boron-neutron capture therapy (BNCT).

1.2.2 The linear accelerator

Medical linear accelerators (linacs) use high-frequency electromagnetic waves to accelerate charged particles (electrons in medical physics), which are directly used to treat superficial tumours or are converted into bremsstrahlung x rays for treatment of a much wider variety of tumours throughout the body. Medical linacs are the most used tool for radiotherapy and an integral part of any radiation oncology unit, justifying a short description of their key components and functionality in any work pertaining to medical physics. Although linear accelerators are also used in other branches of physics, for practical reasons throughout this work the term linac will refer to medical linear accelerators.

Linacs are powered by microwaves of frequency ∼3000 MHz. A *power supply* provides direct current (DC) power to the *modulator*, which produces high-voltage pulses. These pulses are delivered to the *magnetron* or *klystron* and simultaneously to the *electron gun*. The magnetron or klystron inject pulsed microwaves into the *accelerator tube*, while the electron gun, in coordination with the magnetron or klystron, injects electrons, also into the accelerator tube.

The accelerator tube (or *waveguide*), which is made of copper (Cu) and evacuated to vacuum, is divided into various compartments that are specifically shaped to optimize the interaction of electrons with the electromagnetic waves and accelerate them from initial energies of ∼50 keV to the MeV range. The waveguide is a straight tube that accelerates the electrons in a straight line at the end of which bending magnets will direct the electron towards the exit window (made of beryllium).

The electrons emerge from the beryllium window as a pencil beam of about 3 mm in diameter and enter the section of the linac known as the treatment head and usually shielded by a lead-tungsten alloy. Depending on the type of intended therapy, they will be directed into a tungsten *target* for bremsstrahlung production or continue their way downstream for electron beam therapy. In the former case, the x-ray beam is collimated by the *primary collimator* and subsequently flattened by the *flattening filter*, whereas the electron pencil beam is transformed into a diverging beam after passing through a thin *scattering foil*. Finally, both types of beams are given the intended field dimensions by the secondary collimator. X rays are further shaped with the use of *multi-leaf collimators (MLC)*, whereas electron beams are given their final field size and shape with an *electron applicator* and a tertiary *cerrobend cutout*, respectively.

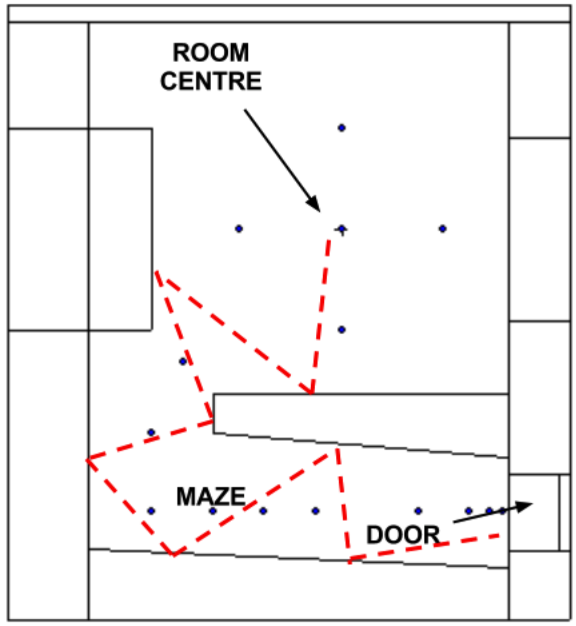

Figure 1–1: Top-down view of a typical high-energy radiotherapy room referred to as a linac bunker in this thesis. The red dotted line shows a typical trajectory of a neutron making its way from the linac head at the centre of the room to the room entrance

.

Finally, it is appropriate to present a simple diagram of a typical linac bunker in order for the reader to have a clear idea of the key elements that define the concrete room that includes the linac. Figure 1–1 shows a top-down view of a linac bunker with the centre of the room where most neutrons are generated, the maze which is an additional shielding to reduce the energy of neutrons, and the entrance to the room, with or without a door.

1.2.3 Biological effects of ionizing radiation

As a result of ionizing radiation, secondary electrons are produced in human body (mostly water). The average energies associated with these electrons are very low, in the range of $\sim$ 30-80 eV [9]. These electrons are further and quickly attenuated ($\lesssim 10^{-15}$ sec) through interactions to energies that are insufficient to cause subsequent electronic transitions ($\sim$ 7.4 eV for liquid water).

The initial consequence of radiation is therefore the creation of electrons and ionized/excited molecules such as H_2O^+ and H_2O^*, which in their turn will create free radicals (species with unpaired electrons). These free radicals produced by the excited molecules can attack DNA and cause a strand break (single or double), which is often considered to cause fatal damage to the cell since it prevents further divisions.

More generally, the biological effects of radiation depend on dose and the type of radiation. Some effects occur immediately and some may take years or even decades to become visible. By $\sim 10^{-3}$ sec, most radicals have already reacted and cell division might be affected within hours, whereas some biochemical processes are modified in less than a second.

Cell division can be impacted in a matter of hours whereas deterministic damage to the gastrointestinal track and central nervous system appears within a matter of days or less. The hematopoietic syndrome can occur in approximately a month. There are also other deterministic effects such as lung fibrosis that may develop weeks after exposure, cataracts (often caused by neutrons), as well as stochastic effects such as radiation induced carcinogenesis, which may be developed years or decades after irradiation [10].

It is important to mention that most dose-effect data in radiobiology stems from detailed dosimetric work that has been coupled with medical observations and epidemiological studies. There are four different sources of information pertaining to the effects of radiation on man

1. persons occupationally exposed to an excessive amount of radiation through an accident or negligence,
2. patients having been exposed to medical procedures,
3. populations exposed to the nuclear explosions at Hiroshima and Nagasaki

4. populations exposed to an excessive amount of radiation through accidents such as Chernobyl and Goiania

Occupational exposure studies also include data from several hundred radial dial painters who tipped brushes with their tongues when painting luminous watch dials [11]. Similar studies involving thousands of uranium miners have been conducted to study the incidence of lung cancer and other effects caused by breathing radon[12]. The studies on the impact of medical exposures have focused on thousands of patients exposed in various ways to some sort of diagnostic or therapeutic radiation. Among these, critically useful large studies of the effects of prenatal and paediatric exposures have been conducted [13]. Moreover, the effects of nuclear weapons tests and explosions during the second world war have been extensively studied over decades and have contributed to our understanding of the impact of a wide range of radiation doses and energies on humans [14][15]. Finally, major accidents which resulted in high radiation doses to populations (Chernobyl and Goiania), have also been extensively studied [16][17].

1.3 Quantities of importance in health physics

Medical physicists must know the physical quantities pertaining to a radioactive source (source strength, rate of decay, etc) and use these metrics to determine the radiation dose deposited in living tissue or in a phantom. Pushing this idea further, health physicists aim to determine radiation doses to different organs/tissues, from different types of radiation, and for ensembles of populations in order to quantify the potential damage caused by ionizing radiation and, more importantly, help shape regulations and security policy in the most effective manner. The quantities below are part of the fundamental toolbox used by health and medical physicists to quantify radiation dose and exposure.

1.3.1 Physical quantities

Before delving into a detailed description of physical quantities it is useful to quickly scan Table 1–1 [10], which summarizes the physical quantities of interest in radiation physics. For practical reasons, a distinction is made between quantities concerning radiation generally and quantities concerning radioactivity.

Fluence and Flux

Fluence Φ represents the number of particles (charged or uncharged) crossing a unit area :

$$\Phi = \frac{\mathrm{d}N}{\mathrm{d}A},$$

whereas particle flux, or fluence rate $\dot{\Phi}$ represents the number of particles crossing a unit area per unit time :

$$\dot{\Phi} = \frac{\mathrm{d}\Phi}{\mathrm{d}t} = \frac{\mathrm{d}}{\mathrm{d}t}\left(\frac{\mathrm{d}N}{\mathrm{d}A}\right).$$

Fluence has units of m^{-2} and flux has units of $\mathrm{m}^{-2} \cdot \mathrm{s}^{-1}$. Both concepts can be extended to include energy and as such for a monoenergetic beam, the energy fluence Ψ is the product of the particle fluence and the energy of the particles. The energy flux $\dot{\Psi}$ (also known as the intensity) is the energy fluence per unit time. The unit of energy fluence is $\mathrm{J} \cdot \mathrm{m}^{-2}$ and the unit of energy flux is $\mathrm{J} \cdot \mathrm{m}^{-2} \cdot \mathrm{s}^{-1}$. For polyenergetic beams, the expressions are modified to account for the entire spectrum of energies, and can be written in their differential forms :

$$\text{Particle fluence spectrum} = \Phi_E(E) = \frac{\mathrm{d}\Phi}{\mathrm{d}E}(E) \text{ and}$$

Table 1–1: Physical quantities used to quantify radiation (Courtesy of Dr. John Kildea [10]).

Quantity	Definition	Formula	Unit
	Radiation Beams		
Particle fluence	Number of particles crossing per unit area for a monoenergetic beam	$\Phi = \frac{\mathrm{d}N}{\mathrm{d}A}$	m^{-2}
Particle flux	Number of particles crossing per unit area per unit time for a monoenergetic beam	$\dot{\Phi} = \frac{d\Phi}{dt}$	$\mathrm{m}^{-2} \cdot \mathrm{s}^{-2}$
Energy fluence	Product of particle fluence and particle energy for a monoenergetic beam	$\Psi = \frac{dN}{dA}E = \Phi E$	$\mathrm{J} \cdot \mathrm{m}^{-2}$
Energy flux (ie intensity)	Product of particle flux and particle energy for a monoenergetic beam	$\dot{\Psi} = \frac{d\Psi}{dt}$	$\mathrm{J} \cdot \mathrm{m}^{-2} \cdot \mathrm{s}^{-1}$
Particle fluence spectrum	Particle fluence as a function of energy for a polyenergetic beam	$\Phi_E(E) = \frac{d\Phi}{dE}(E)$	
Energy fluence spectrum	Energy fluence as a function of energy for a polyenergetic beam	$\Psi_E(E) = \frac{d\Phi}{dE}(E)E$	
Exposure	Amount of charge of either sign collected in a given mass of air at standard temperature and pressure (for photons less than 3 MeV only)	$X = \frac{\Delta Q}{\Delta m_{\mathrm{air}}}$	$\mathrm{C} \cdot \mathrm{kg}_{\mathrm{air}}^{-1}$
Kerma	Mean energy transferred from indirectly to directly ionizing radiation per unit mass of absorbing material	$K = \frac{\mathrm{d}E_{tr}}{\mathrm{d}m}$	$\mathrm{J} \cdot \mathrm{kg}^{-1}$
Linear attenuation coefficient	The probability of a photon beam interacting in an absorber material as a function of depth into the material	$\mu = \frac{ln2}{\mathrm{HVL}}$	cm^{-1}
Mass attenuation coefficient	The linear attenuation coefficient divided by the density of the absorber material	$\mu_m = \frac{\mu}{\rho}$	$\mathrm{cm}^2 \cdot \mathrm{g}^{-1}$
Half Value Layer	The depth into an absorber material at which the intensity of a radiation beam drops to half of its initial value	$\mathrm{HVL} = \frac{ln2}{\mu}$	cm
Tenth Value Layer	The depth into an absorber material at which the intensity of a radiation beam drops to one tenth of its initial value	$\mathrm{TVL} = \frac{ln10}{\mu}$	cm
Linear Energy Transfer	The energy absorbed per unit length by an absorbing medium as ionizing radiation moves through it	$\mathrm{LET} = \frac{\mathrm{d}E}{\mathrm{dl}}$	$\mathrm{keV} \cdot \mu\mathrm{m}^{-1}$
Linear stopping power	The energy lost by a charged particle (or beam of charged particles) per unit length as it (they) traverses an absorber material	$\mathrm{S} = -\frac{dE}{dx}$	$\mathrm{MeV} \cdot \mathrm{cm}^{-1}$
Mass stopping power	The linear stopping power divided by the density of the absorbing medium	$\frac{S}{\rho}$	$\mathrm{MeV} \cdot \mathrm{cm}^2 \cdot \mathrm{g}^{-1}$
	Radioactive Sources		
Activity	Number of radioactive transformations per second	$\mathcal{A} = \frac{\mathrm{d}N}{\mathrm{d}t}$	Becquerel (1 Bq = 1 s^{-1})
		$\mathcal{A}(t) = \mathcal{A}(0)e^{-\lambda t}$	Curie (1 Ci = 3.7×10^{10} Bq) Rutherford (1 Rd = 1×10^6 Bq)
Radioactive decay constant	The probability of a radioactive decay transformation per unit time	$\lambda = \frac{ln2}{t_{1/2}}$	s^{-1}
Half life	Time necessary for half the original number of nuclei in a radioactive sample to decay	$t_{1/2} = \frac{ln2}{\lambda}$	s
Specific activity	The activity of a radioactive sample divided by its mass	$a = \frac{\mathcal{A}}{m}$	$\mathrm{Ci} \cdot \mathrm{g}^{-1}$ (SI unit: $\mathrm{Bq} \cdot \mathrm{kg}^{-1}$)
Exposure rate constant	The exposure rate, in R/h, at a distance of 1 m from a sample of a radionuclide having an activity of 1 Ci	Γ	$\mathrm{R} \cdot \mathrm{m}^2 \cdot \mathrm{Ci}^{-1} \cdot \mathrm{h}^{-1}$
Exposure rate due to a radionuclide	The exposure rate constant for the radionuclide times its activity, divided by the distance from the source squared	$\dot{X} = \frac{X}{t} = \Gamma\frac{\mathcal{A}}{d^2}$	$\mathrm{R} \cdot \mathrm{h}^{-1}$

$$\text{Energy fluence spectrum} = \Psi_E(E) = \frac{\mathrm{d}\Phi}{\mathrm{d}E}(E)E\,.$$

Exposure

Exposure (X) allows for quantification of the fluence of an x-ray or gamma-ray field. It is defined as the amount of charge *of either sign* collected in a given mass of air at standard temperature and pressure (STP). It is defined only for photons with energy less than 3 MeV, whereby :

$$X = \frac{\Delta Q}{\Delta m}\,.$$

The unit of exposure is Coulombs per kilogram of air. The old unit of exposure was the Röntgen (R), and 1 R is equivalent to $2.58 \times 10^{-4}\ \mathrm{C} \cdot \mathrm{kg}_{\mathrm{air}}^{-1}$.

Kerma

Kerma stands for Kinetic Energy Released per unit Mass. It is an indicator of the mean energy transferred per unit mass of absorbing material, from indirectly ionizing radiation to directly ionizing radiation. Kerma is independent of whether or not the directly ionizing radiation produced is absorbed in the absorbing material. The relevant interaction is the initial transfer of energy from the incident indirectly ionizing particle to the directly ionizing one :

$$K = \frac{\mathrm{d}E_{tr}}{\mathrm{d}m}\,.$$

The unit of Kerma is the gray, corresponding to $1\ \mathrm{J} \cdot \mathrm{kg}^{-1}$.

Linear Attenuation Coefficient

The linear attenuation coefficient, μ, is the probability of a photon beam interacting in an absorber material as a function of depth into the material. It has units of cm^{-1}. The mass attenuation coefficient μ_m is equal to the linear attenuation coefficient divided by the density of absorber material. Since the mass attenuation coefficient is independent of the density of the absorber material it is a useful quantity when comparing the Z dependencies of photon attenuation in various absorber materials. Its unit is m^2/kg or more commonly cm^2/g.

HVL and TVL

Half value layer (HVL) and tenth value layer (TVL) are the depths in an absorber material at which the intensity of a radiation beam drops, respectively, to one half and to one tenth of its initial intensity. HVL and TVL are essential metrics in health physics and shielding design and are also used to characterize the penetrability/strength of a beam. The simple relations between the HVL, TVL and linear attenuation coefficients are :

$$\mathrm{HVL} = \frac{\ln(2)}{\mu}\,, \text{ and}$$

$$\mathrm{TVL} = \frac{\ln(10)}{\mu}\,.$$

Linear Energy Transfer

Linear energy transfer (LET) is defined as the rate of *energy absorption* by an absorbing medium as ionizing radiation moves through the medium. It has units of keV/μm,

$$\mathrm{LET} = \frac{\mathrm{d}E}{\mathrm{dl}}\,.$$

Stopping Power

The stopping power S of a charged particle is the energy lost by the particle (or beam) per unit length as it traverses an absorbing material :

$$\mathrm{S} = -\frac{\mathrm{d}E}{\mathrm{dx}}\,.$$

Stopping power may be greater than LET as the secondary electrons produced in the medium as the charged particle moves through it may have enough energy to leave the region of interest and deposit their energy elsewhere. Thus, the energy absorbed by the medium (LET) in the region of interest will be less than the energy lost by the charged particle (stopping power). Stopping power is expressed in units of MeV/cm. Just like the linear attenuation coefficient, the mass stopping power $\frac{S}{\rho}$ is equal to the (linear) stopping power divided by the density of the absorbing medium. Its units are $\mathrm{MeV} \cdot \mathrm{cm}^2 \cdot \mathrm{g}^{-1}$.

Activity

Activity $\mathcal{A}$ of a radionuclide is defined as the number of radioactive transformations (decays) it undergoes per second :

$$\mathcal{A} = -\frac{\mathrm{d}N}{\mathrm{dt}}$$

The SI unit for activity is the becquerel (Bq), which corresponds to one decay per second. In radiation physics, the curie (Ci) was often used as an alternative unit of radioactivity. It is defined as

$$1 \ \ \mathrm{Ci} = 3.7 \times 10^{10} \ \mathrm{Bq} \, .$$

The activity of a radioactive substance decreases as a function of time and from this follows that the number of nuclei (i.e. the activity) is proportional to the number of nuclei present. The law of radioactive decay is thus given by the following equation :

$$\mathcal{A}(t) = \mathcal{A}(0) e^{-\lambda t} \tag{1.1}$$

This law states that the activity $\mathcal{A}(t)$ of a radioactive sample at any time t is equal to the initial activity of the sample $\mathcal{A}(0)$ at time $t = 0$ multiplied by an exponential decay factor $e^{-\lambda t}$, where λ is the decay constant of the particular radionuclide. Since the exponential decay factor is unitless, λ has units of s^{-1}. It gives the probability of radioactive decay per unit time. It must be noted that a correlated quantity, the half-life of a radionuclide, is defined as the time necessary for half of the original nuclei in a sample to decay. The relationship between half-life and decay constant is simply :

$$\mathrm{t}_{\frac{1}{2}} = \frac{\ln(2)}{\lambda}\,.$$

Finally, a useful and related quantity is the specific activity a of a radioactive sample, which is defined as its activity per unit mass. The units of specific activity are Ci/g.

1.3.2 Dosimetric quantities

Dosimetric quantities are used by medical physicists to quantify dose to matter by accounting for various aspects of dosimetry, physics, and radiobiology. Table 1–2 [10] outlines the dosimetric quantities and units that are most frequently encountered.

Absorbed Dose

One of the most extensively used quantities, absorbed dose D is the quantity of radiation absorbed in irradiated material and is simply a measure of the energy of ionizing radiation absorbed per unit mass of absorbing material. Its unit is the gray (Gy) and it may be characterized as :

$$D = \frac{\Delta E_{abs}}{\Delta m}\,.$$

Equivalent dose

Equivalent dose is the quantity that accounts for the differences of lethality between types of radiation. The ICRP defines *equivalent dose* H_T for a particular tissue or organ T as the sum of the absorbed doses to the organ or

Table 1–2: Dosimetric quantities and units used in radiation protection (Courtesy of Dr. John Kildea [10]).

Quantity	Definition	Formula	Unit
		Purely Physical	
Absorbed dose	Energy absorbed per unit mass	$D = \frac{\Delta E_{abs}}{\Delta m}$	Gray (1 Gy = 1 $\frac{J}{kg}$)
		Concerning Individuals	
Equivalent dose	Sum of absorbed doses D to a single exposed tissue or organ T for one or more radiations R, with each D multiplied by the appropriate radiation weighting factor	$H_T = \sum_R w_R D_{T,R}$ (for radiations R)	Sievert (1 Sv = 1 $\frac{J}{kg}$)
Effective dose	Sum of equivalent doses H_T to one or more exposed tissues and organs T, with each H_T multiplied by the appropriate tissue weighting factor	$E = \sum_T w_T H_T$ (for tissues T)	Sievert
Personal equivalent dose	The equivalent dose in soft tissue below a specified point on the body at an appropriate depth d (0.07 mm or 10.0 mm below skin, 3.0 mm into eye)	$H_p(d)$	Sievert
		Concerning Populations	
Collective equivalent dose	Product of average equivalent dose to organ T and the number of individuals exposed	$S_T = \sum_i \bar{H}_{T,i} N_i$ (for individuals i)	Person-sievert
Collective effective dose	Product of average effective dose and the number of individuals exposed	$S = \sum_i \bar{E}_i N_i$ (for individuals i)	Person-sievert

tissue from radiations of different types R, each multiplied by an appropriate radiation weighting factor w_{R} :

$$H_T = \sum_R w_R D_{T,R} \, .$$

The unit of equivalent dose is the sievert (Sv). Radiation weighting factors are based upon the RBE (Relative Biological Effectiveness) of the various radiations, in comparison with 200 kV X rays, as described below.

Effective Dose

Just as different types of radiation have different weighting factors, different tissues and organs of the bodies have different sensitivities to radiation. The effective dose is the sum of the equivalent doses to exposed tissues and organs multiplied by the appropriate tissue weighting factors w_T. The sum of all tissue weighting factors for the whole body is equal to one, so that

$$E = \sum_T w_T H_T \text{ , and}$$

$$\sum_T w_T = 1 \, .$$

Personal Equivalent Dose

Finally, personal equivalent dose $H_p(d)$ is defined as the equivalent dose in soft tissue below a specified point on the body at an appropriate depth d. Its unit is also the sievert (Sv).

1.3.3 Biological quantities

In health physics, several quantities are defined that take into account both the physical and biological aspects of radiation exposure. A sample of those is presented below.

Biological Half-Life

The biological half-life of a substance is the time it takes for half of the substance to leave a compartment (organ or body section) of a living organism. The biological decay constant is analogous to the radioactive decay constant and it gives the probability of a unit substance leaving a biological compartment in unit time as :

$$t_{\frac{1}{2}b} = \frac{\ln 2}{\lambda_b} \, .$$

The effective half life of a radionuclide accounts for both the biological and radioactive half lives of the radionuclide. The relation between physical and biological half-lives is an inverse addition, i.e. inverse physical and biological half-lives add to give the inverse effective half-life described as :

$$\frac{1}{t_{\frac{1}{2}e}} = \frac{1}{t_{\frac{1}{2}p}} + \frac{1}{t_{\frac{1}{2}b}} \, .$$

Relative Biological Effectiveness

The relative biological effectiveness (RBE) is a quantity that allows us to compare the effectiveness of different radiations at inflicting biological damage. It uses the amount of damage due to 200 keV x rays, as a normalization factor. RBE for a particular radiation is defined as the ratio of the dose from 200 keV x rays needed to produce a given biological effect to the dose of the particular radiation needed to produce the same biological effect :

$$RBE = \frac{\text{Dose from 200 keV to a tissue}}{\text{Dose from a test radiation for same biological effect}} .$$

1.4 Concepts of radiation protection

Ionizing beams can be classified with respect to the nature of the radiating particle but also in terms of the density of ionization they generate when traversing a medium. The density of ionization depends on the type and energy of the particle and is quantified by a parameter known as the Linear Energy Transfer (LET). In general, heavier and lower-energy particles have higher LET values than lighter or high-energy particles and the value of 10 keV/μm separates low LET (sparsely ionizing) from high LET (densely ionizing) radiation. Another defining feature of radiation beams dependent on particle type and energy is their penetrability into an absorber material. Naturally, the higher a particle's energy (and lower its LET), the more penetrating it will be. Telling examples are the low penetrability of alpha particles (high LET), high penetrability of gamma rays (lower LET), and the efficient slowing of neutrons when interacting with hydrogenous materials (figure 1–2). In its simplest form and from a physics perspective, radiation protection is based on three key principles: distance, time, and shielding:

1. **Distance:** Exposure to radiation decreases as one moves away from the radioactive source. The inverse square law quantifies this concept by

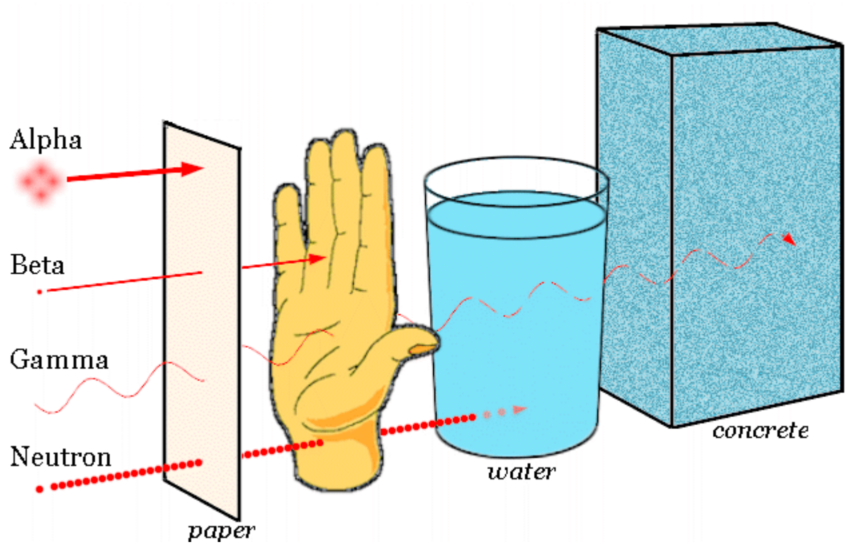

Figure 1–2: Illustration of the penetrability of various radiation beams. Reproduced from [18].

stating that exposure to radiation is inversely proportional to the square of the distance from the source.

2. **Time:** Because exposure increases linearly with time, the longer one is exposed the more damage it will sustain, hence the necessity to minimize average time of exposure to radiation.
3. **Shielding:** The quantity and composition of obstacles between a radiation source and the exposed subject determine its shielding efficiency. The attenuating properties of a material for a given type and energy of radiation form the basis of shielding science.

These three tenets apply to all forms of radiation including scatter radiation. Scattering occurs when the radiation is not absorbed during interaction and is instead redirected in various directions. The health hazards associated with this type of radiation are considerable and constitute - as will be seen subsequently - the main challenge for radiotherapy room design. The radiation scattered off the walls of the room, the patient, and the couch, becomes a significant contributor to dose at a point outside the room and must be shielded for accordingly.

Another important consideration in radiation protection is the bremsstrahlung radiation produced when high energy electrons slow down in high atomic number materials. This implies that beta particle emitting sources should not be only shielded with high Z materials since the Bremsstrahlung thus produced will be much more penetrating than the primary electron beam. Double shielding is therefore necessary, i.e. a first layer of electron attenuating material followed by the high Z material to stop secondary x rays.

A key concept in radiation protection is the ALARA (As Low As Reasonably Achievable) principle. Its underlying principle is that exposure to radiation must be constantly minimized, even if limits are already respected. In other words, the health physicist should not only aim to not exceed *acceptable* thresholds, but to reduce exposure to the lowest value attainable taking social and economic factors into account.

Radiation protection is structured around the idea that different types of professionals from radiation related fields will be associated with different exposure criteria/thresholds. These guidelines, referred to as *occupational*, differ from those applicable to the general public. The latter usually represent one-tenth of the occupational values. Why would higher exposure values be tolerated for a nuclear energy worker (NEW, defined by the CNSC [19])? The philosophy justifying this approach is based on the fact that NEWs have the tools and knowledge required to minimize their exposure, because they are exposed as a result of a remunerated activity, and because they can change their job if they want to [9]. On the other hand, members of the public don't have a choice and are exposed to radiation unwillingly.

1.5 Regulatory bodies and key dose limits

Because of its potentially high impact on the health of society and the major risks it presents, the use of radiation for medical and civil purposes is highly regulated and structured in a way to comply with various dose limits that apply to nuclear energy workers (NEW) as well as to the general public. In Canada, the legal framework is established by specific laws enacted by parliament. The Canadian Nuclear Safety Commission (CNSC) has the mandate to assist the government in matters related to radiation in regulation, mining, and research. Its mandate - given by the Nuclear Safety and Control Act of 1997 (NSCA) - stipulates that the CNSC regulates the use of nuclear energy and materials to protect the health, safety and security of Canadians and the environment [20]. The import, export, and sale of radiation-emitting devices are regulated by Health Canada under the "Radiation Emitting Devices Act" (RED Act) of 1985. The transport of radioactive material is regulated by Transport Canada according to the "Transport of Dangerous Goods Act" (TDG Act) of 1992.

Other organizations that are references in radiation protection are the International Commission on Radiological Protection (ICRP) and the International Commission on Radiation Units and Measurements (ICRU), both of which were formed before the middle of the 20th century. In the US, the reference organization is the National Council on Radiation Protection and Measurements (NCRP), a non-governmental public service organization with a congressional charter to provide recommendations regarding radiation protection. It is also much more than a national organization since its reports are considered to be highly valued scientific references and as such, are consulted internationally.

In Canada, all radioactive materials are regulated by the CNSC, while diagnostic x-ray production devices are overseen by provincial organizations such

Organ/ Tissue	Person	Period	Dose (mSv)
	Effective Dose Limits		
Whole body	Nuclear energy worker, including a pregnant nuclear energy worker	(a) One-year dosimetry period*	50
		(b) Five-year dosimetry period	100
	Pregnant nuclear energy worker	Balance of the pregnancy	4
	A person who is not a nuclear energy worker	One calendar year**	1
	Equivalent Dose Limits		
Lens of an eye	(a) Nuclear energy worker	One-year dosimetry period	150
	(b) Any other person	One calendar year	15
Skin	(a) Nuclear energy worker	One-year dosimetry period	500
	(b) Any other person	One calendar year	50
Hands and feet	(a) Nuclear energy worker	One-year dosimetry period	500
	(b) Any other person	One calendar year	50

Table 1–3: CNSC effective and equivalent dose limits (Courtesy of Dr. John Kildea [10]).

as the Service de Radioprotection of the Ministère de l'Environnement. Generally, there is no redundancy and overlap of responsibility areas.

It is relevant in any work pertaining to health physics to briefly summarize the radiation protection dose limits defined by relevant instances (in Canada by the CNSC) and in this regard, a short list is included in the form of a table 1–3 [10] [20]. An exhaustive list of regulations with detailed explanations is available on the CNSC website (www.cnsc-ccsn.gc.ca).

As demonstrated by the significant amount of legal and regulatory information presented in this first chapter, physical concepts and legal aspects of radiation regulation go hand in hand in health physics.

Chapter 2
Neutrons and Associated Detectors

In a manner similar to photons, neutrons do not carry any charge and therefore do not interact in matter by means of the Coulomb force. This allows them to travel through many centimetres of matter while being invisible to detection techniques based on electromagnetic interactions [21]. Consequently, neutron detection remains a technical challenge in physics and particularly in medical physics where neutrons are sometimes a by-product of X-ray generation and are considered to have a secondary effect in the radiotherapy process. This chapter will introduce the fundamentals of neutron physics, describe their role and impact in radiotherapy, and explain the methods and tools used for the detection and quantification of neutron dose.

2.1 Neutrons and their interactions with matter

As indirectly ionizing radiation, neutrons penetrate the absorber in a quasi-exponential manner and deposit energy in two steps [22]:

1. transfer of energy to heavy charged particles,
2. deposition of energy through Coulomb interactions of these charged particles with the atoms of the absorber.

2.1.1 Types of neutrons

Neutrons are divided into various categories on the basis of their energy, *i.e.* specific energy windows are associated to a type of neutron which is labeled as hot, epithermal, cold, fast, or slow. The last two categories - fast and slow- are of interest to this work. The former are used in external beam neutron therapy, whereas the latter have found application in boron-neutron capture therapy (BNCT) [22]. The dividing energy value between these two types of neutrons is ∼0.5 eV (or the *cadmium cut-off* energy) [21].

The neutron energy is also known as the neutron detection temperature and gives its average kinetic energy E_K in electron volts (eV). The term temperature refers to the hot, thermal, and cold neutrons being moderated in mediums with different temperatures. The energy distribution of neutrons being Maxwellian *i.e.* dependent on thermal motion, neutron kinetic energy is proportional to temperature. Also, the De Brogle relation holds for neutrons and relates speed, energy, and wavelength.

Slow neutrons

Slow neutrons, also known as *thermal neutrons*, have average kinetic energies of $E_K \approx 0.025$ eV and are always below 0.5 eV. Slow neutron interactions are of interest to medical physicists because they can generate secondary radiation with sufficient energy to be detected and/ or cause biological damage. When a slow neutron is captured by a nucleus (*i.e.* when it reaches a state of thermal equilibrium with the absorber medium) it is often followed by the emission of a photon that is easier to detect than the original incident neutron [21], but which can also cause DNA breaks and harm individuals.

Thermal neutrons may undergo a reaction known as radiative capture [or (n, γ) reaction], which is crucial in neutron shielding considerations since most neutrons reaching the door of a bunker are slow neutrons (or *thermalized neutrons*) and will be captured by surrounding shielding materials. The emitted γ radiation must be accounted for in shielding considerations, hence the importance of a clear understanding of radiative capture.

The two possible thermal neutron reactions with tissue are neutron capture by nitrogen-14 ($^{14}_{7}$N) or by hydrogen-1 ($^{1}_{1}$H). According to the ICRU

[23] and the ICRP [24], these two isotopes are present in human tissue in the following proportions: ∼10% in mass for hydrogen-1 and ∼3% in mass for nitrogen-14 [22].

Fast neutrons

Fast neutrons have kinetic energies $E_K > 0.1$ MeV and are widespread in high-energy (> 10 MeV) radiotherapy rooms. As the energy of the neutron increases, the probability of scattering becomes greater and inversely, the probability of neutron-induced secondary radiations useful in detectors drops off rapidly. Often, recoil nuclei (i.e. protons), having picked-up detectable kinetic energy from the neutron, become the secondary radiation that offers indirect information on the nature of the incident neutrons. The most common interactions between neutrons and the atomic nucleus are $(\mathrm{n}, \mathrm{p}), (\mathrm{n}, \alpha),$ and (n, γ) reactions.

2.1.2 Neutron interaction cross-sections

The effective (or characteristic) area that controls the probability of interaction for a given material and neutron energy is a constant known as the *cross-section* σ. This probability is expressed per nucleus for each type of interaction and is measured with units of *barn* (1 barn = 10^{-28} m^2) [21]. Each material/element will have an elastic scattering cross-section and a radiative capture cross-section, which will be a function of the neutron energy. For example, *boron* (Z=5) has a high capture cross-section for thermal neutrons and as will be explained later, this feature makes boron a material of choice for neutron shielding applications.

Multiplying the cross-section by the number of nuclei N per unit volume yields the macroscopic cross section with units of inverse path length. The combination of all the inverse path lengths for all interactions gives the total probability of interaction. It is an analogous quantity to the linear absorption coefficient defined previously and implies that the number of neutrons falls off exponentially with the thickness of the absorber [21]. From this, the neutron mean free path λ can also be deduced by taking the inverse of the macroscopic cross-section. In solids, λ varies from a few centimetres for slow neutrons to tens of centimetres for fast neutrons. It must be noted that exponential attenuation is an idealized description because in reality most neutron shielding situations involve broad beams that include the scattered neutrons.

2.1.3 Elastic scattering

Elastic scattering refers to the collision of a neutron with a nucleus, while the energy and momentum of the system before and after the collision remain the same (*i.e.* are conserved). From basic collisional mechanics [22], the average kinetic energy transferred to the recoil nucleus by the neutron is

$$\overline{\Delta E}_K = \frac{1}{2}(\Delta E_K)_{max} = \frac{1}{2}(E_K)_i \frac{4m_n M}{(m_n + M^2)} = 2(E_K)_i \frac{m_n M}{(m_n + M)^2} \tag{2.1}$$

where:

$(\Delta E_K)_{max} =$ the maximum kinetic energy transfer,

$m_n =$ is the mass of the incident neutron,

$\overline{\Delta E}_K =$ is the average kinetic energy transfer,

$M =$ is the mass of the nucleus,

$(E_K)_i =$ is the initial energy of the neutron.

Equation 2.1 implies that when colliding with a hydrogen nucleus of mass $M = m_p \approx m_n$, on average half of the kinetic energy of the neutron is transferred to the proton. This average energy transferred is much less when $M \gg m_n$ and decreases to just $\sim 2\%$ for a neutron colliding with a lead nucleus. The obvious implication for shielding is that neutrons lose more kinetic energy when interacting with hydrogenous materials (or at least low atomic number materials). Elastic scattering is key for neutron shielding in radiotherapy rooms where concrete walls with high hydrogen content serve as an excellent fast neutron attenuating medium.

2.1.4 Inelastic scattering

In inelastic scattering, a neutron n is first captured by the nucleus and then re-emitted as neutron n' with a lower energy and in a different direction with respect to the incident neutron. The nucleus, having transitioned to an excited state, will return to a less energetic state by emitting high energy γ rays [22]. The process is the following

$$n + {}^{A}_{Z}X \rightarrow {}^{A+1}_{Z}X^{*} \rightarrow {}^{A}_{Z}X^{*} + n' \Rightarrow {}^{A}_{Z}X^{*} \rightarrow {}^{A}_{Z}X + \gamma \tag{2.2}$$

where the * superscript indicates the temporarily excited nature of a nucleus and the other terms are defined as follows:

${}^{\mathrm{A}}_{\mathrm{Z}}\mathrm{X}$ = the stable target nucleus,

${}^{\mathrm{A+1}}_{\mathrm{Z}}\mathrm{X}^{*}$ = the unstable compound nucleus,

${}^{\mathrm{A}}_{\mathrm{Z}}\mathrm{X}^{*}$ = the excited target nucleus.

2.1.5 Neutron capture

As mentioned previously neutron capture occurs when thermal neutrons are absorbed by a nucleus, which, in order to reach a minimal energy configuration, will immediately emit a γ ray or a proton. Reactions of importance in tissue include ${}^{1}\mathrm{H}(\mathrm{n},\gamma){}^{2}\mathrm{H}$ and ${}^{14}\mathrm{N}(\mathrm{n},\mathrm{p}){}^{14}\mathrm{C}$, whereas a reaction relevant for thermal neutron shielding considerations in nuclear fission is ${}^{113}\mathrm{Cd}(\mathrm{n},\gamma){}^{114}\mathrm{Cd}$. Indeed, a 1 mm thick cadmium filter can absorb all incident thermal neutrons, whereas higher energy neutrons will almost all be transmitted. The reason for this is that cadmium's cross-section for neutron capture exhibits a peak at 0.178 eV. Interestingly enough, the value of this peak for natural cadmium is 7800 barns, whereas for ^{113}Cd the peak is much larger with a value of $\sim 64 \times 10^3$ barns [22].

Capture reactions are exploited in medical physics where neutron bombardment of stable nuclei yields γ emitting radioactive nuclei, a process known as neutron activation. Practical examples include radiotherapy cobalt-60 sources, brachytherapy iridium-192 sources, and molybdenum-99 sources which are used in nuclear medicine [22].

An analogous reaction with additional reaction products is the boron-neutron capture reaction. The particularity of this reaction is the very high cross-section ($\sigma = 3840$ barn) of boron-10 for thermal neutrons. The reaction, which has also found applications in external neutron beam therapy and is known as boron neutron capture therapy (BNCT), has the following form where the value of Q is 2.79 MeV if the Li is left in the ground state and 2.31 MeV if it is left in the excited state.

$$ {}^{10}_{5}B + n \rightarrow {}^{7}_{3}Li + \alpha + \ Q \tag{2.3} $$

Finally, highly relevant to this work is the possibility to exploit the boron high cross-section (used in the form of borated polyethylene) for thermal neutron in medical linac bunker shielding applications.

2.2 Neutron kerma

Neutron fields are usually described in terms of fluence $\varphi(E_K)$. The neutron kerma K accounting for all possible interactions is given by :

$$ K = \varphi \frac{\mu_{tr}}{\rho} E_K \, , \tag{2.4} $$

where E_K is the kinetic energy of the monoenergetic neutron beam and $(\frac{\mu_{tr}}{\rho})$ is the mass energy transfer coefficient given in usual units of $\mathrm{cm^2.\,g^{-1}}$. The term $(\frac{\mu_{tr}}{\rho})E_K$ is also called the *neutron kerma factor* F_n with units of $\mathrm{J.\,cm^2.\,g^{-1}}$

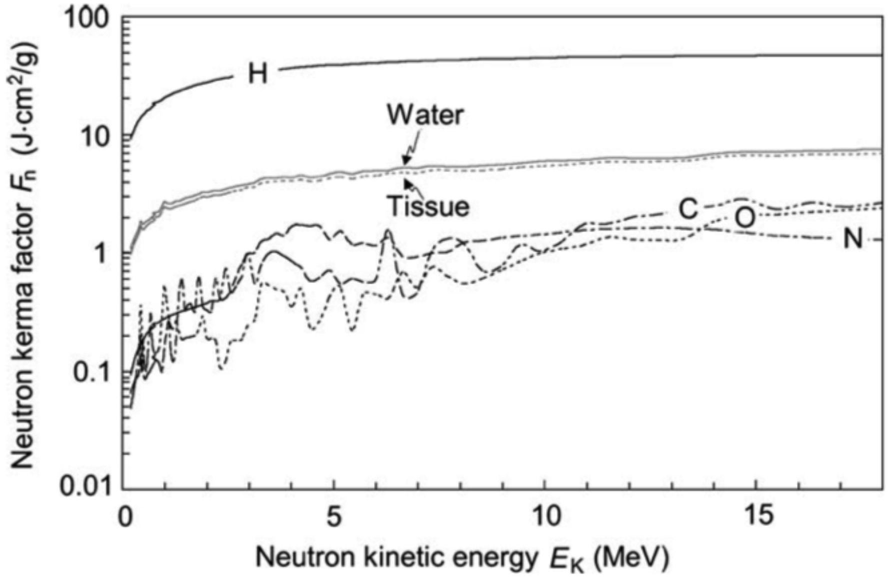

Figure 2–1: Kerma factor vs. kinetic energy of neutrons for different materials. Reproduced from [22] and based on NIST data.

[22]. For monoenergetic neutrons, equation 2.4 becomes :

$$K = \varphi(F_n)_{E_K,Z}\,, \tag{2.5}$$

where $(F_n)_{E_K,Z}$ is the neutron kerma factor $\mathrm{F_n}$, E_K is the kinetic energy of neutrons, and Z is the atomic number of the absorber. Figure 2–1, obtained with data from the NIST (National Institute of Standards and Technology), shows the relation between the neutron kerma factor $\mathrm{F_n}$ and the kinetic energy of neutrons for a number of materials found in medical physics [22]. When the neutron beam is characterized by an energy spectrum, the total kerma can be written :

$$K = \int_0^{(E_K)_{max}} \varphi'(E_K)\,(F_n)_{E_K,Z}\,\mathrm{d}E_K\,, \tag{2.6}$$

where $(E_K)_{max}$ is the maximum neutron kinetic energy and $\varphi'(E_K)$ is the differential fluence distribution. In the case of neutron kerma, the energy is transferred to various particle types such as ions, protons, and alpha particles. In linacs, these charged particles are quickly stopped in matter and the

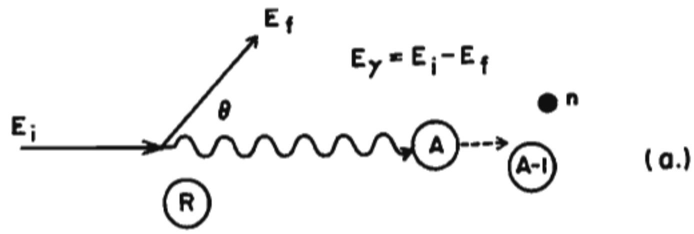

Figure 2–2: Schematic representation of the neutron production process. Reproduced from [26].

approximation equating local neutron dose to local neutron kerma is therefore valid [25]. As will be seen in chapter 4, the MCNP simulation code can calculate neutron kerma and therefore this approximation lies at the basis of neutron Monte-Carlo simulations.

2.3 Neutrons in medical physics

In EBRT and in the context of shielding, one should speak of photo-neutrons since all neutrons in a high energy linac bunker are produced as a result of the photo-nuclear reaction. Briefly and as shown in figure 2–2, an electron with energy $\mathrm{E_i}$ scatters through an angle θ in the Coulomb field of the target nucleus R to produce a photon of energy $\mathrm{E_\gamma = E_i - E_f}$. This is how the Bremsstrahlung photons are generated in the linac target. This photon then induces the photonuclear reaction in the nuclei A of the target or the materials surrounding/shielding the target (W or/and Pb), via the reaction $\gamma + \mathrm{A} \rightarrow (\mathrm{A} - 1) + \mathrm{n}$, which can also be expressed by the more standardized form of equation 2.7.

$$^{A}X(\gamma, n)^{A-1}X \tag{2.7}$$

Linacs operating above 10 MeV produce radiation beams that are significantly contaminated with photoneutrons, hence the importance of considering the neutron component of the radiation field. In theory, between 6 and 16 MeV are required to remove neutrons from stable atoms heavier than carbon [26], but

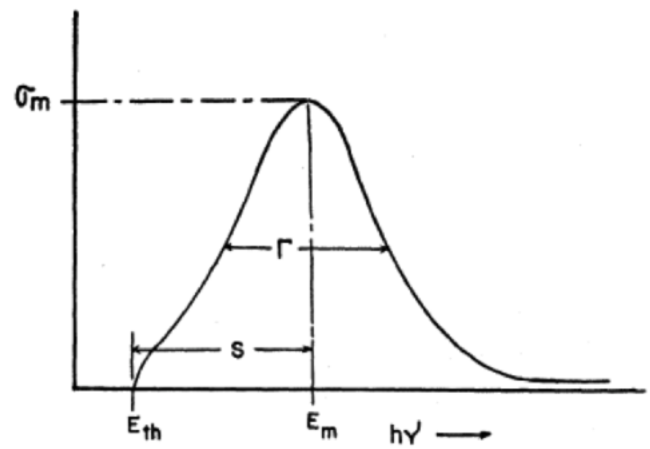

Figure 2–3: General form of the photoneutron production cross-section (arbitrary units) vs. incident photon kinetic energy (arbitrary units). Reproduced from [27].

in the context of radiotherapy the practical threshold to create a measurable amount of photoneutrons is often considered to be about 10 MeV.

Figure 2–3 shows the general form of the cross-section - measured in millibarn (mb) - for the photoneutron reaction in a given material as a function of the incident photon kinetic energy, measured in MeV. The cross-section curve has a threshold energy (E_{th}) below which the reaction does not occur and a peak that is $\sim$ 3-7 MeV above E_{th}. This peak located at E_m is called the giant resonance peak because its shape is characteristic of resonance reactions and it is attributed to electric dipole absorption of the incident photon [26].

The typical linac has massive photon shielding around the target which serves to produce a collimated beam of x-rays during the operation of the accelerator. These shielding materials are usually heavy metals such as tungsten or lead, and small amounts of iron and copper can also be found in the bending magnets. Once the photoneutron is produced, the most significant mechanism of neutron energy loss in these heavy elements is inelastic scattering. Although present, elastic scattering is not accompanied by significant neutron energy loss because of the large mass difference between the neutron and the nuclei of the heavy elements (as demonstrated by equation 2.1). Because inelastic scattering will only happen if the neutron energy is above the lowest excited state of the absorber (in this case the shielding material, see equation 2.2), the lower corresponding values for tungsten make it a relatively more effective neutron energy attenuator than lead. Indeed, below 0.57 MeV, lead is virtually transparent to neutrons whereas inelastic scattering can occur at much lower energies in tungsten [26]. The other reason favouring tungsten over lead is the higher atomic density of the latter (1.9 times more atoms per cm^3).

The major parts of the linac from which photoneutrons are generated are the bending magnet, the target, the flattening filter, and the collimator [6], [26]. Figure 2–4 is a simplified schematic drawing of a typical medical linac head. Since the shielding is designed primarily for photons, which are emitted predominantly in the forward direction, the shielding tends to be much thicker and heavier in this direction. This distribution of shielding materials is unfortunately not appropriate for photoneutrons, which are emitted isotropically. Nevertheless, the average photoneutron is scattered so many times in the linac head that the head shielding can be approximated as a hollow sphere, with a wall thickness of up to 10 cm for tungsten and 15 cm for lead [26].

2.3.1 Photoneutron spectra

The photoneutron spectrum at different locations in a medical linac bunker is a key metric in design considerations because it is only through a complete understanding of the energy distribution of the photoneutrons that one can develop an effective bunker shielding strategy. From the moment they are generated in the head of the linac until they reach the door of the bunker, photoneutrons will lose much of their energy through the various physical interactions described previously. Consequently, the most useful tool for understanding and eventually controlling this energy degradation process is the

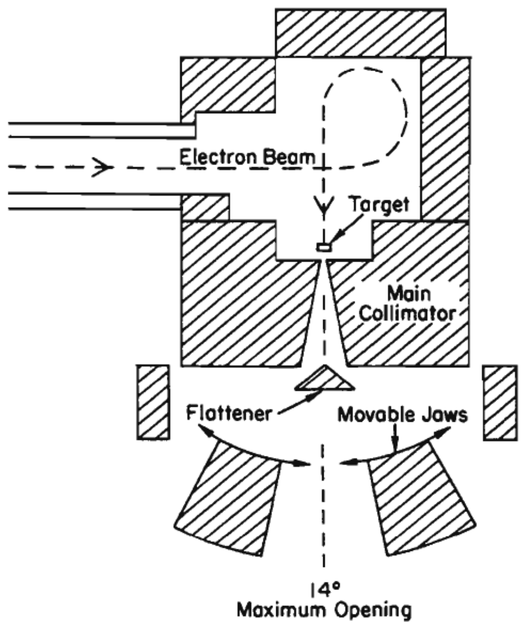

Figure 2–4: Simplified diagram of a medical linear accelerator head. Reproduced from [26].

energy spectrum of the photoneutrons. Moreover, in order to obtain equivalent dose, many of the neutron detectors that measure fluence require the use of fluence to equivalent dose conversion coefficients. These coefficients, found in report 74 of the ICRP [28] and shown in figure 2–8, depend strongly on the neutron energy and hence the neutron spectrum must be known in order to determine dosimetric information.

Two groups of neutrons are produced in photoneutron reactions. One group has a Maxwellian energy distribution and is composed of evaporation neutrons, meaning that photons interact with the entire target nucleus and that generated photoneutrons have an isotropic angular distribution. This group constitutes the majority of the photoneutrons. The second group is composed of direct neutrons that, as their name implies, are produced when the photon interacts directly with a neutron in the target nucleus. The result is that direct photoneutrons are more energetic than evaporation neutrons and have an anisotropic angular distribution. This category represents up to ∼15% of all photoneutrons [6]. The analytical equation that describes the photoneutron spectrum with the contribution of the two types of photoneutrons is given by equation 2.8 and was first reported in 1991 [29].

$$\frac{\mathrm{d}N}{\mathrm{d}E_n} = \frac{0.8929\, E_n}{(T)^2} \exp\left(\frac{-E_n}{T}\right) + \frac{0.1071\, \ln\left[E_{max}/(E_n + 7.34)\right]}{\int\limits_0^{E_{max}-7.34} \ln\left[E_{max}/(E_n + 7.34)\right] \mathrm{d}E_n} \tag{2.8}$$

The first term in the spectrum equation describes the evaporation neutrons whereas the second term is associated with direct neutrons. E_n is the neutron energy, T is the nuclear temperature in MeV ($T = 0.5$ MeV in tungsten), and E_{max} is the maximum photon energy generated by the linac when operating. The value of 7.34 MeV corresponds to the average binding energy of the emitted neutron for tungsten [29]. For example, in the case of a linac producing maximum x-ray energies of 25 MeV, the photoneutron emission spectrum becomes :

$$N(E_n) = 3.5716\, E_n \exp(-2E_n) + 0.0123607 \ln\left(\frac{25}{E_n + 7.34}\right) .$$

The spectrum plot, supposing a point isotropic neutron source in place of the complex geometry of a linac head, is presented in figure 2–5. In addition to the primary spectrum obtained from the analytical relation, this figure also includes the Monte-Carlo simulated photoneutron spectrum resulting from interactions with a tungsten sphere of 10 cm diameter surrounding the point neutron source [30]. Note that as previously mentioned, the spherical approximation of the linac head is accepted by advisory organizations such as the NCRP as well as by numerous research groups [31] [32]. The former has discussed the behaviour of photoneutron spectra before and after interaction with the linac head in its 1984 report on the neutron contamination from medical linacs [26]. Figure 2–6 taken from this report clearly shows the effect of the 10

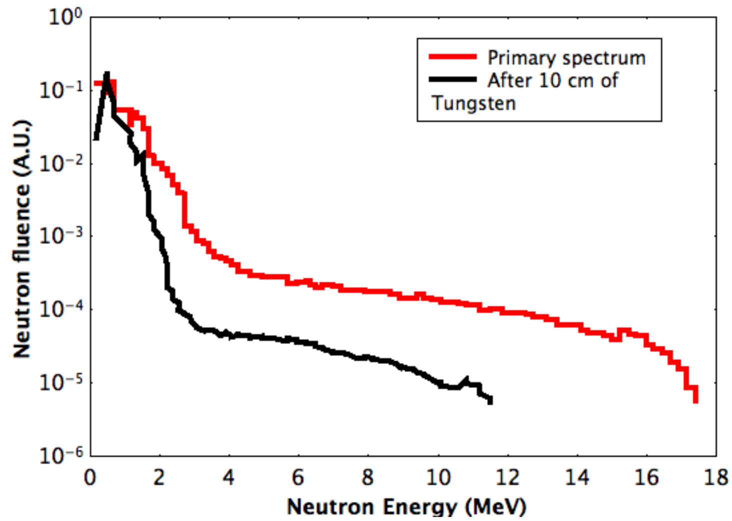

Figure 2–5: Primary and transmitted photoneutron spectra through a 10 cm radius tungsten sphere. Based on equation 2.8 for a 25 MV photon beam. Partially reproduced from [30].

cm tungsten sphere on the integral photoneutron spectrum. Different in form, this particular representation of energy distribution - also known as integral spectrum - has a vertical axis that indicates the fraction of neutrons with energies superior to the corresponding energy value on the horizontal axis. It is clear that there is some reduction of the portion of high-energy neutrons after crossing the tungsten sphere. There is also a reduction in the portion of relatively low energy ($\leq$ 0.1 MeV) neutrons to the benefit of even lower energy neutrons not seen with this specific scale. In other words, before crossing the sphere, 100% of neutrons (all) had energies above 0.1 MeV, whereas only 85% of neutrons transmitted through the shielding are more energetic than 0.1 MeV. This energy degradation becomes a first shielding obstacle against photoneutrons, with average neutron energy decreasing from $\sim$1.1 MeV to $\sim$0.7 MeV and from $\sim$2 MeV to $\sim$1.7 MeV after neutrons pass through head shields of 10 cm tungsten and 6.4 cm lead, respectively [6] [26].

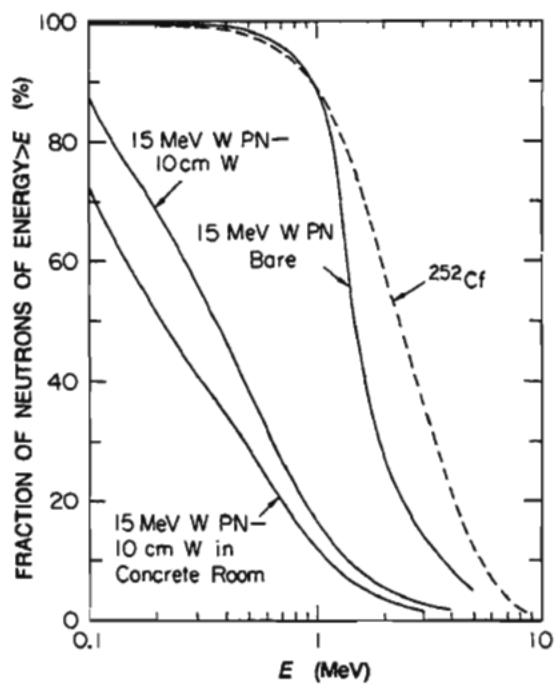

Figure 2–6: Integral photoeneutron spectrum for 15 MeV electrons striking a tungsten target (designated 15 MeV W PN bare). Also shown are the Monte-Carlo spectra obtained when 10 cm of tungsten shielding surrounds the tungsten target and when this assembly is placed in a concrete room. Reproduced from [26] and based on data from [33].

2.3.2 Neutron detection for radiotherapy facilities

The fundamental concept of neutron detection is based on the conversion of an incident neutron into a charged particle, the latter being easier to detect because of its charged nature (subject to Coulomb interactions). Neutron monitoring inside the linac bunker may be performed to determine neutron leakage form the accelerator head for shielding purposes, and to determine neutron equivalent dose in the patient plane, both inside and outside the primary photon beam. This often follows the requirement from regulatory agencies to perform shielding integrity radiation surveys during commissioning of linacs. Although barriers composed of hydrogenous materials (such as concrete) usually provide adequate shielding for photons and neutrons, spot checks outside these barriers are required by national agencies such as the CNSC. Moreover, for facilities operating above 10 MV - the photoneutron production threshold - the bunker door/ entrance (*i.e.* maze entrance) and all possible openings of the room, such as passages for electrical wires, must be checked for neutron contamination [5]. In photoneutron monitoring, the quantities of interest are neutron fluence, neutron equivalent dose (or more often ambient dose equivalent), dose equivalent rate, and the neutron spectrum [23]. As mentioned in chapter 1, fluence $\phi = \mathrm{d}N/\mathrm{d}a$, is the number of particles $\mathrm{d}N$ incident on a sphere of cross-sectional area $\mathrm{d}a$ and the unit is m^{-2} or cm^{-2}, whereas equivalent dose H (measured in sievert or rem) is the product of the radiation quality factor Q (or w_R in some textbooks [34]) and the absorbed dose D at a point in tissue, *i.e.* $H = QD = w_R D$. As for the ambient dose equivalent $H^*(d)$ at a point in a radiation field, the formal ICRP definition states that it is the equivalent dose that would be produced by the corresponding expanded and aligned field in the ICRU sphere at a depth d, on the radius opposing the direction of the aligned field. For strongly penetrating radiation, a depth of 10 mm is recommended [28]. The 10 mm is essentially the depth required for electron build-up to occur and for ambient dose-equivalent to represent a near-maximum dose. Ambient dose equivalent is also measured in sievert or rem.

Before getting into the description of various detection techniques, a brief quantitative description of relevant operational metrics would be helpful. Neutron measurements inside linac bunkers is challenging because of interference from primary and leakage photon beams, and also because the detection is spread over a large energy range, from thermal energies ($\simeq$0.025 eV) to the MeV range. This is problematic because a single detector is unable to probe neutron dose equivalent or fluence over such a large energy window. Most linacs operate at repetition rates between 100 and 1000 pulses per second with pulse widths of $\sim$1 to 10 μs [35]. Inside the primary beam the photon fluence is up to 4000 times higher than the neutron fluence, while outside the primary beam the photon leakage fluence is up to 100 times higher [5]. Peak electron currents may range from 20 to 120 mA per pulse in the photon mode and 3 to 15 mA per pulse in the electron mode. Therefore, active detectors are overwhelmed (saturated) by the intensity of the photon pulse and their measured readings become only an indication of the repetition rate of the accelerator. Another problem in mixed photon-neutron fields is that the neutron detectors can have photon-induced reactions, which cannot be separated from the neutron interactions themselves. Thus, only passive detectors should be used for measurements inside the room except at the outer maze entrance area where photon fluence is considerably reduced [5]. In terms of energy, room-scattered neutrons further soften the spectrum and outside the concrete room the average neutron energy is significantly lower than that inside the room. Most of the neutrons in the room are less than 0.5 MeV in energy, whereas the average energy of neutrons at the outer maze entrance (close to room entrance or door) is ~100 keV. Most of the neutron detectors are calibrated against a Plutonium-Berylium $\left(\overline{E}_n = 4.2\text{MeV}\right)$, Americium-Beryllium ($\overline{E}_n = 4.5$ MeV), or ^{252}Cf $\left(\overline{E}_n = 2.2\text{MeV}\right)$ neutron source [5]. Because the spectrum of fission neutrons from ^{252}Cf is similar to the typical photoneutron spectrum [36] and the shape of the photoneutron spectrum is independent of the incident electron energy, detectors calibrated against a ^{252}Cf source are adequate for neutron measurements inside the primary beam [36].

Finally, two reactions are key in slow neutron detection methods and although one was briefly introduced at the beginning of this chapter, they will both be described with more detail here. Indeed, slow neutrons are of particular significance in present-day nuclear reactors and much of the instrumentation that has been developed for this energy region is aimed at the measurement of reactor neutron flux.

The boron-neutron reaction for photoneutron detection

Probably the most popular reaction for the conversion of slow neutrons into directly detectable particles is the ${}^{10}_{5}\text{B}\,(n,\alpha)\,{}^{7}_{3}\text{Li}$ reaction shown in equation 2.3. The Q-value of the reaction is very large compared with the incoming energy of the slow neutron. Thus the large reaction energy submerges the much smaller kinetic energy of the incoming neutron, and it becomes therefore impossible to obtain precise information on the value of the particle's original energy. Moreover, the reaction products show a net momentum that is almost equal to zero because the incoming neutron momentum is very small (by conservation of momentum). Consequently, the two reaction products are emitted in exactly opposite directions and the energy is always shared in the same manner. The individual energies of the alpha particle and lithium nucleus can be calculated by simple conservation principles and yield for the case of a reaction leaving

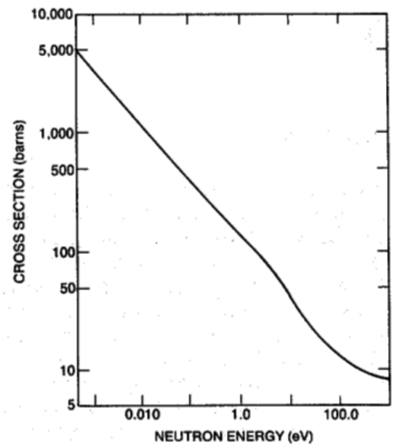

Figure 2–7: Boron-10 cross-section for low energy neutrons. Reproduced from [37].

Li in its excited state (the predominant case with thermal neutrons)

$$E_{Li} = 0.84 \text{ MeV} \quad \text{and} \quad E_{\alpha} = 1.47 \text{ MeV}\,. \tag{2.9}$$

The thermal neutron cross-section for the ${}^{10}_{5}\mathrm{B}\,(n,\,\alpha)\,{}^{7}_{3}\mathrm{Li}$ reaction is 3840 barns and it drops rapidly with increasing neutron velocity (or energy) following a $\sim 1/v$ trend [21], as shown in figure 2–7. The utility of this reaction stems from its large cross-section for thermal neutrons and from the fact that boron is readily available with the natural isotopic abundance of ^{10}B being 19.8%.

The helium-neutron reaction for photoneutron detection

The gas ^{3}He is also widely used as a detection medium for neutrons through the reaction

$${}^{3}_{2}\mathrm{He} + {}^{1}_{0}\mathrm{n} \rightarrow {}^{3}_{1}\mathrm{H} + {}^{1}_{1}\mathrm{p} \quad Q = 0.764 \text{ MeV}\,. \tag{2.10}$$

For reactions induced by slow neutrons, the Q value is shared by oppositely directed reaction products with energies

$$E_p = 0.573 \text{ MeV} \quad \text{and} \quad E_{^3H} = 0.191 \text{ MeV}\,.$$

The thermal neutron cross-section for this reaction is 5330 barns, significantly higher than that for the boron reaction, and its value is also inversely proportional to the neutron energy. Although ^{3}He is commercially available, its relatively high cost and limited supply are hindrances to its more mainstream use [21].

2.4 Neutron detectors

Neutron monitoring techniques for radiotherapy facilities consist of active and passive methods. Active methods include the use of dose and fluence meters. Passive methods include the use of activation foils, thermoluminescent dosimeters (TLDs), solid-state detectors, and bubble detectors [5].

Active neutron monitoring consists of slowing down fast neutrons or moderating them until they reach thermal energies. A thermal detector is then used to detect the thermal neutrons and measure dose-equivalent (known as rem-meter) or fluence (known as fluence meter). The response of a rem-meter is shaped to fit an appropriate fluence to dose-equivalent conversion coefficient over a given energy range. Modern designs of rem-meters comply with ICRP effective dose recommendations [24] and the operational quantity appropriate for rem-meter calibration is ambient dose equivalent $[H^{*}(10)]$ [28] which is defined in equation 2.11 :

$$H^{*}(10) \;= \int h_{\phi}(E)\,\phi(E)\,\mathrm{d}E \tag{2.11}$$

where $h_{\phi}(E)$ is the fluence to ambient-dose-equivalent conversion function, and $\phi(E)$ is the neutron fluence as a function of energy for a particular neutron field. The relation between h_{ϕ} and neutron energy E is shown in figure 2–8, where it is clear that low energy neutrons have a smaller contribution to ambient dose equivalent than the higher energy neutrons. The rem-meter

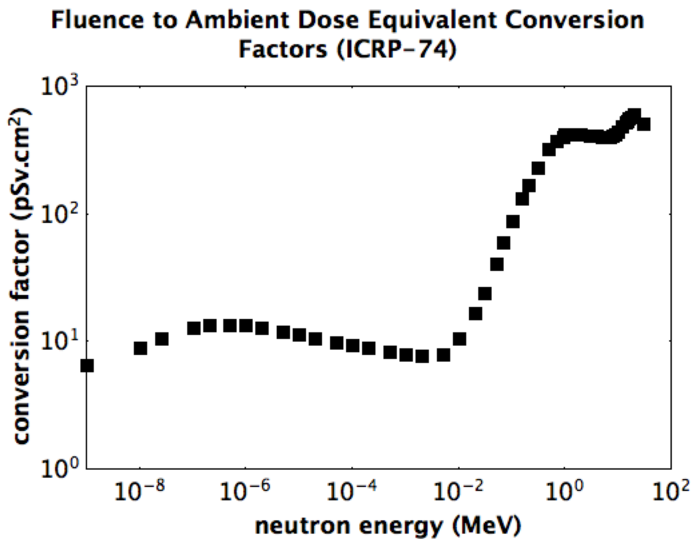

Figure 2–8: Fluence to ambient dose equivalent conversion coefficients. Reproduced from ICRP report 74 [28].

response (R_m) in that field is given by equation 2.12 :

$$R_m = \int C\, r_\phi(E)\, \phi(E)\, \mathrm{d}E \tag{2.12}$$

where $r_\phi(E)$ is the response function of the rem-meter in counts per unit fluence, and C is the calibration constant in units of sievert per count. As the comparison of both equations shows, the rem-meter measurement will be considered accurate if $r_\phi(E)$ has a similar energy response to that of $h_\phi(E)$ and the ratio $r_\phi(E) \,/\, h_\phi(E)$ defines the energy response of the rem-meter in terms of counts per unit dose equivalent. The obvious problem is that this ratio is not constant over much of the energy range and therefore the detector will be adapted to only specific energy windows [5].

Most commercial rem-meters consist of a hydrogenous neutron moderator material such as polyethylene, surrounding a thermal neutron detector. These detectors are based on the ^{10}B and ^{3}He reactions described previously. In simple terms, the moderator's role is to slow down the fast and intermediate

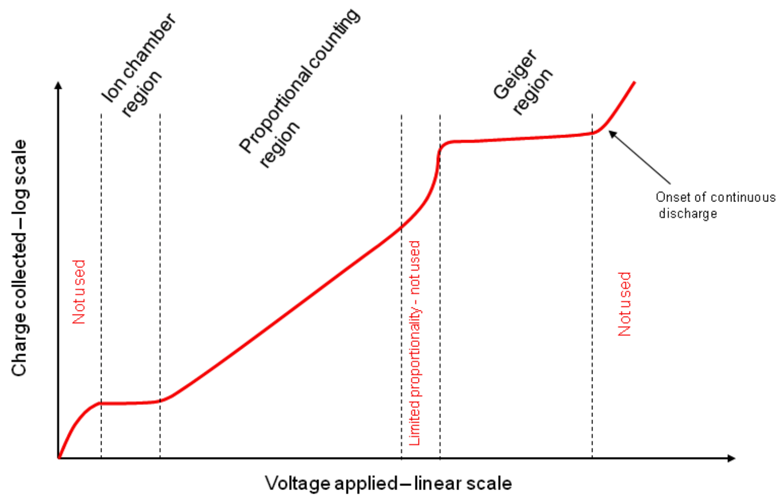

Figure 2–9: Relative level of ion-pair current vs. voltage applied for a wire cylinder ionization detection system with constant incident ionizing radiation. Reproduced from Wikipedia [38].

energy neutrons until they can be detected by thermal neutron detectors. A description of detectors based on both of these reactions follows.

2.4.1 Detectors based on the boron reaction

The BF_3 proportional tube is used for slow neutron detection. In this device, boron trifluoride serves both as the target for slow neutron conversion into secondary particles as well as a proportional counter gas. As its name indicates, the proportional counter is used to count particles of ionizing radiation and is categorized as a type of gaseous ionization detector. Its main advantage lies in that it can measure the energy of various types of radiation and discriminate between them [21][10][38]. Figure 2–9 shows the relative position of the proportional region among various regions of gaseous ionization chambers. In all commercial detectors, the BF_3 gas is highly enriched in ^{10}B in order to increase efficiency through the latter's higher cross-section.

The ideal and real pulse-height spectra expected from a BF_3 tube are shown in figure 2–10. In the ideal case, the branching ratio between reactions leading to

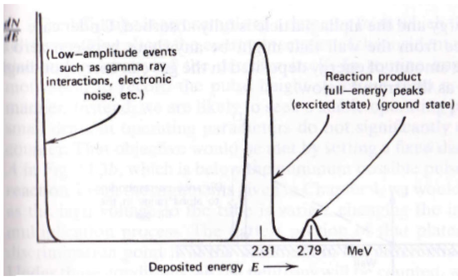

(a) Ideal spectrum

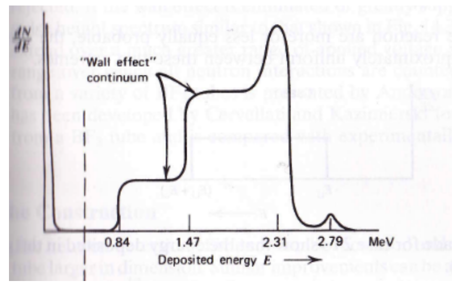

(b) Real spectrum

Figure 2–10: Pulse height spectra from BF_3 tubes. (*a*) Spectrum in which all reaction products are absorbed. (*b*) Real spectrum with additional points due to the wall effect. Reproduced from [21].

the ground state and reactions leading to the first excited state is 6:94 (*i.e.* the ratio of surface areas under the 2.31 MeV and the 2.79 MeV peaks should be 94:6, respectively). The non-ideal situation occurs because the size of the tube is no longer large compared with the range of the secondary particles, which might strike the chamber wall and produce a small pulse. The cumulative effect of this type of process is known as the *wall effect* and it is seen in any detector smaller than 1 cm in diameter (the practical range of alpha particles in the boron reaction) [21]. The BF_3 tube is an example of a detector from which the differential pulse height spectrum tells us nothing about the energy spectrum of the incident radiation but is a function only of the size and geometry of the detector itself.

Neutron detection efficiency can be improved and the wall effect minimized if the BF_3 tubes are made larger in dimension or if the pressure in the BF_3 gas is increased [21]. Nevertheless, the main challenge in the design of the gas-filled tubes remains γ ray discrimination. Gamma (γ) rays are often present together with the neutron flux and interact primarily in the wall of the counter and create secondary electrons. Note that electrons deposit only a small portion of their energy in the gas before reaching the opposite wall of the counter, because the stopping power for electrons in gases is low. The impact of γ rays on the pulse height spectrum will then take the form of low-amplitude and low energy pulses on the left tail of the spectra in figure 2–10. Thus, if the γ ray flux is low, simple amplitude discrimination can eliminate it without sacrificing neutron detection efficiency. Adversely, if the photon flux and its rate are sufficiently high, significant complications can arise such as large apparent peak amplitudes due to pulse pile-up. This can be controlled to some extent by choosing the right pulse-shaping time constant in the detector electronics. Short time constants can be seen as double-edged swords: they can reduce γ ray pile-up but may also decrease the neutron-induced pulse amplitude because of incomplete charge integration [21]. Because of pulse pile-up, manufacturers of active monitors (such as gas filled detectors) generally state photon rejection for steady fields and not pulsed fields, such as the ones associated with linacs [5].

Another application of boron in neutron detection can take the form of a solid coating on the interior walls of a proportional tube filled with a more suitable gas than BF_3. Indeed, ^{3}He proportional counters are more sensitive and more stable than BF_3 counters, but also more expensive. The optimal thickness of the boron layer will be determined with respect to the maximum range of the α particles from the boron reaction. The problem here is that because of the attenuation by the boron layer, the average energy deposited by neutron interactions will be considerably less than that for BF_3 tubes, and consequently the device's discrimination ability will also be lower [21].

2.4.2 Detectors based on the helium reaction

As seen previously, the cross section of the ${}^3_2\mathrm{He}\,(n,\,p)\,{}^3_1\mathrm{H}$ reaction is higher than that of the ${}^{10}_{5}\mathrm{B}\,(n,\,\alpha)\,{}^7_3\mathrm{Li}$ reaction, which makes it an attractive alternative for slow neutron detection. ^{3}He of sufficient purity can act as an acceptable proportional gas where each thermal neutron reaction would deposit 764 keV

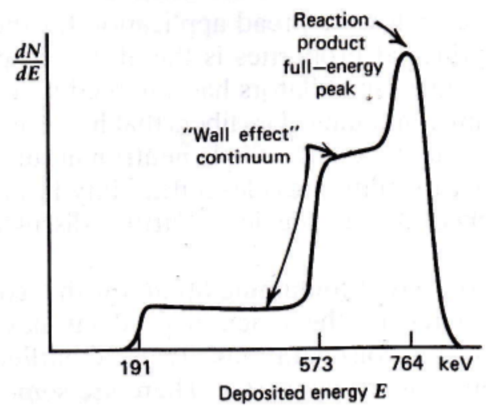

Figure 2–11: Real pulse height spectrum for a ^{3}He spectrum in which the wall effect is significant. Reproduced from [21].

in the form of kinetic energy of the triton and proton reaction products. As with the BF_3 tubes, the range of these products is often larger than the size of the ^{3}He tube, which results in the same previously mentioned wall effect. This is shown in figure 2–11 with a large tail left of the expected peak energy value of 764 keV. Notice that the discontinuities on the tail occur at energies corresponding to that of the proton (573 keV) and triton (191 keV). Note that the atomic mass of ^{3}He is lower than that of BF_3, which results in much longer ranges for the reaction products and a more significant wall effect in the case of the former. Methods to attenuate the wall effect include building larger tubes to allow neutron reactions to occur far from the walls as well as increasing the pressure of the ^{3}He gas in order to reduce the range of the charged particle reaction products. The latter objective is also attainable by adding a small amount of heavier gas - such as isobutane, krypton, or argon - to the helium in order to enhance the stopping power [21] [39].

As with BF_3 tubes, when the gamma irradiation rate is high, the pile-up of the resulting pulses can raise their amplitude to the point that a clean separation from the neutron-induced pulses is no longer possible. This is the case when the ^{3}He tube is placed in the linac room, where the pulsed mode photon flux is such that neutron detection becomes practically impossible.

The detectors described so far rely on the slowing down of a fast neutron in a moderating material before its detection as a thermal neutron. The moderating process eliminates all information on the original energy of the fast neutron and cannot be used if the goal is to obtain energy information. Furthermore, the detection process is relatively slow since the neutron must undergo multiple collisions with moderator nuclei, followed by diffusion as a thermal neutron before the detection signal is generated. As a consequence, such detectors cannot provide a fast detection signal required in many neutron detection applications [21].

This limitation can be overcome if the fast neutron induces a nuclear reaction without the moderation step. The reaction products will then have a total kinetic energy given by the sum of the incident neutron kinetic energy and the Q-value of the reaction. If the neutron energy is not too small compared to the Q-value, a measurement of the reaction product energies will yield the neutron energy by simple subtraction of the Q-value. Moreover, the detection process will be faster since the incoming fast neutron spends only a few nanoseconds in the active volume of the detector and a single reaction is sufficient to provide a detector signal [21]. The downside to fast neutron measurement is that cross-sections for fast neutron reactions are orders of magnitude lower than the corresponding thermal neutron cross-sections, and such detectors will inevitably show a much lower detection efficiency than their thermal neutron counterparts.

Although both helium-neutron and boron-neutron reactions are of importance in neutron spectroscopy and both are fundamentally similar, for reasons of brevity, only the former will be detailed here. The cross-section of the of the helium-neutron reaction falls off continuously with increasing neutron energy and there are a number of reactions that must be considered in detectors based on this type of reaction. The first is elastic scattering of the neutron from the helium nuclei, the cross-section of which is larger than the (n, p) reaction, especially for fast neutrons. For example, cross-sections for both reactions are equal at neutron energies of ∼150 keV, but elastic scattering becomes three times more probable at 2 MeV. In addition, a competing (n, d) reaction is possible for neutron energies exceeding 4.3 MeV, but becomes significant only at energies above 10 MeV [21].

The pulse height spectrum from a detector based on the ^{3}He reaction will show three distinct features. The spectrum, after the full energy of the reaction products is entirely absorbed in the detector, is shown in figure 2–12. First, at the right end of the spectrum, there is a full-energy peak corresponding to all the (n, p) reactions induced directly by the incident neutrons. The peak is centred at an energy equal to the neutron energy plus the Q-value of the reaction. Second, a pulse height continuum results from elastic scattering of the neutron and a partial transfer of its energy to a recoil helium nucleus with a maximum energy equal to 75% of the incident neutron energy. Third, an epithermal peak is seen at the beginning of the tail and centred around 0.764 MeV. This peak corresponds to the detection of incident neutrons that have been reduced to the thermal range by moderation in external materials and these interactions deposit an energy equal to the Q-value [21].

The spectrum shown in figure 2–12 is very similar to the spectrum that would be obtained with a large ^{3}He-filled proportional counter irradiated with fast neutrons. To minimize the wall effect, pressure is increased (to several atmospheres) and, as already mentioned, a heavier gas (usually krypton) is added

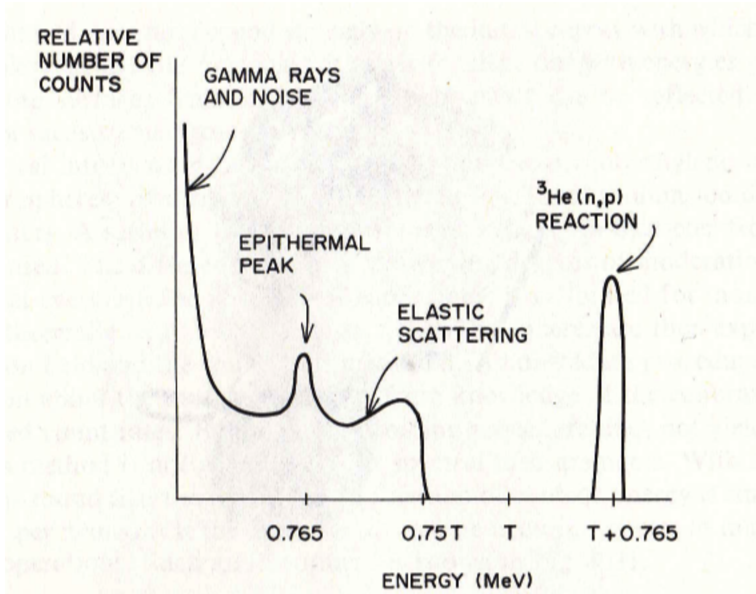

Figure 2–12: Pulse height spectrum expected from fast neutrons incident on a ^{3}He detector. Reproduced from [9].

to reduce reaction product ranges [40][41][42]. From the beginning, ^{3}He proportional counters had an added layer of complexity including two-dimensional storage of both amplitude and rise time information for each pulse as well as digital signal processing techniques that allow for a more selective choice of acceptance or rejection parameters [43]. Nevertheless, the pulse pile-up issue that leads to signal saturation remains an obstacle, and ^{3}He proportional counters cannot be used in the radiotherapy room because of the pulsed nature of the linac.

2.4.3 Bonner spheres

The last type of detector described here will be the Bonner Sphere spectrometer (BSS) developed by Bramblett, Ewing, and Bonner in 1960 [44]. The original BSS comprised a small thermal neutron detector (cylindrical ^{6}LiI (Eu) crystal, 4 mm diameter $\times$4 mm), positioned at the centre of a polyethylene sphere. Five spheres with diameters ranging from 2 to 12 inch were used in

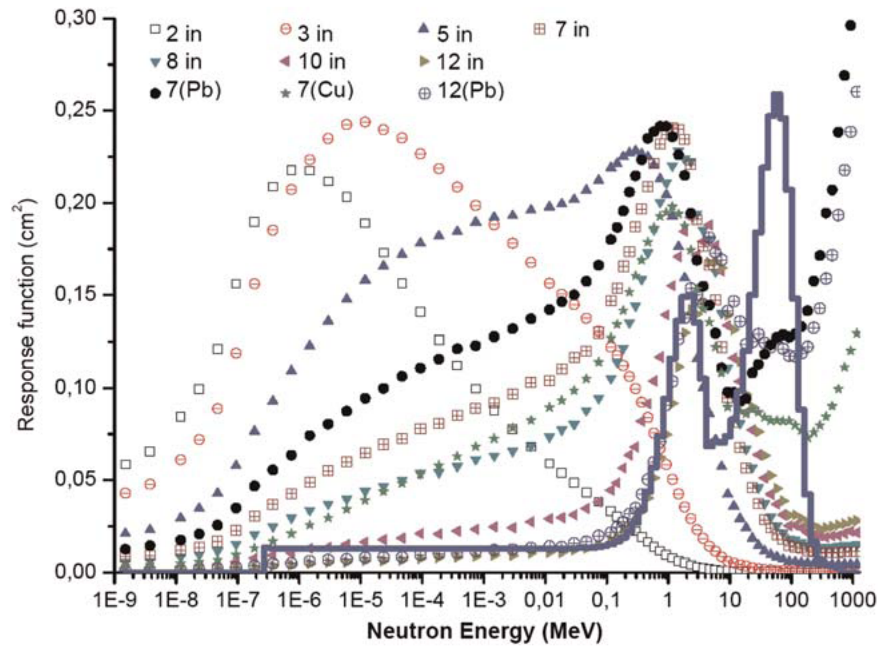

Figure 2–13: Typical response matrix of a BSS with extended range spheres superposed to a typical neutron spectrum of a high-energy field (continuous line). Reproduced from [45].

conjunction to form a detector system based on five different response functions. The response function is defined as the reading per unit fluence as a function of the monoenergetic neutron energy under uniform irradiation conditions and is usually derived by Monte-Carlo simulations [45][46]. Figure 2–13 shows the energy dependence of the detection efficiencies of BSS neutron detectors of various diameters up to 12 inches.

The difference in the shapes and position of the maxima in these response curves allows to measure the count rate of each sphere individually. An unfolding process can then provide the incident neutron energy distribution [21].

Modern versions of the BSS have more layers, which help determine relatively high energy resolution neutron spectra over a wide energy range. Moreover, using the same principle, investigators have also included different thermal neutron detectors as a substitute for the lithium iodide scintillator [47].

With the basics of neutron physics and the associated detection techniques reviewed, we can now focus on describing the analytical and numerical shielding methods devised by the health physics community for optimal design of radiotherapy bunkers.

Chapter 3
Shielding and radiation protection

Radiation shielding is a science in itself and an important branch of health physics. Academic journals such as the *Journal of Radiation Protection* and *Radiation Protection Dosimetry* frequently publish scholarly articles on shielding design and optimization in radiotherapy rooms. In this chapter, following a description of the milestones that led to the development of radiation protection and shielding science, the focus will be directed on present day shielding methodologies and formalisms. In order to stay relevant to the subject of this thesis, the description of key radiation shielding concepts and formula will be limited to those pertaining exclusively to neutrons.

3.1 Brief history of shielding and radiation protection

Radiation shielding is a little more than a century old and related thorough reviews can be found in many books and articles [48][6][49]. The history of shielding begins shortly after Roentgen discovered x-rays in 1895, when skin burns and eye irritation were observed and within a few years it was generally accepted that exposure to x-rays was harmful. From then on, shielding techniques and devices were developed and became essential components of radiation applications. It was first observed that lead was effective in stopping x-rays and that film could be used to detect x-rays for health protection [50]. The development and growing popularity of the Coolidge tube introduced a need to better structure the field of radiation protection and a first attempt was made in 1921 by the *X-Ray and Radium Protection Committee* in Britain. Their first report emphasized the use of lead for beam attenuation and distance to reduce exposure. Among the suggestions was to place the tube in a metal case and to use lead in the walls of the room to protect operators. The next step was the formation of the *International Committee on X-Ray and Radium Protection* in 1928, which was later renamed the *International Committee on Radiation Protection - ICRP*. The first report issued by this committee was the U.S. Bureau of Standards Handbook No. 15 in 1931 [51], which included a simple table summarizing minimum lead thicknesses for radiation energies between 75 kV and 600 kV. It was also at this time that the concept of the primary barrier was introduced and it was decided, for additional security purposes, that it extend one foot beyond the maximum beam size, a rule of thumb still used today. In 1953, with the advent of the first linac, the U.S. *National Council on Radiation Protection and Measurements - NCRP* (formed in 1946) and the *International Commission on Radiation Units and Measurements - ICRU* decided to impose a permissible dose limit of 5 R per year [52].

Modern North American radiation therapy physicists use various publications from the NCRP [5] [53] [54] [26] for basic shielding calculations pertaining to all types of radiation. Report 79 ([26]) in particular focuses on neutron shielding and contains additional information about mazes used to moderate neutrons. Present-day shielding methods, as summarized in NCRP report 151 [54], rely on data and simple deterministic equations to design shielding for medical facilities that use megavoltage linacs. Complications arise above energies of about 10 MeV when neutrons are produced as will be detailed later in this work.

In Canada, the *Atomic Energy Control Act* of 1946 paved the legal way for the establishment of the *Atomic Energy Control Board - AECB*, with its main purpose being to assist the Canadian government in matters related to radiation regulation, research, and mining. The AECB was replaced by the *Canadian Nuclear Safety Commission - CNSC* in 2000 after the *Nuclear Safety Control Act*, was passed by parliament in 1997.

All of the above mentioned efforts aim to prevent harmful non-stochastic effects and to reduce the probability of stochastic effects to acceptable levels [24]. The prevention of non-stochastic effects is achieved by setting equivalent-dose limits. In the context of this work that focuses on radiotherapy pertaining to neutrons, the way to reach these objectives is to design suitable bunkers. The designer must have an in-depth knowledge of the materials and techniques detailed in the following NCRP reports:

- Report 49 - Structural Shielding Design and Evaluation for Medical Use of X Rays and Gamma Rays of Energies up to 10 MeV (1976) [53]. Superseded by NCRP 151,
- Report 51 - Radiation Protection Design Guidelines for 0.1-100 MeV Particle Accelerator Facilities (1977) [54]. Superseded by NCRP 151,
- Report 79 - Neutron Contamination from Medical Electron Accelerators (1979) [26]. Superseded by NCRP 151,
- Report 144 - Radiation Protection for Particle Accelerator Facilities (2003) [55], and
- Report 151 - Structural Shielding Design and Evaluation for Megavoltage X- and Gamma-Ray Radiotherapy Facilities (2005) [5].

Two exhaustive technical documents published by advisory organizations are today considered to be the references in the field of shielding for medical radiation facilities. The first is report No. 47 [56] of the IAEA (International Atomic Energy Agency) and is entitled *Radiation protection in the design of radiotherapy facilities*. The other is report No. 151 [5] of the NCRP. At the

McGill University Health Centre (MUHC), and generally in North-American institutions, the document of choice is usually report No. 151 of the NCRP.

3.2 Neutron transport in concrete rooms: analytical models

Monte-Carlo (MC) derived models of the effects of concrete walls on photoneutron spectra were investigated starting from the late 1970s [36]. Some of these early studies are shown on figure 2–6, where one of the four curves indicates an increase in the proportion of low-energy neutrons scattered from the concrete walls. This has direct repercussions on shielding design and is one example of how simulation information can eventually lead to optimization of shielding methodology. This section will focus on explaining the behaviour of photoneutrons in the linac bunker.

As seen in figure 1–1, typical high-energy radiotherapy rooms have a rectangular shape with a maze to reduce the dose rate of the radiation field at the entrance to the bunker. In the case of linacs that also produce neutrons, the maze is also key in moderating neutron energies by the time they reach the door or entrance of the room. It essentially becomes a secondary barrier that increases the interaction surface for the neutrons to undergo more elastic and inelastic interactions. Its main purpose is to keep the bunker doors as light as possible and perhaps, depending on specific architectural or engineering constraints, to entirely eliminate them from the room design. Since the central area of the room is shielded with thick ($\sim$8 and 4 feet [5]) concrete walls that are sufficient for neutrons, the most challenging aspect of neutron shielding occurs in the maze and in the vicinity of the door or the entrance. Generally, maze design is divided in two separate categories: low-energy accelerators ($\leq$ 10 MV) and high-energy accelerators ($>$ 10 MV) since there are considerable differences in the secondary radiation types and fluences produced in each of these cases. Since neutrons are generated at energies $\gtrsim 10$ MV, only such mazes will be studied and referred to in this work.

Another simplified but typical diagram of a room layout is given in figure 3–1, where the various parameters serve to quantify the neutron dose distribution along the maze. Since the average energy of the neutron capture gamma rays from concrete is 3.6 MeV [57], a maze and door that provide sufficient shielding for the neutron capture gamma rays will also be adequate for scattered photons from the linac head. More precisely, for mazes in high-energy accelerator rooms, where the distance from A to B in figure 3–1 is > 2.5 m, the photon field is dominated by neutron capture gamma rays and the scattered photon component can be ignored [5]. Moreover, it was found that the photon dose equivalent outside the maze door changes only slightly when the collimator of the accelerator is adjusted from maximum size to the closed position or when the scattering phantom is removed from the beam [58], implying that scattered photons have little influence on dose around and beyond the room entrance. Hence, shielding considerations in the maze and around the door may be exclusively based on the capture reaction photons and photoneutrons [5].

3.2.1 Neutron capture photon equivalent-dose at the maze door

A method for estimating neutron capture photon equivalent-dose at the treatment room door was given by McGinley in 1995 [48][5]. It links equivalent-dose (h_φ) from the neutron capture gamma rays at the outside maze entrance (point B in figure 3–1) to a unit of absorbed dose of x-rays at the isocentre through equation 3.1 :

$$h_\varphi \;=\; K\, \varphi_A\, 10^{-\left(\dfrac{d_2}{TVD}\right)}, \tag{3.1}$$

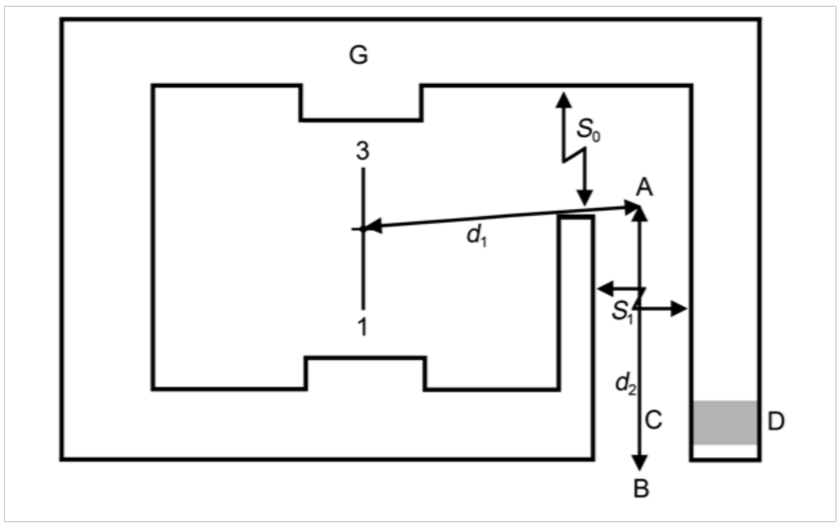

Figure 3–1: Linac bunker diagram for calculating neutron capture gamma-ray and neutron equivalent dose at the maze door. Reproduced from [5]

.

where, as mentioned in report 151 of the NCRP:

K = ratio of neutron capture gamma-ray equivalent-dose (Sv) to total neutron fluence at location A in figure 3–1. The average value of K is $6.9 \times 10^{-16}\,\mathrm{Sv} \cdot \mathrm{m}^2$ per unit neutron fluence based on measurements from 22 accelerator facilities [5],

φ_A = total neutron fluence m^{-2} at location A per unit absorbed dose (gray) of x rays at the isocenter,

d_2 = distance from location A to the door (meters), and

TVD = tenth-value distance with a value of ∼5.4 m for x-ray beams in the range of 18 to 25 MV, and a value of ∼3.9 m for 15 MV x-ray beams [5].

The total neutron fluence at the inside maze entrance (location A in figure 3–1) per unit absorbed dose from x-rays at the isocenter is then given by equation 3.2 [59][26] :

$$\varphi_A \;=\; \phi_{dir} + \phi_{sc} + \phi_{th} = \frac{\beta Q_n}{4\pi d_1^2} + \frac{5.4\beta Q_n}{2\pi S_r} + \frac{1.3 Q_n}{2\pi S_r}\,. \tag{3.2}$$

In equation 3.2 the three terms represent the direct (ϕ_{dir}), scattered (ϕ_{sc}) and thermal (ϕ_{th}) neutron components, respectively. The $1/(2\pi)$ in the scattered and thermal neutron terms accounts for the fraction of the neutrons that enter the maze [5]. The other parameters are, as mentioned in NCRP report 151:

β = transmission factor for neutrons that penetrate the head shielding (1.0 for Pb and 0.85 for W),

d_1 = distance in meters from the isocenter to location A in figure 3–1,

Q_n = neutron source strength. Measured by neutrons emitted from the accelerator head per gray of x-ray absorbed dose at the isocenter, and

S_r = surface area of the treatment room in m^2.

Equation 3.2 was first derived in 1979 [36] and is based on Monte-Carlo (MC) simulations. Although MC was and remains the gold standard to obtain photoneutron distributions in any setting, the fact that it was initially unavailable to most radiation safety officers prompted investigators to also derive simple analytical formulas from their MC results. This would make our understanding of neutron transport in concrete rooms an easier task. As a result, it was found that the photoneutron field could be described by equation 3.2 as the sum of neutrons originating directly from the source (the linac head), a component scattered from the walls, as well as a contribution of the thermal (low energy) neutrons. The direct component, ϕ_{dir} follows the inverse square law, whereas the scattered ϕ_{sc} and thermal components ϕ_{th} were found to be constant throughout the room [26].

Neutron source strength ($\mathrm{Q_n}$) values for a number of accelerators and nominal energies are given in Table B.9 of NCRP report 151 and are based on studies performed by two groups in the early 2000s [60][6].

3.2.2 Neutron equivalent dose at the maze door

The maximum neutron fluence is obtained by closing the collimators which implies that most photoneutrons originate in the head of treatment accelerators [61][62]. The neutron field in the maze is also a function of the gantry angle and location of the target rotational plane in the treatment room. It was found that the neutron level at the treatment room door was maximum when the gantry angle was aligned along the horizontal line marked 3 - 1 in figure 3–1 and the head is closer to the inner maze entrance (point A). More specifically, for the same room layout, the neutron dose equivalent at the maze door was found to vary by a factor of two as the gantry angle was changed [63].

The neutron dose equivalent at the outer maze entrance is determined using one of several analytical techniques outlined below. All these techniques are based on the concept of the tenth-value distance (TVD) first introduced in 1967 by Maerker and Muckenthaler [64] and refering to the fall-off of the thermal neutron fluences through mazes and large ducts. Later on, it was reported that the TVD is roughly equal to three times the square root of the product of the height times the width of the opening and that each additional turn in the opening (at the level of the outer maze entrance - point B) would decrease the fluence roughly another three-fold [54].

Kersey's method

Although no longer used, one of the earliest techniques for evaluating neutron fluence at the entry of a maze was given by Kersey in 1979 [65] and it served as a basis for the development of more accurate models. In this approach, the effective neutron source position is taken to be the isocenter of the accelerator and the neutron equivalent dose ($H_{n,D}$) at the outside maze entrance per unit absorbed dose of x-rays at the isocenter is given by equation 3.3 :

$$H_{n,D} \;=\; H_0 \left(\frac{S_0}{S_1}\right)\left(\frac{d_0}{d_1}\right)^2 10^{-\left(\frac{d_2}{5}\right)}, \tag{3.3}$$

where, as mentioned in NCRP 151:

$H_{n,D}$ is the neutron dose equivalent at the maze entrance in sievert per unit absorbed dose of x-rays (gray) at the isocenter and thus the constant has units of $\mathrm{Sv} \cdot \mathrm{n}^{-1} \cdot \mathrm{m}^2$,

H_0 is the total (direct + room-scattered + thermal) neutron dose equivalent at a distance d_0 (1.41 m) from the target per unit absorbed dose of x-rays at the isocenter ($\mathrm{mSv} \cdot \mathrm{Gy}^{-1}$). This value is given in Table B.9 of NCRP report 151 [5],

$\frac{S_0}{S_1}$ is the ratio of the inner maze entrance cross-section area to the cross-section area along the maze (see figure 3–1),

d_1 is the distance in meters from the isocenter to the point on the maze centerline from which the isocenter is barely visible (point A), and

d_2 is the distance in meters from A to B and in the case of a maze with two bends, it refers to the distance from A to C plus the distance from C to D (see figure 3–1).

More than a decade later, it was found through a study of 13 accelerators that the ratio of the neutron equivalent dose calculated by use of Kersey's method to the measured neutron equivalent dose varied from 0.82 to 2.3 [63]. The same study reported that the TVD for maze neutrons was ∼16 % less than 5 m, implying that 5 m is a conservative safe value to use for neutron TVD when dose equivalent is determined at the maze outer entrance. Moreover, measurements showed that a second turn in the maze reduced neutron dose by a factor of at least three as compared to the value obtained by Kersey's equation. As a consequence of these significant differences found between Kersey's method and experimental results, improved and more accurate versions of equation 3.3 were developed in the early 2000s.

Modified Kersey's method (or McGinley method)

Wu and McGinley introduced equation 3.4 in 2003 [66], which gives the neutron dose equivalent along the maze length in the form of two exponential functions :

$$H_{n,D} \;=\; 2.4 \times 10^{-15}\, \varphi_A \sqrt{\frac{S_0}{S_1}} \left[1.64 \times 10^{-\left(\frac{d_2}{1.9}\right)} \;+\; 10^{-\left(\frac{d_2}{TVD}\right)} \right] , \qquad (3.4)$$

where all parameters have already been defined in equations 3.1, 3.2, and 3.3. It was also reported by the same authors that the tenth-value distance (TVD) varied as the square root of the cross-sectional area along the maze S_1 (m^2) in the following form:

$$TVD \;=\; 2.06\sqrt{S_1}\,.$$

Equation 3.4 is the most widely accepted analytical expression for calculation of the neutron dose at the entrance of linac bunkers. The total weekly dose equivalent at the maze door (H_w) is then the sum of all the components from the leakage and scattered radiations (H_{tot}), the neutron capture gamma rays (H_{cg}), and the neutrons (H_n) :

$$H_w \;=\; H_{tot} + H_{cg} + H_n \;=\; H_{tot} + (W_L \cdot h_\varphi) + (W_L \cdot H_{n,D}) \;,$$

where W_L is the weekly leakage-radiation workload measured in $\mathrm{Gy} \cdot \mathrm{week}^{-1}$, whereas h_φ and $H_{n,D}$ are as defined in equations 3.1 and 3.4, respectively. For most mazes, where energies above 10 MV are used, H_{tot} is an order of magnitude smaller than the sum of H_{cg} and H_n, and is therefore negligible [5].

3.2.3 Door shielding

Shielding of maze doors for scattered and leakage photons is relatively simple and explained in report 151 of the NCRP. However, as previously mentioned, the scattered and leakage dose equivalents are low compared with photoneutron and neutron capture gamma rays that become possible above linac energies of 10 MV [58]. Average energy for the latter varies between 3.6 MeV and 10 MeV (for very short mazes), whereas the former have an average energy of ~100 keV which corresponds to a polyethylene TVL of 4.5 cm [26]. Alternatively, as explained in section 2.1.5, borated polyethylene (BPE) (5 % by weight) can also be used and it is much more effective for shielding against thermal neutrons compared with polyethylene with no boron. Indeed, the TVL for BPE is 3.8 cm for 2 MeV neutrons and 1.2 cm for thermal neutrons, but for safety purposes, it is recommended to that a TVL of 4.5 cm be used in calculating the BPE thickness requirements [5].

Most bunkers with maze lengths on the order of 8 m or greater require 0.6 to 1.2 cm of lead and 2 to 4 cm of BPE for shielding in the door and a widely suggested Lead/BPE arrangement is: lead, BPE, lead. The lead on the source side of the BPE is to further reduce the energy of the neutrons (after they have already lost most of their energy along the maze) by inelastic scattering (sec. 2.1.4) and make the BPE more effective in shielding against, at that point, almost exclusively thermalized neutrons. The lead on the outside of the BPE will serve to attenuate the neutron capture gamma rays from the BPE but is often unnecessary when the maze is long enough to attenuate neutrons sufficiently before they encounter the door [67]. Figure 3–2 offers a simplified diagram of the door and summarizes its role in stopping neutrons.

As we conclude the analytical section of the shielding calculations, it is worth mentioning that although numerical methods have recently made gains in popularity and that the formulae described in this section can significantly lack in accuracy and precision [30], they nevertheless continue to be widely used by radiation safety officers.

3.3 Monte-Carlo simulations for neutron shielding

A detailed explanation of the Monte-Carlo (MC) technique or a review of all types of radiation related MC simulation codes and methods would clearly go beyond the scope of this work. Instead, this section will focus on describing the basic tenets and specificities of neutron transport MC simulation and offer a brief review of the research done in this specific field. For the reader who would be totally unfamiliar with the field of MC modelling in EBRT, Verhaegen and Seuntjens [68] have produced an exhaustive topical

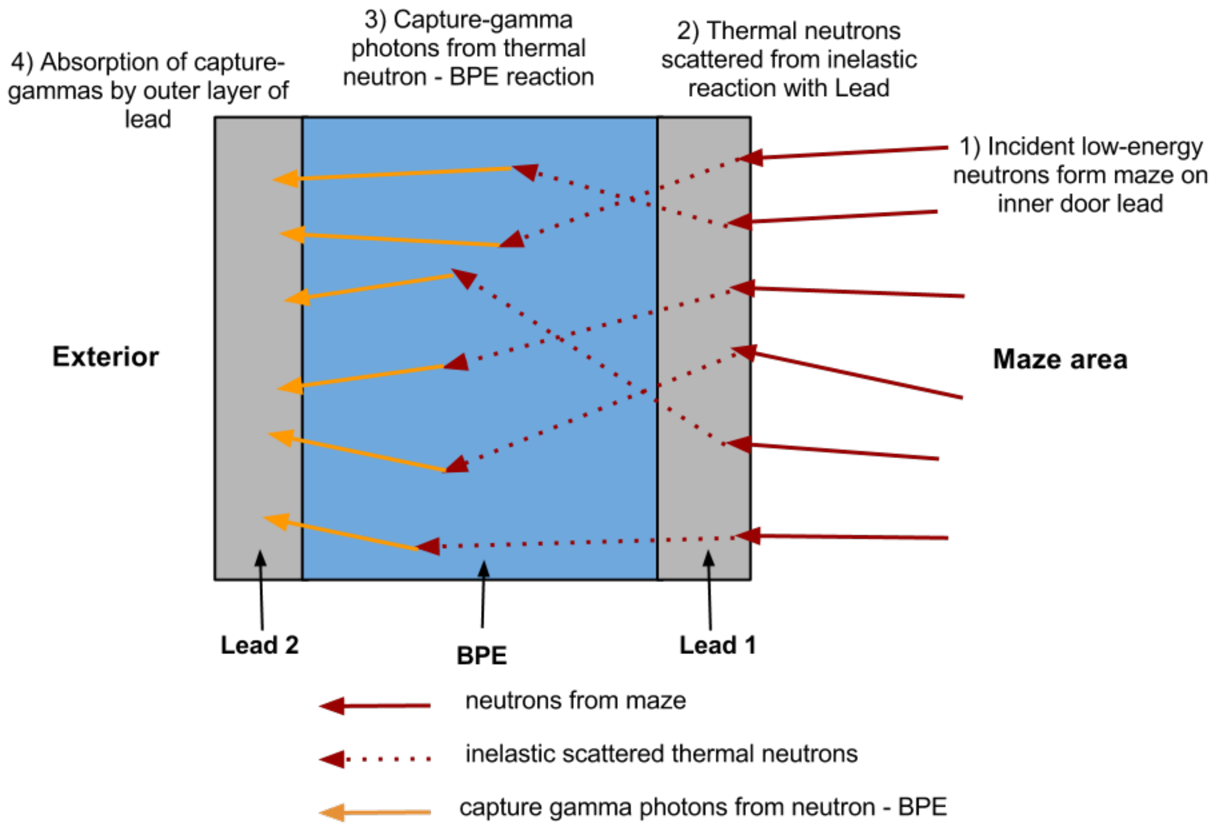

Figure 3–2: Qualitative high-energy linac bunker door diagram (layer thicknesses not proportional). (1) Low energy neutrons at the end of the maze undergo inelastic scattering reactions in a first layer of lead. (2) Resulting scattered thermal neutrons interact with a borated polyethylene (BPE) layer through the neutron capture reaction. (3) Capture-gamma photons are generated in the BPE. (4) The photons are absorbed by the outer layer of lead.

review that covers the history of MC and offers a description of the available codes.

Initially developed in the 1940s, MC techniques were applied to medical physics in the 1970s but remained limited to very simple radiation geometries because of the low computing power available at the time. Beginning from the mid 1990s, the number of MC studies has significantly increased due to a parallel increase in computing speed, the advent of cheaper computer cluster technology, and an enhanced flexibility offered by numerous MC codes [68]. Numerous papers began describing MC models for complete linac heads (as seen in figure 3–3) including complex components such as multi-leaf collimators (MLC) [69] and MC-based treatment planning systems were already presented by the late 1990s [70][71]. It is now accepted that the MC method is the gold standard for modelling radiation transport for radiotherapy applications. Without overstating its potential, it would be safe to say that its current status is such that MC is expected to play an crucial role in future radiotherapy and imaging tools, not only in research but also in a practical clinical setting [68].

In the specific case of neutrons, the overwhelming majority of MC simulation studies pertain to the shielding domain and only a limited number of publications focus on neutron dosimetry during EBRT. Neutrons are a concern to the patient only when it comes to dose delivered to healthy tissue surrounding the treatment target. In IMRT, this can be problematic since more monitor units may be required, increasing thus effective dose to organs that are outside the beam [72]. Although IMRT is mostly performed with 6 MV beams with insignificant neutron production, situations where higher energies can be used deserve dedicated simulation studies and/or validation [68]. The code MCNP5 (Monte Carlo N Particle transport code [73]) with its integrated neutron cross-section libraries becomes an indispensable tool for the generation

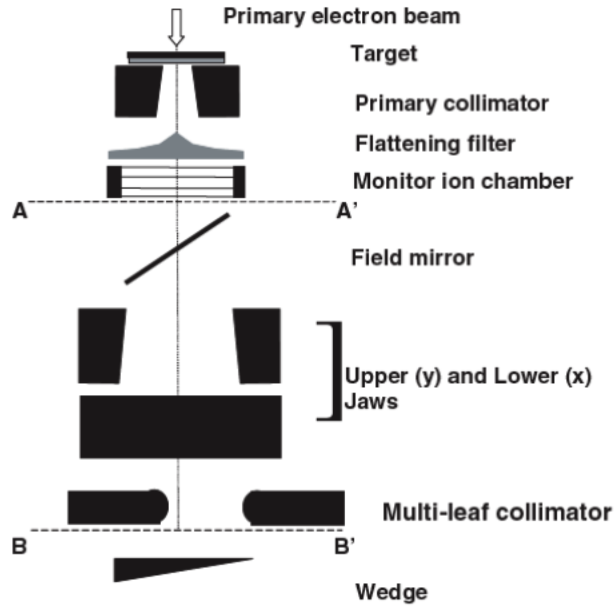

Figure 3–3: Simplified view of the various components of a linac head as modelled for Monte Carlo simulations. Reproduced from [68].

and tracking of photoneutron transport. This is the code that was used in this work and references to MC will from here on refer to simulations performed with the specificities of MCNP5.

The need to use MC simulations for neutron shielding essentially arises from the insufficient flexibility and the simplicity associated with the previously described analytical models. Although these equations offer a quick and less error-prone design solution, they also simplify shielding to the point that significant discrepancies can occur between radiation measurements and analytical calculations. Even if the equations are considered accurate because they are obtained by fitting mathematical expressions to MC simulation results (see section 3.2), they lack robustness and/or flexibility in that the slightest modification to the room geometry would perturb the model by degrading its reliability. This is because the fundamental physics is not accounted for and analytical equations are based exclusively on macroscopic trends. The risk here is more often to over-shield - and consequently spend more resources than necessary - than to under-shield, since the conventional models are conservative whereas MC is much more representative of reality.

3.3.1 Review of studies on MC simulations of photoneutrons

Since the 1990s numerous groups have used the MC method to study a multitude of aspects pertaining to radiotherapy photoneutron dosimetry and shielding. This section presents notable studies and breakthroughs in linac room photoneutron dosimetry and maze/door shielding.

MC simulations related to photoneutron dosimetry in linac bunkers

Ongaro et al. studied the spectrum of photoneutrons in the patient plane from an SL20I ELEKTA multileaf accelerator with MC simulation and compared it to experimental results obtained with a neutron spectrometer and passive bubble detectors [74] [75]. The simulation was performed with the MCNP-4B code (the previous version of MCNP5) to model linacs operating at 15 MV and 18 MV. The study follows a very common methodology that consists of validating MC simulations with physical measurements, especially with Bonner sphere neutron spectrometers. *Agosteo et al.* added in sophistication to the analytical neutron flux models by using a set of functions whose spatial behaviour is determined by the angular distributions of the photoneutrons emitted from the shield of the accelerator head and diffused from the walls [76]. Their analytical results were compared to MC results obtained from MCNP.

A study from *Chibani and Ma* used the MCNPX code (a variant of MCNP5) to model in detail 18 MV and 15 MV Siemens and Varian linac heads [77]. Tissue-equivalent phantoms were used to calculate dose distributions from various particles. Results were given in the form of dose equivalent ratio (DER), which is defined as the ratio of the maximum particle dose (in our case neutron) to the maximum photon dose, corrected with the particle's quality factor.

A first observation was that contrary to the behaviour of alpha particles and protons, increasing field size decreases neutron DER. This is probably due to the higher probability of generating neutrons when the jaws or MLCs are closed. It was also found that for all beam energies and field sizes (except for the smallest 1 cm $\times$ 1 cm), three quarters of the total DER is due to neutron contribution. Enlarging the scope of the study, the authors used an NCRP method to assess the risk associated with leakage neutrons [26] and found that for a 70 Gy treatment, risk levels of secondary fatal cancer varied between 1.1 - 2.0 %, depending on the energy and manufacturer of the linac.

In an extensive comparison [72] of photoneutron spectra from various linacs made by Siemens, Varian, and Elekta, *Howell et al.* used Bonner spheres to measure photoneutron production and calculate key associated metrics: ambient equivalent dose, average energy, fluence, and neutron source strength. They observed that neutron spectra shape remained relatively unchanged for different linacs or energies, but as expected, neutron fluence (and consequently ambient equivalent dose) increased with increasing energy. It was also found that Varian linacs had a higher photoneutron production yield than those from other manufacturers.

A 2005 publication by *Howell et al.* [78] had already compared secondary neutron doses associated with conventional 18 MV plans to those from 18 MV IMRT plans delivered with dynamic MLC. It was found that IMRT plans yielded a higher neutron fluence (and by extension dose), proportional to the higher number of monitor units (MU) associated with this type of treatment. Although IMRT is seldom used with 18 MV energies, this study pointed out an additional limitation, namely the higher photoneutron production, associated with high-energy IMRT. Moreover, a Varian Linac with the MLCs was modelled with MCNPX and the photoneutron fluence computed for locations in the head as well as around the linac. These Monte-Carlo results showed good agreement when compared with the clinical measurements.

Using gold foil activation, a study by *Followill et al.* [60] focused on determining the neutron source strength values (Q) for 36 different linac and energy combinations. It was found that changes in total room surface area had minimal impact on neutron fluence in the plane of the patient and that the main contributor to photoneutron dose is the linac head, *i.e.* at the patient's location around the isocenter, direct fluence predominates over room scattered fluence. It was also observed that, as expected, the value of Q increased with increasing photon energy and was between 0.02 - 1.44 ($\times 10^{12}$) neutrons per Gy of photon at the isocenter.

In a study with thermoluminescent devices (TLD), *Barquero et al.* measured thermal neutron fluences, neutron spectra, and neutron dose at 21 different locations inside the treatment room of a radiotherapy 18 MV linac [79]. The spectra were measured with TLDs placed in the middle of Bonner sphere (see section 2.4.3) analogous polyethylene spheres. The MC code MCNP4 was used to calculate neutron Kerma in the TLDs and compute neutron spectra at the experimental points of interest. In the room, spectra could be divided in three sections: a peak at 0.1 MeV, a stable epithermal portion, and a lower thermal energy region. More quantitatively, dose from neutrons (0.5 mSv) was an order of magnitude less than dose from photons (5 mSv), per Gy of photon delivered at the isocenter.

Saeed et al. used the MC particle physics code named Geant4 to model a Varian 2100C linac and study the relation between ambient equivalent dose, energy, and field size [80]. They confirmed that for a given field size, average photoneutron energy scales with linac energy. This work proved that Geant4 could be a valid neutron simulation substitute for the more widespread MCNP code.

MC simulations for photoneutron shielding of linac bunkers

Pena et al. used MC to investigate the impact of various combinations of linacs and room geometries on neutron fluence and spectra [81]. It was shown that there is an 80 % increase in photoneutron fluence at the isocentre when the modelling of a 15 MV linac includes, in addition to the basic components necessary for photon/electron simulations, the high-Z materials (Pb and W) surrounding the linac head. Moreover, analysis of the dependence of neutron fluence on the volume of the treatment room showed an inverse proportionality relation between the two.

In a study closely related to this work, *Carinou et al.* used MCNP4 to simulate neutron and capture gamma ray transport for various maze geometrical parameters, wall composition, and wall surface lining [82]. Calculations were verified with measurements at two linac facilities and good agreement was observed with simulations, which were also compared with results from analytical equations derived by Kersey and McCall (see section 3.2.2). It was found that for maze lengths longer than 8.5 m, analytical and MC results were in line, whereas for shorter mazes the Kersey and McCall methods, respectively overestimated and underestimated neutron dose at door entrance. Furthermore, it was shown that the use of barytes concrete (concrete with barium in the form of $BaSO_4$) instead of ordinary concrete has a significant impact on dose reduction (~20 %) at the entrance. Finally, simulations indicate that the presence of wood and borated polyethylene (BPE) in the maze reduced neutron dose at entrance by 45 % and 65 %, respectively.

In a purely experimental study (no MC), *Wang et al.* studied the neutron dose equivalent rate at the entrance of the bunker for a Varian Clinac 23 EX linac operating at 18 MV [83] and compared it to results from analytical models such as Kersey's or McGinley's. They also investigated the impact that borated polyethylene (BPE) would have on dose reduction in the maze. They found, as expected, that neutron dose was maximum when the gantry head was tilted towards the maze-room passage and when the jaws were closed. It was also found the Kersey method overestimated neutron dose equivalent by about two to four times (calculation to measurement ratio of 2.4 - 3.8) whereas the modified Kersey method (*i.e.* McGinley method) has much more realistic ratios between 0.6 - 0.9.

In a publication pertaining to modern CT-on-rails systems, *Kry et al.* investigated the presence and impact of neutrons on regular electronic malfunctioning following the use of high-energy radiotherapy beams [84]. They first linked the CT scanner's failure rate as a function of 18 MV monitor units (MUs) delivered and examined the impact of covering the linac head with borated polyethylene (BPE). They also used MC simulations to calculate neutron fluence and spectrum in the bore of the CT scanner with and without the presence of BPE layers on the CT scanner and the linac head. It was determined that for a delivery of 200 MUs, using 7.6 cm of BPE on the linac head marginally reduced CT failure rate from 57 % to 29 %, and that fast neutrons were mainly responsible for electronic failures. This study steps out of traditional photoneutron shielding simulations and opens doors to studies on a variety of aspects that will need careful examination in next generation hybrid therapy/imaging systems.

3.3.2 Our approach to bunker modelling and neutron simulations

Since various groups use different MC codes and methods, and since there is no single way to simulate neutron transport in bunkers, it is imperative that we describe the specificities and peculiarities of our approach to radiotherapy photoneutron simulation. It must be noted that we chose this approach because it is also the one used by the CNSC Class II inspection group, with whom we collaborated to obtain our results. Also, all references to the MC code from here on will refer to the MCNP5 code, which we used in this project.

MCNP for bunker modelling and dosimetry

Monte-Carlo is a versatile tool for modelling any component and/or process related to radiation therapy, be it a patient, ventilation, conduits, walls, or anything of interest to the physicist. The main challenge is to know important properties of the object being modelled such as dimension, shape, density, and material composition. Once these building blocks are entered in the code, MCNP can determine appropriate interaction cross-sections from which it samples physical interactions accordingly. Of course, modelling minor details like random daily objects in the bunker is irrelevant and only essential components in terms of architectural structure, such as door, maze, walls, ceiling, and floor will have any meaningful impact on simulation results.

To begin with MCNP, the user starts with an input file where he must enter the composition of materials, then the problem geometry, as well as information on the type of radiation source. Subsequently, the user also defines the type of results and/or information that must be collected and the simulation parameters [85]. Each volume and/or component in the problem is made of a material, the fractional isotopic composition of which can be defined separately giving flexibility to the user to create blends and mixtures of elements.

Each isotope has a given interaction probability with a particle of a given energy and momentum. These interaction tables are provided with MCNP and the user must specify the one to use for a given simulation.

The geometry of the problem is constructed by first defining surfaces and then by creating volumes delimited by these surfaces. There is much flexibility in choosing the radiation source with the possibility to set the type of radiation, the direction of emission, the energy, as well as the exact location or physical distribution of the source.This allows the creation of incident beams in a well defined direction or point isotropic sources, like the one used in this work. Most of our input file information was entered using the MCNP GUI called *Visual Editor*, where the user can graphically draw a geometry and customize the simulation properties with corresponding menus [86]. As its explicit name indicates, *Visual Editor* is an invaluable tool to visually create geometries and input files, that can then be used in the command-line MCNP simulation process. Moreover, *Visual Editor* does have its own embedded MCNP version that, although limited in computational power, is of great help in validating preliminary simulations and obtaining a first approximation of results.

MC results are scored using *tallies*, which store all the statistical information related to the simulation. The end results are essentially clustered in those tallies and provide particle current, fluence, energy deposition, and other metrics that the user is interested in. For our work, the neutron fluence tally determines the portion of neutron fluence (differential) in a given energy bin, averaged over the cell volume $\left(\mathrm{d}\bar{\Phi}_{\mathrm{n}}/\mathrm{dE}_{\mathrm{n}}\right)$. The conversion to ambient equivalent dose is done with conversion coefficients found in report 74 of the ICRP [28]. This was already described in equation 2.11, shown in figure 2–8, and it is the method we used for neutron dose calculations. The value given by equation 2.11 provides the ambient dose equivalent for all the points in the volume of the cell, averaged over that entire volume [85].

Variance reduction techniques

The speed at which a simulation is performed can be drastically increased using variance reduction techniques. The relative error (or uncertainty) R is inversely proportional to the square root of the number of histories N ($\propto 1/\sqrt{\mathrm{N}}$) associated with the simulation. Also, simulation time T is proportional to N and therefore it can be stated that $\mathrm{R} = \mathrm{C}/\sqrt{\mathrm{T}}$ with C being a positive constant. If one wishes to reduce R, one can decrease C and/or increase T. Since increasing T is not practical or realistically feasible, huge efforts have been invested into developing mathematical and/or numerical techniques that would reduce C. The latter can be manipulated by choosing the right tally or using an appropriate sampling method [87]. In other words, since a variance (*i.e.* uncertainty) is associated with every output variable, the precision of simulation results can only be increased if that variance, or roughly speaking the confidence intervals of that variable, are narrowed down and/or reduced. This is the statistical origin of the name associated with the technique.

We used the flux tally at a point (also known as the F5 tally) which inherently makes use of a variance reduction technique known as the *next event estimator*. For every particle from the source and every collision event, the tally deterministically estimates the contribution of the fluence at the point location of the detector. To simplify the description without mathematical formalism, suffice it to say that the F5 tally at a point accounts for all interactions of a particle in the room outside of an exclusion volume defined around that point, *i.e.* particle collisions meters away from the point of interest (the detector) are accounted for but weighted proportionally to the probability that the next event (following that distant collision) will occur at the detector point. That is why the point detector tally (F5) is also referred to with the expression *next event estimator*, because it is a tally of the flux at a point as if the *next event* were a particle trajectory directly to the detector point without further collision [87]. A contribution to the point detector is made at every source or collision event in the room, but the location and conditions in which that collision occurs determines the probability associated with it impacting the detector. For example, if one would measure fluence near the door, interactions occurring in the maze and in the centre of the room will be accounted for, but the former will have a much higher probability to influence the detector dose than the latter.

This is one factor that considerably accelerates simulations and we were able to run 20 million histories ($N = 2 \times 10^7$) in less than 45 minutes. The exclusion volume we defined around the tally point was a 5 cm radius sphere. Nevertheless, the most useful tool for the simulations was the specifically adapted cluster of computers at the McGill Medical Physics department.

Modelling of the radiation source

The Brazilian group of *Facure et al.* used MCNP5 and a practical in-house model to simulate photoneutron fluences inside bunkers [7]. They studied the impact that room design metrics would have on photoneutron fluence, including the role of moderator materials and total room surface area. In order to simplify the simulation they used a method widely accepted in the shielding community: instead of starting with a photon or electron beam that will generate photoneutrons in the various components of the linac head, they used a isotropic point source of neutrons that is surrounded by a 10 cm radius tungsten sphere and a photoneutron energy distribution described in equation 2.8. We have also used this method for our simulations and will describe it in a little more detail. The logic behind this simplified model stems from the complexity of the linac head, the various components of which are often challenging to reproduce in detail or include in time consuming MC simulations. Indeed, the head shielding consists of high atomic number materials such as lead and tungsten, as well as insignificant portions of copper and iron. Because tungsten is the material of the collimator jaws - the composition of which was recommended as a single good substitute for the linac head shielding during MC modelling of energy attenuation [35] - it was decided that the 10 cm sphere emulating the head shielding would also be made of tungsten. Another rational for this choice comes from literature results showing the predominance of tungsten-produced photoneutrons [78]. Also, as mentioned in section 2.3.1, this method has already been successfully tested in other studies from various authors [76][82][30][88] and discussed in detail in report no. 79 of the NCRP [26].

Finally, the tungsten sphere was placed 100 cm above the isocenter, where the linac head (or neutron source) would be if the gantry was not tilted (at an angle of 0 degrees). In our view, this is a reasonable choice in that it represents the average position of the linac without being unrealistic. Indeed, it is intuitively tempting to place the sphere directly at the isocenter since this is probably closer to the geometric average position of the linac head, but this would also be a purely theoretical position since the linac head is never at the isocenter. Also, a previous study of MUHC linacs has shown that the gantry angle at which the linac has delivered the most radiation in the course of a year is 0 degrees [89].

It is now time to conclude the review of shielding techniques and present our results.

Chapter 4
Results and discussion

4.1 Results from Monte-Carlo simulation of photoneutrons

The MCNP5 code was used to study photoneutron distribution in five different linac bunkers. Three of these are existing bunkers at the McGill University Health Centre (MUHC). In this work, they will be referred to by their practical names - Novalis, 21A, and 21B - used in the clinic by MUHC personnel. All three are high energy linacs that routinely operate at 18 MV. Consequently, the photoneutron spectrum used at the centre of the 10 cm radius sphere of tungsten (see section 3.3.2) has a maximum photon energy of 18 MV. More specifically, this implies that equation 2.8 has an E_{max} value of 18, the maximum photon energy (in MeV) generated by the linac. Note that the tungsten sphere is not placed at the isocenter, but 100 cm above it towards the ceiling, where the linac head would be if the gantry angle was set at 0°. The reason behind this is that 0° gantry is the most common treatment position for the linac head [89]. It must nevertheless be noted that photoneutron fluence in the maze is maximum when the gantry is turned 90° towards the inner maze entrance and maze efficiency should be validated at that gantry angles during radiation safety surveys.

Two other hypothetical bunkers designed to operate without a door - and hence with a longer maze and an additional maze bend - were studied. They are named Model 1 and 2 and differ only slightly in dimensions between them. They are considerably larger than the existing MUHC bunkers. The motivation here is to be able to compare results from existing room designs to a new category of doorless bunkers, which are increasing in popularity [90]. Indeed, it is possible that bunkers at the new MUHC facility currently under construction will be doorless. Top-down views of the three existing bunkers along with the two hypothetical ones are displayed in figure 4–1.

In addition to the engineering plans, the drawings in figure 4–1 also present the photoneutron interactions coloured by average energy all over the room, i.e. blue dots represent thermal photoneutrons whereas red dots are associated with photoneutrons in the MeV range. This option is offered by the MCNP associated GUI, Visual Editor [86], which offers the possibility to run an input file with the photoneutron spectrum associated with an 18 MV linac and for a limited number of particle histories (10000 here). The primary use of figure 4–1 is to offer a simple qualitative and visual idea of the photoneutron distribution in regions of interest throughout the bunker, regardless of uncertainty on measurements. The tungsten sphere is almost exclusively red since most photoneutron interactions from the unmoderated spectrum will involve the high-energy neutrons. Indeed, the fraction of fast neutrons in the original spectrum being much larger than in attenuated spectra at different locations in the room, the associated mean neutron energy is also higher and the proportionally scaled colouring shifted to the red.

In addition to top-down views, Visual Editor allows the user to have a clear 3D visualization of the geometries drawn. Figure 4–2 shows 3D views of the five bunkers from different angles. It must be mentioned that the three existing bunkers from the MUHC are very similar in terms of configuration, materials, total surface area, linac operating energy, and length of maze. A similar resemblance exists between hypothetical room models 1 and 2. It is therefore expected that simulation results will follow these similarities, *i.e.* that neutron fluence, spectra, and equivalent dose at various locations in the room will,

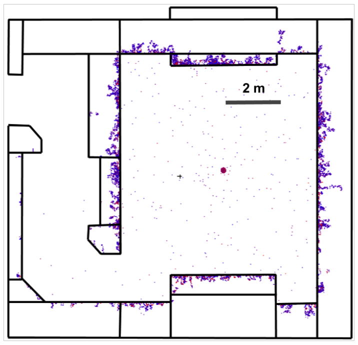

(a) **Model 1**: doorless bunker with 2 bends

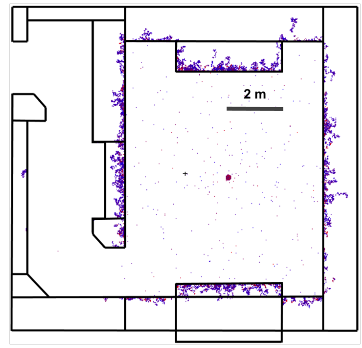

(b) **Model 2**: doorless bunker with 2 bends

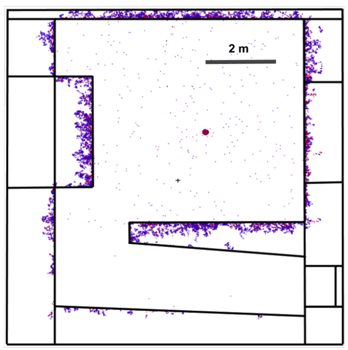

(c) **Bunker 21A** from the MUHC

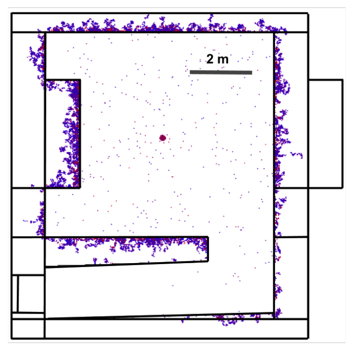

(d) **Novalis** Bunker from the MUHC

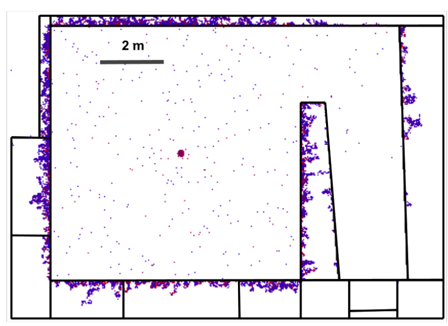

(e) **Bunker 21B** from the MUHC

Figure 4–1: Top-down view of the three currently operational high energy bunkers at the MUHC as well as two hypothetical doorless bunkers. Dots represent neutron interactions (scattering) coloured by neutron energy: blue to red for thermal and fast neutrons, respectively qualitatively and quantitatively, be very close for all vaults belonging to a given category (MUHC or hypothetical models). Indeed, it would even be possible to present simulations for only two bunkers - one from each category - and generalize results to similar room designs. We nevertheless chose to include all five vaults in order to remain thorough in the methodology as well as to emphasize the ability of MC to highlight/detect differences and similarities in simulation design and parameters.

The results in this chapter present the dependency of various photoneutron parameters on key changes in linac bunker design. The goal is to test the flexibility and accuracy of the MCNP5 code for simulations that could eventually be used to optimize photoneutron shielding through improved design. It would have been possible to probe the impact of a very large (indeed countless) number of bunker designs, but for practical reasons only a sample was studied. Photoneutron distribution in the bunker, fluence, dose, and spectral properties were investigated for various combinations of the following bunker features:

1. Presence vs. absence of a door,
2. Presence vs. absence of borated polyethylene lining on the maze walls for bunker models 1 and 2,
3. Presence vs. absence of a bulkhead at the inner maze entrance.

What follows briefly and graphically describes the sensitivity of photoneutron interactions to these design parameters. The location of interest is the maze for all five rooms and most of the tallies (see section 3.3.2) are placed along the maze. Figure 4–3 shows a typical distribution of tallies in bunker model 1. Simulations for the other rooms are also performed with a similar distribution of tallies in their respective mazes. As previously mentioned, the F5 tally spheres had a radius of 5 cm (tallies are not to scale in the figure).

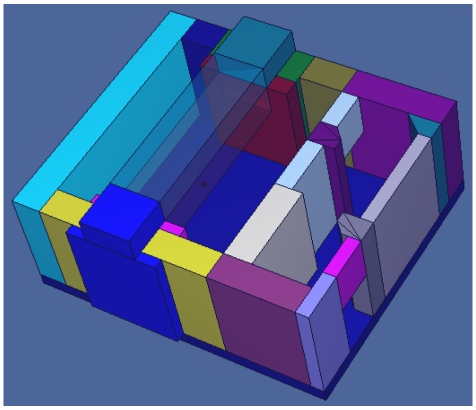

(a) **Model 1**: doorless bunker with 2 bends

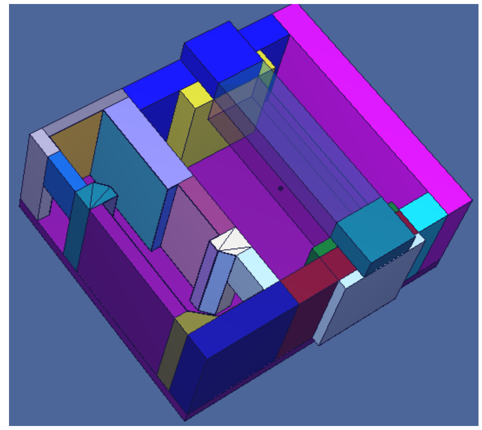

(b) **Model 2**: doorless bunker with 2 bends

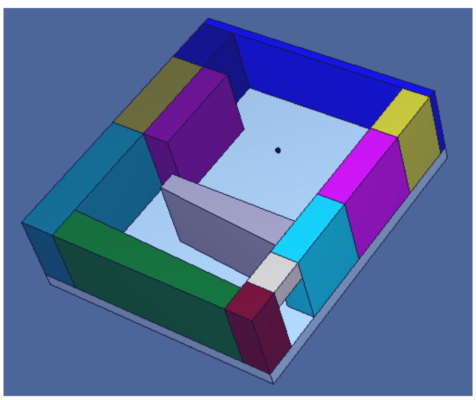

(c) **Bunker 21A** from the MUHC

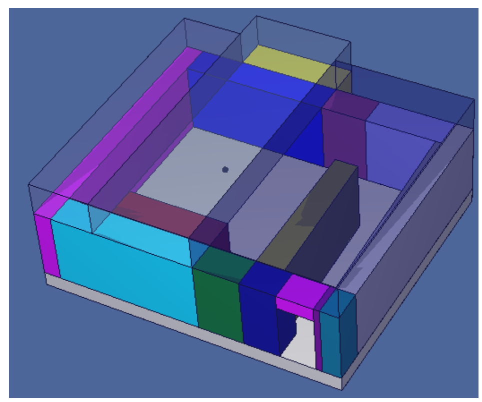

(d) **Novalis** Bunker from the MUHC

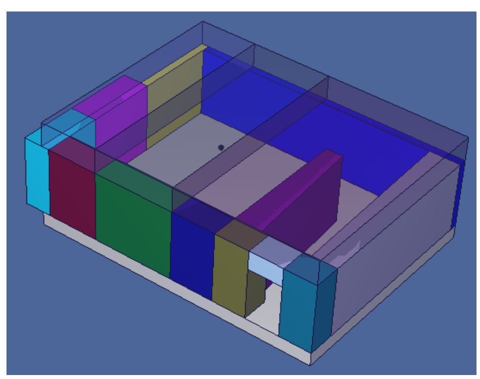

(e) **Bunker 21B** from the MUHC

Figure 4–2: 3D view of all five bunkers. Ceilings have been removed or made transparent for a better view of the room. The small black dot in the middle of the room represents the tungsten sphere

Finally, all simulation results were obtained from 2×10^7 particle histories (N = 20 000 000) reducing uncertainty to under 1.0% on all results. This insignificant value is invisible with uncertainty bars

4.1.1 Impact of the door

The three MUHC bunkers (21A, 21B, and Novalis) have doors whereas bunker models 1 and 2 do not. Studying the impact of the door is therefore only meaningful for the three existing rooms. Moreover, since we already know - through survey measurements and reports - that the three doors are sufficient in preventing photoneutrons from exiting the room, we will disregard photoneutron distribution outside the room and instead focus only on their distribution within the maze. The main objective here is to determine whether the door impacts dose distribution in the maze through an increase of photoneutrons rebounding off the door. The reader might wonder why we would be concerned about the dose caused by neutron rebound from the door. The reason is that a better understanding of neutron physics around the door is essential for their replacement by additional maze bends that are necessary for doorless bunker design. Moreover, rebound on the door is similar to rebound on walls, which is critical to comprehend when adding additional walls and/or surfaces in designing doorless two-bend mazes.

The graphs of dose vs. position in figure 4–4 (left column) show the dose from the last six tallies placed before the door (roughly corresponding to a distance of ∼3 m). There is a slight difference between the closed and open door configurations only next to the door indicating a higher dose for the latter in all three bunkers. Spectra associated with tally 15, the closest to the door (distance of 50 cm), also show small differences between both configurations. The open door is associated with a slightly - almost insignificantly - higher dose contribution from thermal neutrons, represented by the left peak, whereas the fast

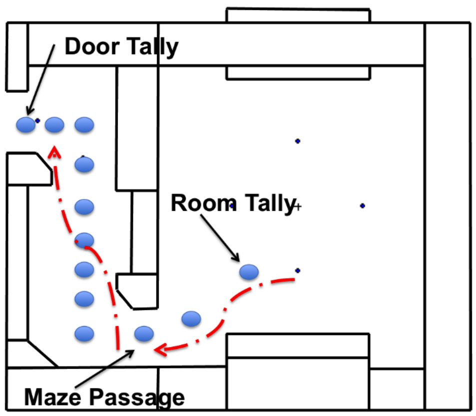

(a) Tally positioning vs. typical photoneutron trajectory along the maze

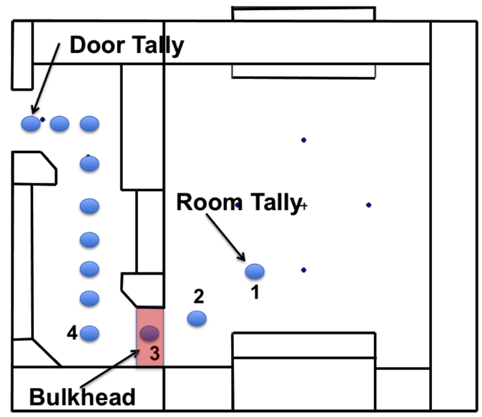

(b) Tally positioning and position of the maze passage **bulkhead**

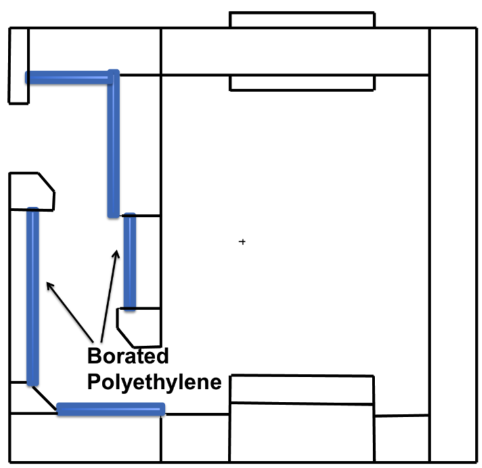

(c) Position of **borated polyethylene** (BPE) layers along the maze walls

Figure 4–3: Positioning of tallies in bunker model 1 and two bunker design features: borated polyethylene in the maze and presence of bulkhead in maze passage neutron/epithermal peak remains unchanged. This implies that the number of thermal neutrons (*i.e.* thermal neutron fluence) is slightly higher near the maze entrance when the door is open. Indeed, it can be seen in figure 4–5 that the fluence spectrum has a slightly higher number of neutrons associated with the thermal energy peak for all three rooms. This is counterintuitive, since we initially expected that neutrons rebounding off the door would increase dose in its vicinity. The practical impact of this observation is limited since the door will be closed in all cases, but it helps us understand (and eventually manipulate) the dynamics of thermal and fast neutrons in the vicinity of the bunker entrance, with or without a door.

Figure 4–6 shows the quantitative impact of opening the door on dose and fluence values at the entrance of the bunker. This confirms the tendency seen in figure 4–4, where the absence of a door results in a slight dose increase at the end of the maze.

4.1.2 Impact of borated polyethylene

This section will look at the influence of borated polyethylene (BPE - 5% boron by weight) linings on the walls of the maze (layer thickness of 2.54 cm). As explained in section 2.1.5, BPE preferentially absorbs thermal neutrons, which are dominant in the maze. It is therefore a useful material to *capture and/or stop* already thermalized neutrons. Although BPE neutron capture is followed by emission of γ rays, this is not problematic since it is much easier to shield for photons than for neutrons.

Fluence and dose distribution are examined in the maze of all five bunkers and results are summarized in figures 4–7 and 4–8. Figure 4–7 clearly shows a decrease in the number of neutrons as measurement position progresses from inner maze (passage from room to maze) to entrance and/or door of the bunker. The first tally is placed in the room right before the inner maze and the last

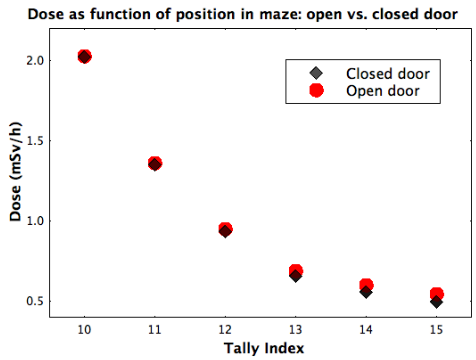

(a) 21A: Dose vs. position

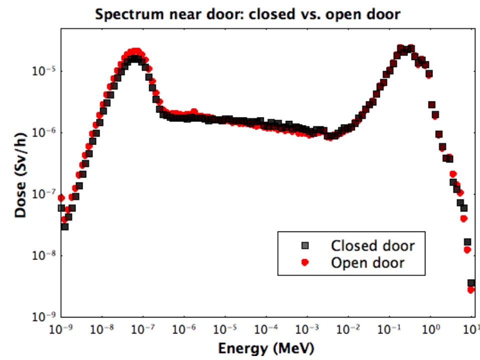

(b) 21A: spectrum near door

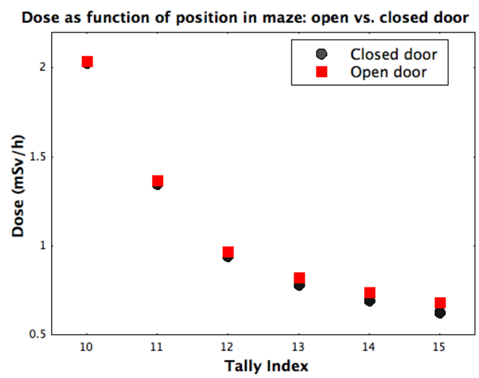

(c) 21B: Dose vs. position

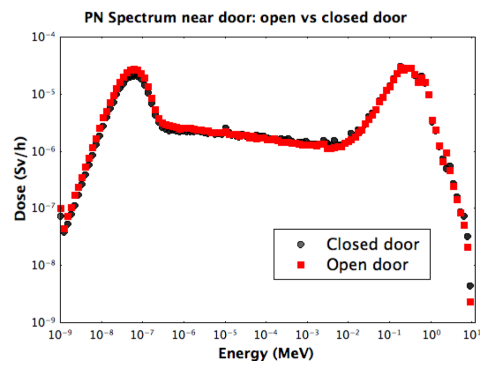

(d) 21B: spectrum near door

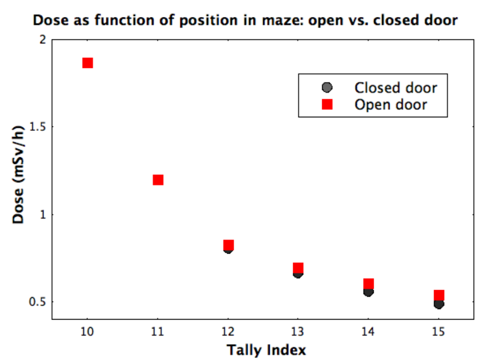

(e) Novalis: Dose vs. position

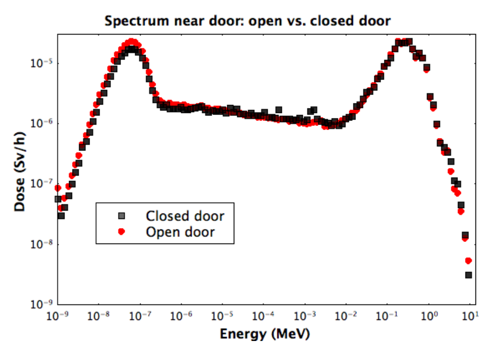

(f) Novalis: spectrum near door

Figure 4–4: Open vs. closed door for 3 existing bunkers at the MUHC. Dose as a function of tally position near the door (left column) and dose spectrum right next to the door within the maze. Note the slightly (but consistently) higher dose for open door configurations in all rooms.

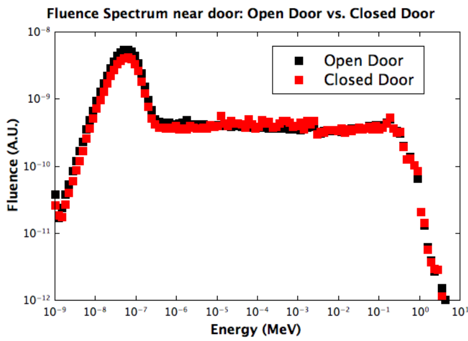

(a) 21A: fluence spectrum near door

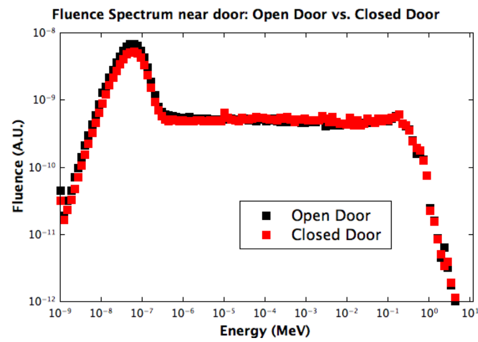

(b) 21B: fluence spectrum near door

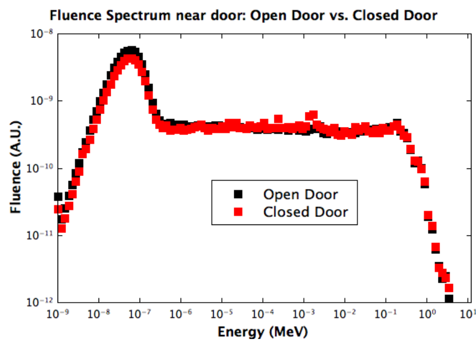

(c) Novalis: fluence spectrum near door

Figure 4–5: Spectrum right next to entrance in the maze for three rooms. The open door configuration results in a minor fluence increase

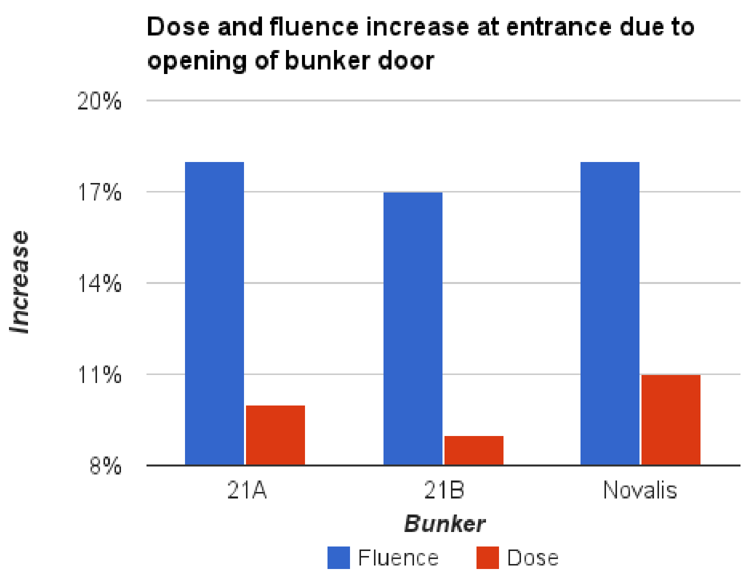

Figure 4–6: Attenuation of fluence and dose at the entrance of the bunker: impact of opening the door

Table 4–1: Dose at bunker entrance with and without BPE lining on the maze walls. Also shown is the percent reduction in dose and fluence at the entrance introduced by the use of BPE

Bunker	Dose - no BPE	Dose - with BPE	Dose variation - BPE vs. no BPE	Fluence variation - BPE vs. no BPE
		(mSv/h)		
21A	0.493	0.127	*-74 %*	*-80 %*
21B	0.626	0.25	*-60 %*	*-68 %*
Novalis	0.491	0.126	*-74 %*	*-80 %*
Model 1	0.103	0.020	*-80 %*	*-88 %*
Model 2	0.0820	0.0074	*-91 %*	*-92 %*

is right next to the door for bunkers 21A, 21B, and Novalis and right before the entrance for room Models 1 and 2 (doorless bunkers).

As expected, figure 4–7 confirms that BPE significantly attenuates neutron fluence, with the difference being amplified as neutrons progress in the maze. The reason is that the surface of BPE exposed to neutrons becomes proportionally higher as they approach the entrance/door. Most neutrons will therefore have interacted with the BPE by the time they reach the door/entrance. BPE lining of the maze walls is thus a very useful tool for neutron shielding and especially so for doorless bunkers.

On the other hand, figure 4–8 shows the overall reduction of dose at a room entrance due to BPE lining of the maze. A significant feature is that the proportion of fast to thermal neutrons is higher with the presence of BPE. The explanation lies with the fact that a lower number of thermal neutrons make it to the door/entrance because they have a high probability of interaction with BPE. Consequently, thermal neutron contribution to overall dose is proportionally lower when using BPE.

Table 4–1 summarizes the quantitative impact of BPE on neutron fluence and dose near the room entrance for the five bunkers.

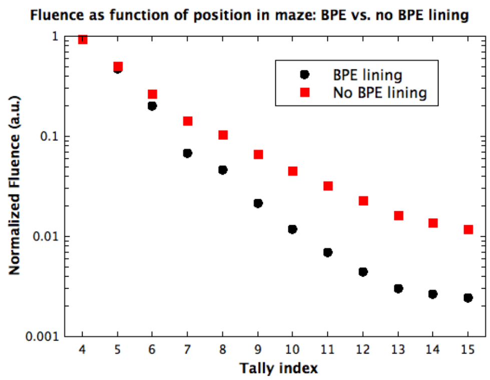

(a) 21A: closed door

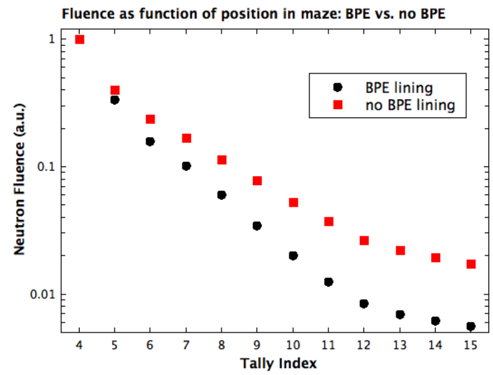

(b) 21B: closed door

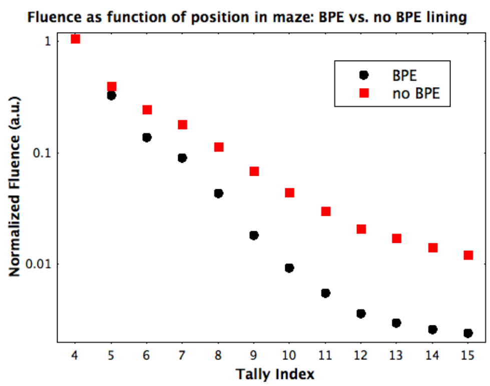

(c) Novalis: closed door

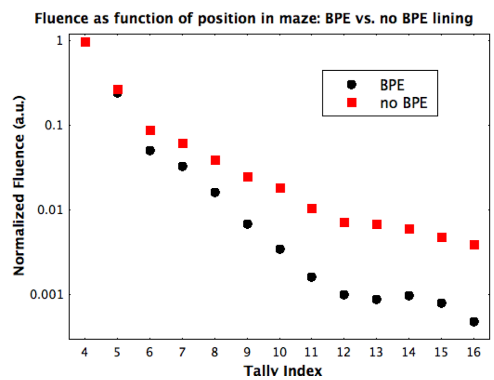

(d) Model 1

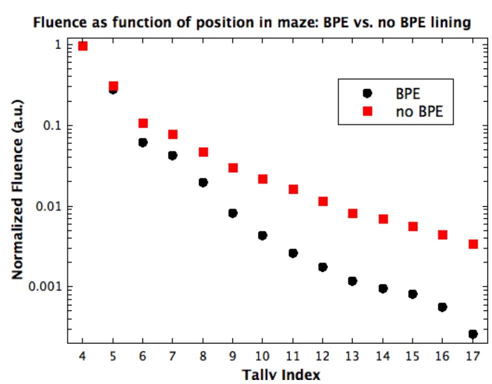

(e) Model 2

Figure 4–7: Impact of borated polyethylene (BPE) on number of neutrons in the maze for 5 bunkers. Displayed is the fluence as a function of tally position in maze. Note the significant reduction in neutrons associated with the presence of BPE.

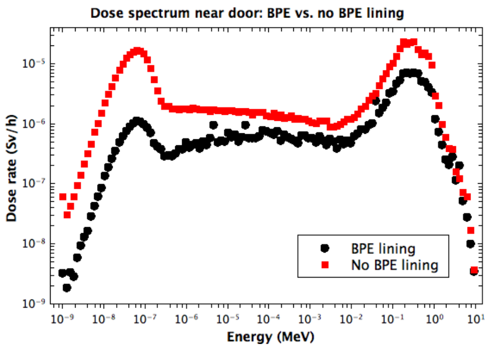

(a) 21A: closed door

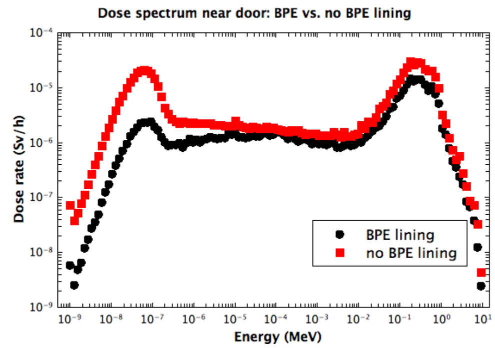

(b) 21B: closed door

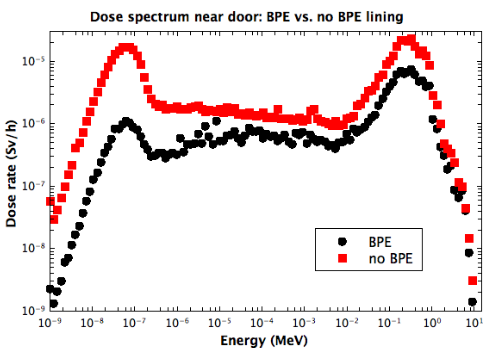

(c) Novalis: closed door

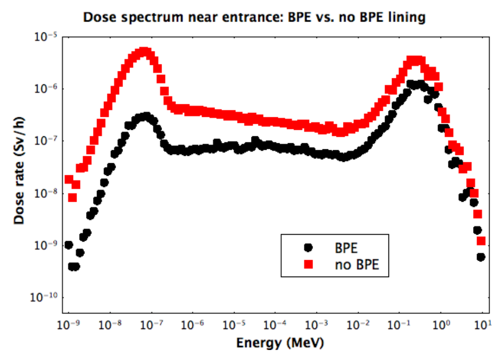

(d) Model 1

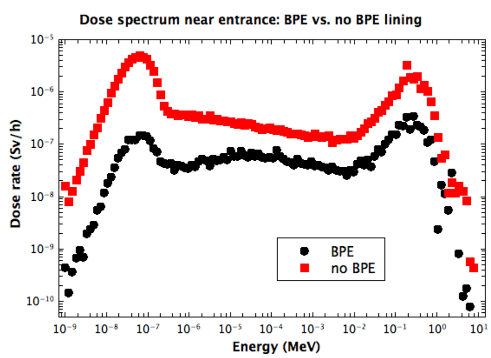

(e) Model 2

Figure 4–8: Impact of borated polyethylene (BPE) on neutron energy distribution near the entrance/door of 5 bunkers. Displayed is the dose spectrum near the door with and without BPE lining on the maze walls. Note a ∼10x thermal neutron dose reduction associated with the presence of BPE.

Similarly, figure 4–9 shows the factor by which fluence and dose are reduced by the maze, with and without the use of BPE. The impact of BPE is clearly significant on dose reduction, making it a material of choice for photoneutron shielding.

4.1.3 Impact of maze

As an attempt to focus on the role of the maze in the bigger picture of radiation shielding, we will now look at its general impact on fluence and dose. In particular, we are interested in how the maze modifies these two key metrics in the specific case of neutrons, and what are the quantitative and qualitative benefits of the maze to neutron shielding. The simplest way to evaluate the net impact of the maze would be to score dose (or fluence) at the bunker entrance with and without the maze wall present, but this is not our goal and it has already been extensively studied since the 1970s and 1980s [54] [26]. Since we are not aiming to investigate the rationale of using a maze, we will instead put the emphasis on quantifying the differences in fluence (or dose) at two different points along the maze (maze entrance and bunker entrance). This is indeed much more relevant to our general objective of understanding and optimizing maze design.

Figures 4–10 and 4–11 show the fluence and dose spectra inside the room and near the entrance/door of all five bunkers. As neutrons progress from inside the room to the door, two major changes occur: (1) a reduction of the overall number of neutrons and more specifically (2) a preferential reduction of the high-energy (fast) neutrons. The result is an overall decrease in dose rate near the door/entrance. A closer observation of the spectra shows that the fast neutron fluence peak disappears as neutrons reach the entrance. This is consistent with the model of neutron thermalization through elastic interactions explained in chapter 2 and is the reason for the use of the maze. Looking at the

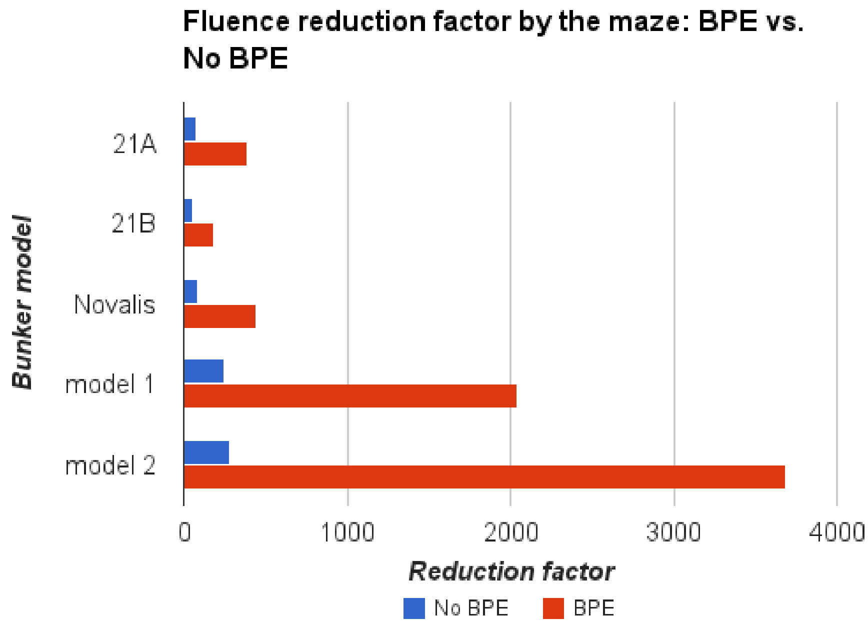

(a) Fluence reduction factor by maze: BPE vs. No BPE

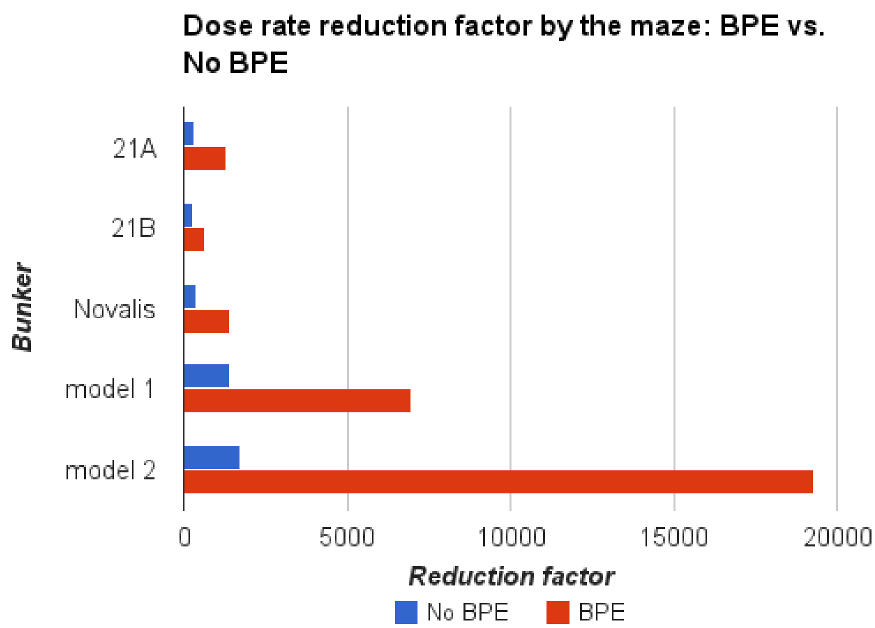

(b) Dose reduction factor by maze: BPE vs. No BPE

Figure 4–9: Attenuation of fluence and dose by the maze, with and without BPE lining on maze walls. Notice the significant dose and fluence reduction introduced by the use of BPE

Table 4–2: Dose rate in room and at door computed with MC and analytical models. Percent values in parentheses show the deviation of analytical results from Monte-Carlo simulations

Bunker	**Monte-Carlo: In Room**	**Monte-Carlo: Room Entrance**	**McGinley method (2002)**	**Kearsey method (1979)**
		(mSv/h)		
21A	162	0.492	0.202 *(-59 %)*	0.778 *(58 %)*
21B	158	0.626	0.284 *(-55 %)*	1.325 *(112 %)*
Novalis	177	0.491	0.238 *(-52 %)*	1.598 *(225 %)*
Model 1	142	0.103	0.058 *(-44 %)*	0.032 *(-69 %)*
Model 2	142	0.082	0.047 *(-43 %)*	0.025 *(-70 %)*

dose spectrum, it is clear that in the room, the major contributor to dose are the fast neutrons since the associated peak is two to three times higher than the thermal neutron peak. At the entrance of the bunker, dose contribution is almost equally shared between thermal and fast neutrons, as both peaks are of a similar height. Therefore, aside from overall fluence reduction, the most significant change in neutron spectra is the reduction of the ratio of fast to thermal neutrons from inside the room to the end of the maze. For example, figure 4–11 (e) qualitatively shows that $\frac{\mathrm{B}}{\mathrm{A}} \simeq 3\left(\frac{\mathrm{D}}{\mathrm{C}}\right)$.

The decrease in the number of fast neutrons and, consequently, the corresponding dose is caused entirely by the maze, hence its indispensability to high energy linac shielding. Note that the surface area under the dose spectrum provides the total dose associated with that particular tally. Table 4–2 presents the dose values (in mSv/h) associated with figure 4–11 as well as results from the analytical models of Kearsey and McGinley presented in section 3.2.2. Since dose from analytical models is given in Sieverts per Gray (Sv/Gy) of photon dose delivered at the isocenter, it is necessary to convert it to units given by the MC simulations (Sv/h). MUHC has characterized its linacs to operate at an average dose rate of 600 MU/min and since 100 MU corresponds to a dose of 1 Gy to the isocenter, 6 Gy are delivered to the isocenter every minute, or equivalently (6 Gy/min)·(60 min/h)=360 Gy/h. This dose rate is then multiplied by the result from the analytical models to yield units of Sv/h, which corresponds to the units of the MC results.

A reduction of ~3-4 orders of magnitude is seen in neutron dose when moving from the room to the bunker entrance. It is also clear that the two doorless bunkers are more effective in reducing dose than the three existing bunkers. This is mostly due to a longer maze as well as the additional bend (or leg) at the end of the maze i.e. the more space neutrons have for interaction the more thermalized they will be, and since fluence-to-ambient-dose-equivalent conversion factors are directly proportional to neutron energy (see figure 2–8 in section 2.4), the equivalent dose from thermal neutrons is smaller. Without the maze, dose reductions of many orders of magnitude would not be possible. As in table 4–2, a comparison of MC results with analytical models reveals significant discrepancies. As values in parentheses indicate, with respect to the MC method, the McGinley method consistently underestimates dose at room entrance, whereas the older Kearsey method overestimates dose except for doorless bunkers. Also, the former is generally slightly more accurate than the latter in matching MC results. This proves that although simple to use analytical models give results that are significantly different from those obtained from MC.

4.1.4 Impact of the bulkhead

Finally, we will examine the impact of a structural change in the geometry of the room on the dose rate at the entrance of the bunker. It was decided to study the effect of adding a bulkhead in the maze passage (as previously shown in figure 4–3). Figure 4–12 shows the dose spectrum at the entrance of room Model 1 with and without a concrete bulkhead placed at the inner maze

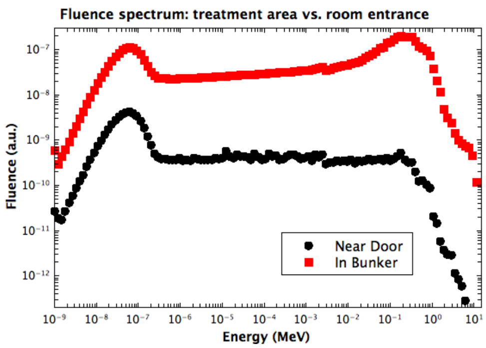

(a) 21A: closed door

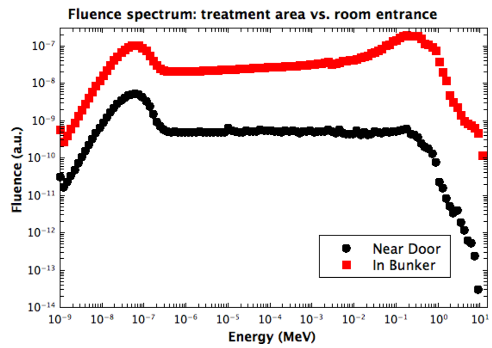

(b) 21B: closed door

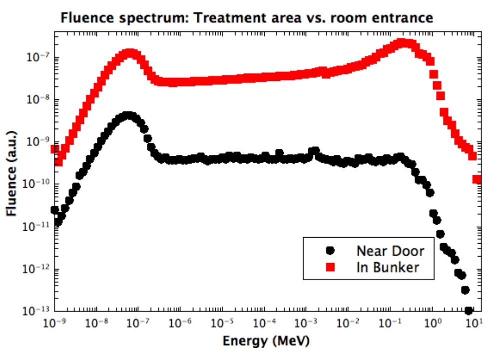

(c) Novalis: closed door

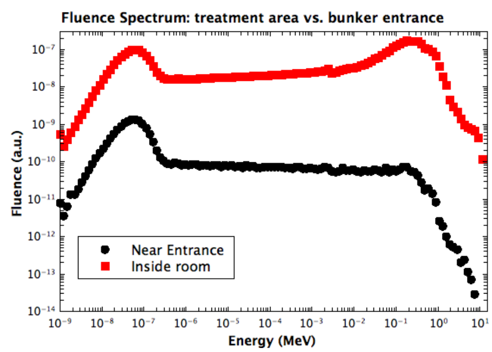

(d) Model 1

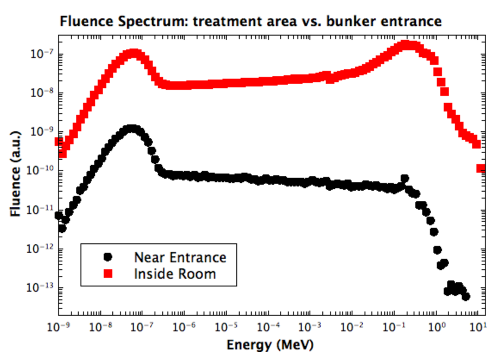

(e) Model 2

Figure 4–10: Fluence spectrum in the room and near the door or entrance of bunker. Note the disappearance at the end of the maze of the second peak representing high energy (fast) neutrons.

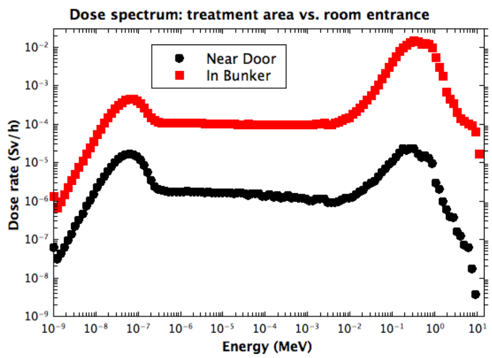

(a) 21A: closed door

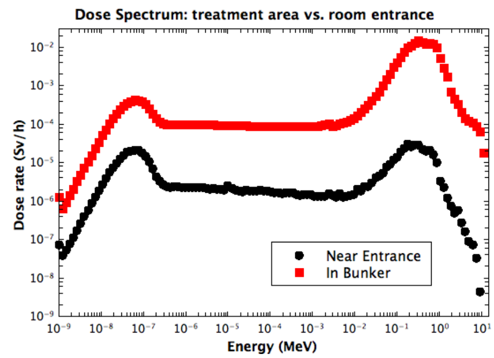

(b) 21B: closed door

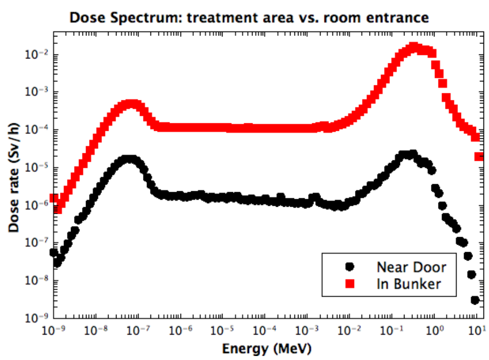

(c) Novalis: closed door

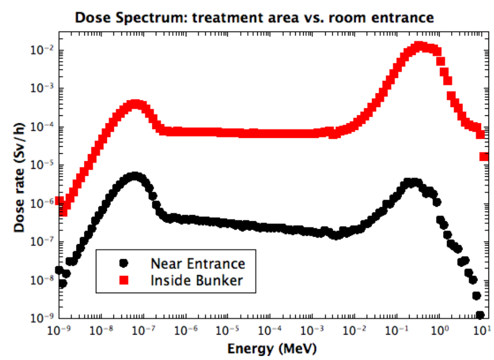

(d) Model 1

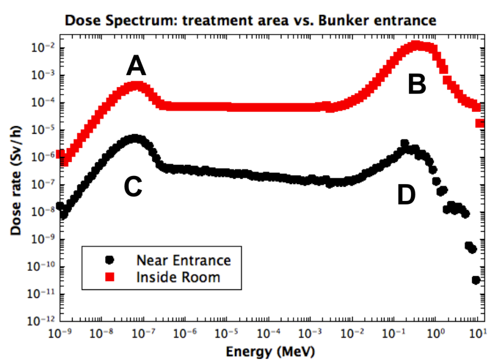

(e) Model 2

Figure 4–11: Dose spectrum in the room and near the door or entrance of bunker. Note the much smaller contribution to overall dose from the fast neutrons - as indicated by the smaller ratio of fast to thermal neutron peaks - near the end of the maze, *i.e.* $\frac{B}{A} > \frac{D}{C}$.

passage as well as a three dimensional view of the bunker and the highlighted bulkhead. Overall dose rate (surface under the dose spectrum - Sv/h) at the room entrance with and without bulkhead is 0.101 mSv and 0.166 mSv, respectively (a 39 % decrease introduced by the bulkhead).

An important feature here is that the dose is reduced homogeneously, with very little distinction between thermal and fast neutrons. The reason is that the bulkhead does not inherently favour neutron thermalization as would other design features such as the length of the maze (section 4.1.3) or the presence of BPE on maze walls (section 4.1.2). A bulkhead simply reduces neutron fluence at the entrance of the maze without altering the proportion or ratio of fast to thermal neutron dose contribution. It is a useful tool, since a 39 % dose reduction is a significant number, especially if used in conjunction with other shielding optimization elements such as the addition of borated polyethylene.

4.2 Physical measurement attempts

Although the bulk of this Master's project pertained to Monte-Carlo simulations for bunker shielding, physical measurements were also performed using two instruments: a ^{3}He neutron spectrometer and bubble detectors (see section 2). The aim was to explore parallel paths that would serve as benchmarks to confirm the accuracy of our MC simulations.

This experimental attempt was partially successful with bubble detectors as our neutron spectrometer was incompatible with the linac's pulsed mode of operation and in need of more thorough characterization. Bubble detectors were tested to simply confirm the overall tendencies expected and observed with MC simulations. We did not compare measured dose values with MC results in the maze because bubble detectors yield statistically significant numbers

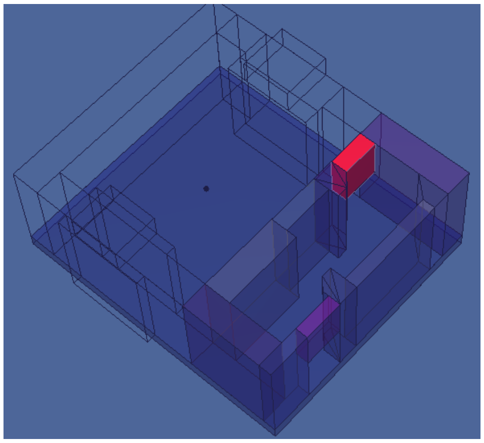

(a) 3D representation of a bulkhead

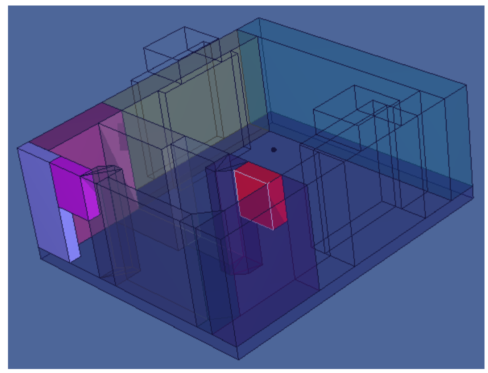

(b) 3D representation of a bulkhead

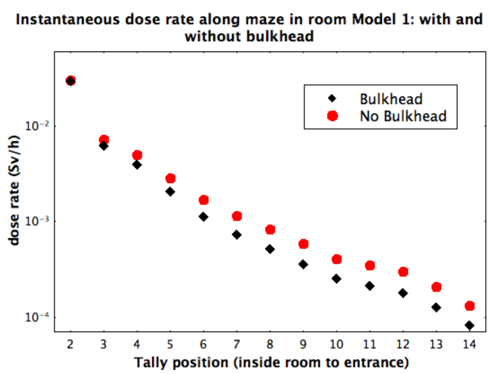

(c) Dose as function of position

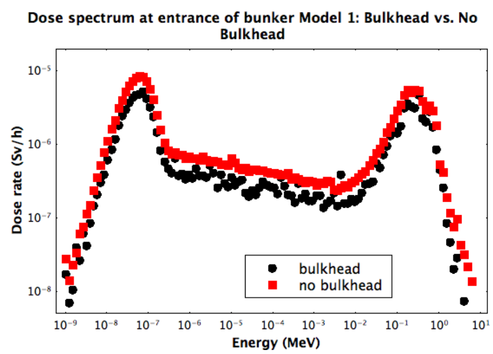

(d) Dose spectrum at entrance

Figure 4–12: Impact of Bulkhead in room Model 1: (C) Dose as function of position within the maze and (D) dose spectrum at room entrance. Notice the overall and homogenous dose reduction. (A and B) 3D views of the bunker and the bulkhead in read, obtained with VisualEditor. The black dot in the middle of the room is the tungsten sphere only after a minimum number of bubbles (~ 80) have been created. The challenge is that large numbers of bubbles are difficult to count without a special bubble counter that we did not have access to.

Despite these obstacles and our limited success in surmounting them, we consider the experimental portion of our project very fruitful in understanding and developing skills in perhaps this most difficult aspect of neutron physics: the detection of neutrons followed by quantification of the associated dose and spectral properties.

4.2.1 The ^{3}He neutron spectrometer

As presented in section 2.4.2, the ^{3}He neutron spectrometer is a popular and useful tool for measuring the neutron energy distribution. We used a Cutler-Shalev-type ^{3}He Seforad neutron spectrometer coupled to a charge sensitive preamplifier (FNS-1, Seforad-Applied Radiation Ltd, Emek Hayarden, Israel). Calibration of the detector was attempted at the CNSC laboratory in Ottawa using two ^{241}AmBe neutron sources and a ^{137}Cs gamma source. The spectrometer was exposed to neutrons in two different configurations: in a large room where scattering was minimized, and on top of a narrow well with a neutron source placed at its bottom. In the latter setup, neutrons were collimated via the well shaft onto the sensitive volume of the detector. Figure 4–13 presents both of our calibration setups at the CNSC with some of the physicists involved. Calibration of the spectrometer was problematic due to difficulties in fully accounting for neutron scatter in the well and our inability to decouple the photon and neutron components of the spectrum.

As for measurements, the ^{3}He spectrometer response at different locations within the bunker showed saturation due to the high flux of neutrons caused by the pulsed nature of the linac beam. We found that the intense photon and neutron pulses overwhelm our detector through pulse pile-up, making it

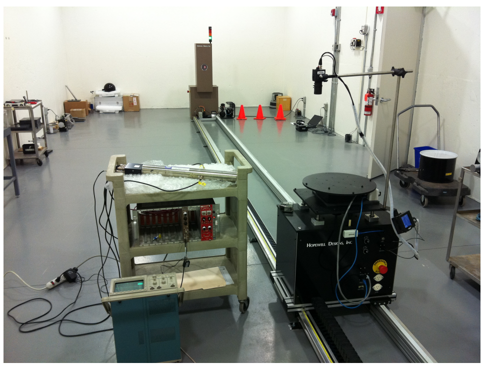

(a) Large room: spectrometer on cart and calibration source platform placed on rails

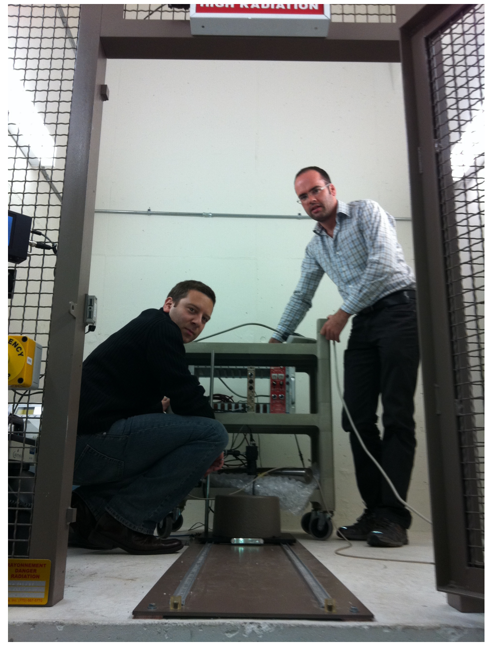

(b) Physicists on top of calibration well - with my supervisor John Kildea (right)

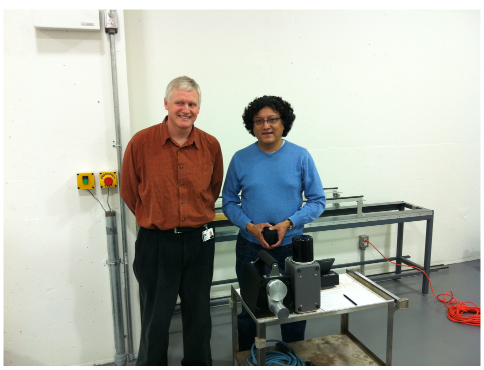

(c) Collaboration of CNSC and McGill experts - Michael Evans from McGill (left) and Angel Licea from the CNSC

(d) Physicists working in the large room

Figure 4–13: Calibration of the spectrometer at the CNSC: (A) the large calibration room, (B) the room with the well, (C) experts involved in the project and (D) physicist colleagues working in the large room.

impossible to distribute fluence into regular energy bins in order to obtain a spectrum. Figure 4–14 C shows a simplified diagram of the pulse pile-up problem we faced. Without delving into details, suffice it to say that the height/amplitude of the pulse (vertical axis) is proportional to the energy of the neutron that caused it. In the case of a continuously emitting neutron source, the neutron flux is sufficiently low in intensity (number of neutrons per unit time) for neutron detection pulses to form in a distinct and discernible manner (from the perspective of the pules-height analyzer). This enables the formation of a clear distribution of pulses on the time axis. From there on, the possibility to count and bin pulses according to their amplitudes (energies) can yield histograms of the number of neutrons with respect to energy values, *i.e.* a spectrum. This fluence spectrum is easily transformed into a dose spectrum by weighing it with the fluence-to-dose-equivalent conversion factors relation (section 2.4). We had initially hoped that our setup/equipment would follow this simple procedure only to realize that the linac operates in pulsed mode, i.e. a very high neutron and photon flux saturates the detector in a short period of time (6 μs) making the distinction of pulse heights impossible. We nevertheless present some pictures and diagrams (figures 4–13 and 4–14) that reflect the experimental tests completed and the challenges faced.

4.2.2 Bubble detectors

Neutron equivalent dose was also measured using bubble detectors (BTI, Chalk River, ON). Bubble detector technology will not be detailed here but suffice it to mention that it is based on the concept of stored mechanical energy in the form of superheated liquid dispersed throughout a polymeric medium [91]. Neutrons striking this medium produce small visible bubbles which appear instantly in the dosimeter and can be subsequently counted. The bubbles can be re-compressed - and the detector reused - by screwing the

(a) Spectrometer in maze

(b) Spectrometer in room: notice that the linac has been tilted to be as close as possible to the spectrometer

(c) Screenshot from our oscilloscope when the spectrometer is placed at the junction of the maze and the room and exposed to 6 MV photon beam

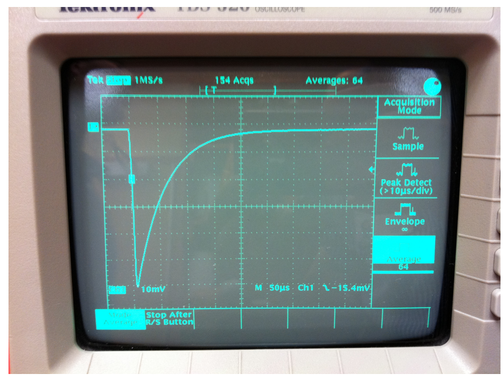

(d) Screenshot from our oscilloscope when the spectrometer is placed in the maze close to the door and exposed to 6 MV photon beam.

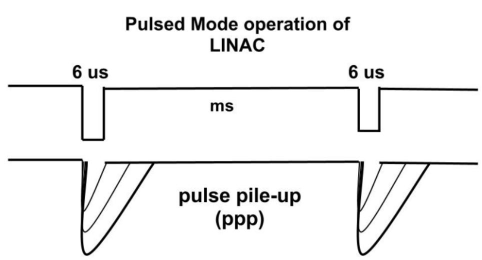

(e) pulse pile-up of spectrometer: linac pulses on top and the resulting pulse saturation at the bottom

Figure 4–14: Measurements with the spectrometer in bunker 21A of the MUHC: spectrometer, amplifier, and pulse height analyzer placed on a mobile cart positioned (A) in the maze and (B) in the room next to the linac. (C) and (D) The pulse pile-up situation as seen on an oscilloscope and on a diagram (E).

cap assembly back on the dosimeter. By varying the formulation/proportion of the superheated liquid and the polymeric medium, the radiation detection properties of the bubble detector can be varied to meet different requirements. This flexibility in design has thus allowed the production of a range of bubble detectors over the years.

We used bubble detectors because they are passive devices, which makes them incomparably simpler to manipulate than active instruments such as spectrometers, as well as conceptually easy to understand: bubbles are simply formed following exposure of the detector to neutrons. The number of bubbles is directly proportional to the measured equivalent neutron dose at the location of the bubble detector. A bubble-per-Sievert (b/Sv) coefficient is associated with each bubble detector and characterizes that specific detector's sensitivity. A thorough review on bubble detectors was written by Ing, Noulty, and McLean in 1997 [91], and numerous publications report their use in the context of photoneutron dose measurements in linac bunkers [92].

We first used six detectors with different sensitivities at various locations within the bunker and the maze and counted the bubbles using in-house software (courtesy of Dr. DeBlois). After discussion with CNSC experts, it was determined that at the very least 80 bubbles (and ideally much more) are necessary to have statistically significant results, a number that is not trivial to count manually. The main obstacle is determining what exactly constitutes a bubble and this uncertainty introduces inherent subjectivity in counting methodology. In order to account for the 3D distribution of bubbles and avoid unwanted visual effects stemming from angular dependency during counting, we acquired pictures of our bubble detectors at three different angles. This approach is meant to increase statistical relevance and credibility by introducing some averaging as well as by attenuating the impact of visual errors

(a) general view of BTI bubble detectors

(b) Bubble detector picture after exposition to neutrons

Figure 4–15: (A) general view of BTI bubble detectors and (B) our picture of a bubble detector after exposure to neutrons in the bunker

during the counting stage. Thus, all following results are averages of three views and based on a minimum number of 80 bubbles. Figure 4–15 shows a general view of bubble detectors as well as a typical picture of bubbles formed after exposure, and which are subsequently manually counted.

Using the bubble detectors we were able to examine neutron equivalent dose within the photon beam, around the linac and at the opening of the maze. Within the maze and near the door, however, regular exposure times (100-200 MU) yielded low numbers (< 20) of bubbles forcing us to increase MU numbers to the hundreds and thousands, in order to obtain statistically relevant numbers of bubbles. Figure 4–16 presents histograms of various measurements made in the room and in the maze, the overall objective being to validate the bubble detector functionality, sensitivity, and to confirm, qualitatively and quantitatively, expected trends such as linearity of measured dose with number of delivered MUs. The energy used was 18 MV in order to maximize photoneutron production. Six different sensitivity bubble detectors were used: (1) 0.075 b/μSv, (2) 0.083 b/μSv, (3) 0.085 b/μSv, (4) 2.2 b/μSv, (5) 2.3 b/μSv, (6) 2.4 b/μSv. For practical reasons, the detectors were identified with the label number instead of their sensitivity.

Bubble detector results indicate inaccuracies. For example, histograms from figure 4–16 (a) and (b) should yield equal values of equivalent dose for a given number of MUs, i.e. all three detectors are supposed to measure the same dose, albeit with varying numbers of formed bubbles, which is clearly not the case. This can be due to bubble counting uncertainty since we counted from 3 different viewing angles, hence the term 'average dose'. In figure 4–16 (c), the relative sensitivity of the six detectors to dose variations, displayed by a variation from 100 MU to 125 MU shows a proportional increase in detected equivalent dose. The histogram of figure 4–16 (d) shows that the detectors' response follows the trend of the increasing number of MU, although with a considerable lack of accuracy. Indeed, aside from a non-proportional increase, the reader can note the non-linearity of detector 2 (0.083 b/μSv) in response to a change in exposure from 70 to 90 MU. Finally, the neutron yield - measured as the detected neutron equivalent dose per gray of photon dose delivered to the isocenter - is shown in the histogram of figure 4–16 (e). This ratio is, as expected, stable and helps validate the qualitative functionality (but not the precision or accuracy) of our bubble detectors.

Only after preliminary measurements were completed did we realize that BTI (Chalk River, ON), the company that manufactures the bubble detectors, has a product specifically suited for thermal neutron detection (labeled BDT for Bubble Detector Thermal). Because the area of interest in this work is the maze, we decided to compare the thermal bubble detector with the standard bubble detector we previously used (also known as the Personal Neutron Dosimeter - PND). Sensitivities were intentionally chosen to be as high as possible and were manufactured at values of 2.9 b/μSv and 3.1 b/μSv for the

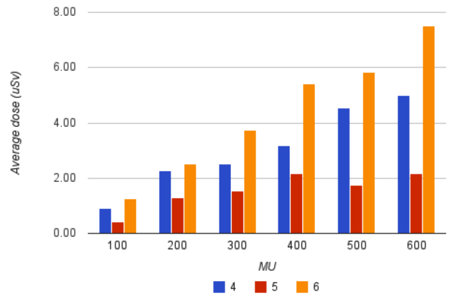

(a) Equivalent dose (μSv) vs. output (MU) in maze for 3 **most sensitive** detectors

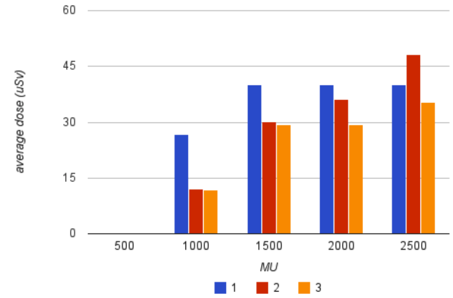

(b) Equivalent dose (μSv) vs. output (MU) in maze for 3 **least sensitive** detectors: notice the higher number of MUs and no detection below 500 MU

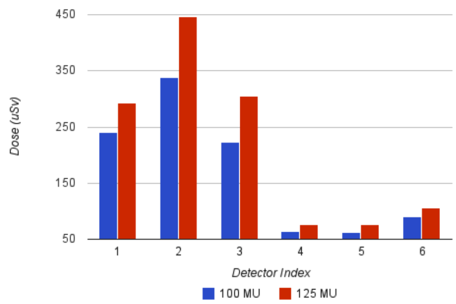

(c) Increase in detected equivalent dose from 100 MU to 125 MU. In order to account for sensitivity differences, detectors 4, 5, 6 were placed in the maze whereas detectors 1, 2, 3 were placed in the room

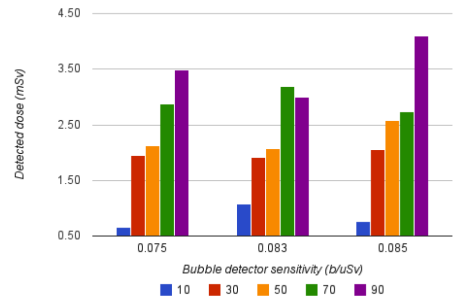

(d) Response of 3 least sensitive detectors to increasing MU values (10-90). Detectors are placed in the beam.

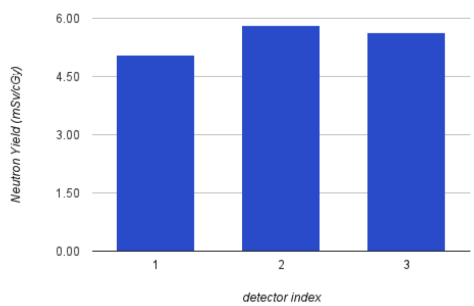

(e) Average neutron yield for 3 least sensitive bubble detectors placed in the beam.

Figure 4–16: Various measurements with 6 different bubble detectors ((1) 0.075 b/μSv, (2) 0.083 b/μSv, (3) 0.085 b/μSv, (4) 2.2 b/μSv, (5) 2.3 b/μSv, (6) 2.4 b/μSv). The objective was to explore and understand bubble detector functionality. Average values refer to 3 different readings of the bubble detectors (corresponding to 3 different angles)

PND and the BDT, respectively. Measurements were performed in the maze of bunker 21B, where we were certain to have a significant portion of thermal neutrons and would therefore be able to test the potential advantage of thermal bubble detectors over standard ones. Figure 4–17 shows these differences for two positions of bubble detectors, the inner maze (or beginning of the maze) and the room entrance (or end of maze).

As expected, both bubble detectors clearly reflect the decrease of equivalent dose values dropping by factors of 9.7 and 6.3 for the PND and the BDT, respectively. More significantly, whereas PNDs detected more dose than BDTs at the beginning of the maze, the opposite is true near the door. Indeed, the histograms show that PNDs detect 20% more dose than BDTs when placed in the inner maze, whereas the latter detect 23% more dose than the former near the door. This is coherent with the proportion of fast and thermal neutrons at different points in the maze, the former dominating near the room and the latter near the door. PNDs, which are more sensitive than BDTs to higher energy neutrons, will measure a higher dose value associated with a large portion of fast neutrons at the beginning of the maze. Similarly, BDTs being more sensitive to thermal neutrons, which dominate in the vicinity of the door, will detect more thermal neutron associated dose near the door. Consequently, it appears reasonable to use BDTs for neutron dose measurements near the door because of the dominance of thermal neutrons in that specific section of the maze.

Finally, it is worth mentioning that BDT measurements need to be apprehended within their intrinsic uncertainties as well as with the understanding that these detectors are clearly not insensitive to epi-thermal and fast neutrons, but have simply had their sensitivity to thermal neutrons enhanced relative to PNDs.

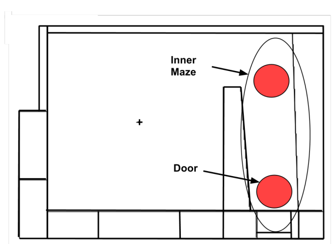

(a) Position of bubble detectors: inner maze and door.

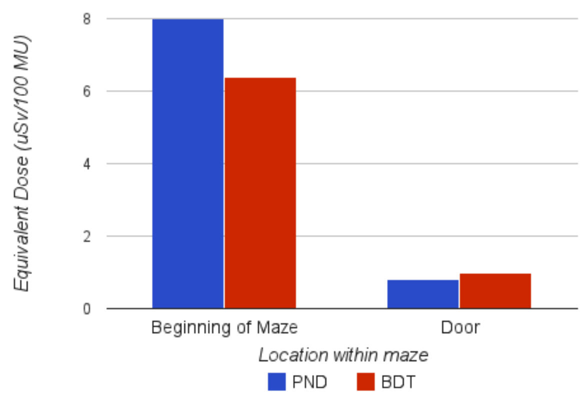

(b) Equivalent dose (uSv/100MU) detected from 2 types of bubble detectors placed at beginning and end of maze.

Figure 4–17: PND and BDT bubble detectors placed in the maze: note the expected higher sensitivity of the PND at the beginning of the maze. This trend is reversed near the door. Although a large number of MUs was delivered, equivalent dose was normalized to 100 MU.

Chapter 5
Conclusion and future work

This work began with a review of photoneutron physics in the context of radiation therapy. This was followed by a summary of neutron shielding techniques used in the context of radiotherapy. Analytical models as well as numerical approaches were presented and our approach to Monte-Carlo simulations of photoneutron shielding was detailed.

Neutrons being a potentially harmful byproduct of radiotherapy treatments, their impact on the health of the clinical personnel, and eventually the patient, must be reduced as much as possible following the ALARA principle (as low as reasonably achievable). In large part, maze design aims to reach this goal in the most reasonable and effective manner while accounting for architectural, logistical, and financial constraints. Ever increasing computational power and recent breakthroughs in variance reduction techniques have turned MC from a tool used by research groups into a mainstream phenomenon that is becoming ubiquitous in academia and progressively in the clinic.

The well known MC code MCNP5 was used to simulate transport of photoneutrons in radiotherapy bunkers with a special emphasis on the maze area. Radiotherapy bunker models were reproduced from existing rooms at the MUHC or inspired from modern doorless bunker models. The source of neutrons was modelled as a combination of an existing analytical photoneutron spectrum and a 10 cm radius sphere of tungsten, which partially mimics the role of the linac head and smoothes the point source photoneutron spectrum.

Simulations were performed using the next event estimator variance reduction technique and 20 million particle histories, which yielded results that had all associated uncertainties under 0.8%. The maze was studied in terms of fluence and dose rate (Sv/h) at different locations. Design features such as the presence of a door, the role of the maze, the impact of Borated Polyethylene or of bulkheads in the inner maze passage were assessed and results presented in the form of graphs and tables. In general, it was shown that each additional design feature could contribute to the reduction of photoneutron dose at the bunker entrance. Indeed, modern mazes with borated polyethylene, a bulkhead, and a second leg can potentially reduce dose by orders of magnitude if compared to conventional mazes with a more conservative design.

Although physical measurements were attempted using bubble detectors and a neutron spectrometer, results were inconclusive because of technical obstacles. The spectrometer that can be used with the pulsed mode of the linac must be a non-active type in order to avoid being subjected to pulse pile-up. Bubble detector results, on the other hand, are associated with high uncertainties introduced during the counting process of large numbers of bubbles necessary to have statistically meaningful results. It was therefore not possible to present meaningful results pertaining to spectral measurements. Limited qualitative results were presented for bubble detectors, which were tested for functionality and detection of trends only.

It must nevertheless be mentioned that this part of the project to which we dedicated the first five months was very instructive in our understanding of neutron physics. Indeed, now that this master's project has drawn to an end, the collaboration - far from having ended - has continued and extended to the use of modern spectrometers built in Canada [93].

This work proved that MC simulations can be an accessible and relatively user-friendly bunker design tool for medical physicists, gradually replacing - or at the very least complementing - existing analytical equations that have been used for decades. Future steps may include continuation of physical measurements with modern equipment as well as refining the MC code to make it more user friendly and flexible in reproducing bunker geometry.

Bibliography

[1] Canadian Cancer Society. Canadian cancer statistics, 2012. URL `www.cancer.ca/statistics`.

[2] Larry F. Ellison and Kathryn Wilkins. Canadian trends in cancer prevalence. *Health Rep*, 23(1):7–16, Mar 2012.

[3] National cancer institute, 2012. URL `www.cancer.gov`.

[4] Faiz M. Khan. *The physics of radiation therapy*. Lippincott Williams & Wilkins, Philadelphia, 4th ed edition, 2010. ISBN 9780781788564.

[5] NCRP. *Structural shielding design and evaluation for megavoltage X- and gamma-ray radiotherapy facilities: recommendations of the National Council on Radiation Protection and Measurements*, volume no. 151. National Council on Radiation Protection and Measurements, Bethesda, MD, 2005. ISBN 0929600878.

[6] Patton H. McGinley. *Shielding techniques for radiation oncology facilities*. Medical Physics Pub., Madison, Wis., 2nd ed edition, 2002. ISBN 1930524072.

[7] A. Facure, A. X. Da Silva, and R. C. Falcao. Monte carlo simulation of scattered and thermal photoneutron fluences inside a radiotherapy room. *Radiation Protection Dosimetry*, 123(1):56–61, 2007. doi: DOI10.1093/rpd/ncl1080.

[8] Frank H. Attix. *Introduction to radiological physics and radiation dosimetry*. Wiley, New York, 1986. ISBN 0471011460. URL `http://www.loc.gov/catdir/description/wiley031/86013222.html`.

[9] J. E. Turner. *Atoms, radiation, and radiation protection.* Wiley-VCH, Weinheim, 3rd completely rev. and enl. ed edition, 2007. ISBN 9783527406067 (Talk. paper). URL `http://www.loc.gov/catdir/enhancements/fy0814/2007476027-b.html`.

[10] John Kildea. Health physics for medical physicists. Class Notes - McGill University, September 2010.

[11] R. E. Rowland. *Radium in humans: a review of U.S. studies.* Argonne National Laboratory, Argonne, Ill., 1995.

[12] Kreuzer M., Walsh L., Schnelzer A., Tschense A., and Grosche B. Radon and risk of extrapulmonary cancers: results of the german uranium miners' cohort study, 1960–2003. *British Journal of Cancer - BJC*, 99:1946–1953, November 2008.

[13] Stalberg K., Haglund B., Axelsson O., Cnattingius S., Pfeifer S., and Kieler H. Prenatal x-ray exposure and childhood brain tumours: a population-based case–control study on tumour subtypes. *British Journal of Cancer - BJC*, 97:1583–1587, October 2007.

[14] Richard Doll. Hazards of ionizing radiation: 100 years of observations on man. *British Journal of Cancer - BJC*, 72:1339–1349, August 1995.

[15] Izumi S., Koyama K., Soda M., and Suyama A. Cancer incidence in children and young adults did not increase relative to parental exposure to atomic bombs. *British Journal of Cancer - BJC*, 89:1709–1713, October 2003.

[16] *Sources and effects of ionizing radiation: United Nations Scientific Committee on the Effects of Atomic Radiation : UNSCEAR 2008 report to the General Assembly, with scientific annexes.* United Nations, New York, 2010. ISBN 9789211422740 (v. 1).

[17] A. D. da Cruz, J. P. Volpe, V. Saddi, J. Curry, M. P. Curadoc, and B. W. Glickman. Radiation risk estimation in human populations: lessons from the radiological accident in brazil. *Mutat Res*, 373(2):207–14, Feb 1997.

[18] Radiation Primer (Baylor College of Medicine), 2007. URL `http://www.bcm.edu/bodycomplab/mainbodycomp.htm`.

[19] Ministry of Justice (Canada). Radiation protection regulations, September 2007. URL `http://laws-lois.justice.gc.ca/eng/regulations/sor-2000-203/`.

[20] CNSC webpage. URL `http://www.cnsc-ccsn.gc.ca`.

[21] Glenn F. Knoll. *Radiation detection and measurement*. John Wiley, Hoboken, N.J., 4th ed edition, 2010. ISBN 9780470131480 (hardback). URL `http://catalogimages.wiley.com/images/db/jimages/9780470131480.jpg`.

[22] E. B Podgoršak. *Radiation physics for medical physicists*. Biological and medical physics, biomedical engineering. Springer, Heidelberg, 2nd, enl. ed edition, 2010.

[23] *Quantities and units in radiation protection dosimetry*, volume 51. International Commission on Radiation Units and Measurements, Bethesda, Md., 1993. ISBN 0913394505.

[24] *1990 recommendations of the International Commission on Radiological Protection: user's edition*. Published for the International Commission on Radiological Protection by Pergamon Press, Oxford, 1st ed edition, 1992. ISBN 0080419984.

[25] Zhenzhou Liu and Jinxiang Chen. New calculations of neutron kerma coefficients and dose equivalent. *J. Radiol. Prot.*, 28(2):185–93, Jun 2008. doi: 10.1088/0952-4746/28/2/002.

[26] *Neutron contamination from medical electron accelerators: recommendations of the National Council on Radiation Protection and Measurements*, volume no. 79. The Council, Bethesda, Md., 1984. ISBN 0913392707 (pbk.).

[27] R. Montalbetti, L. Katz, and J. Goldemberg. Photoneutron cross sections. *Phys. Rev.*, 91:659–673, Aug 1953. doi: 10.1103/PhysRev.91.659. URL `http://link.aps.org/doi/10.1103/PhysRev.91.659`.

[28] ICRP. Conversion coefficients for use in radiological protection against external radiation. Adopted by the ICRP and ICRU in September 1995. *Ann. ICRP*, 26(3-4):1–205, 1996.

[29] G. Tosi, A. Torresin, S. Agosteo, A. F. Para, V. Sangiust, L. Zeni, and M. Silari. Neutron measurements around medical electron accelerators by active and passive detection techniques. *Medical Physics*, 18(1):54–60, Jan-Feb 1991.

[30] A. Facure, R. C. Falcao, A. X. Da Silva, and V. R. Crispim. Neutron dose rate evaluation for medical linear accelerators. *Radiation Protection Dosimetry*, 111(1):101–103, 2004. doi: DOI10.1093/rpd/nch369.

[31] A. Facure, R. C. Falcão, A. X. Silva, V. R. Crispim, and J. C. Vitorelli. A study of neutron spectra from medical linear accelerators. *Appl. Radiat. Isot.*, 62(1):69–72, Jan 2005. doi: 10.1016/j.apradiso.2004.05.072.

[32] Mansour Zabihzadeh, Mohammad Reza Ay, Mahmoud Allahverdi, Asghar Mesbahi, Seyed Rabee Mahdavi, and Majid Shahriari. Monte-Carlo estimation of photoneutrons contamination from high-energy X-ray medical accelerators in treatment room and maze: a simplified model. *Radiation Protection Dosimetry*, 135(1):21–32, July 2009. doi: DOI10.1093/rpd/ncp097.

[33] Richard C. McCall and William P. Swanson. Neutron sources and their characteristics. *Publication from SLAC (Stanford Linear Accelerator Center)*, 1979.

[34] E. B. Podgoršak. *Radiation oncology physics: a handbook for teachers and students*. International Atomic Energy Agency, Vienna, 2005. ISBN 9201073046.

[35] AAPM Radiation Therapy Committee. Task Group 27 and American Institute of Physics. *Neutron Measurements Around High Energy X-ray Radiotherapy Machines: A Report of Task Group 27, Radiation Therapy Committee, American Association of Physicists in Medicine*. AAPM report. American Association of Physicists in Medicine, 1987. ISBN 9780883185186. URL `http://books.google.ca/books?id=rrm7AAAACAAJ`.

[36] R. C. McCall, T. M. Jenkins, and R. A. Shore. Transport of accelerator produced neutrons in a concrete room. *IEEE Transactions On Nuclear Science*, 26(1):1593–1602, 1979.

[37] Doug Reilly, Norbert Ensslin, and Hastings Smith. *Passive Nondestructive Assay Of Nuclear Materials*. The Commission, Washington, DC, 1991.

[38] Doug Sim. Proportional counters. URL `http://en.wikipedia.org/wiki/Proportional_counter`.

[39] S.S. Desai and A.M. Shaikh. On studies of Helium-3 and isobutane mixture as neutron proportional counter gas. *Nuclear Instruments and Methods in Physics Research Section A: Accelerators, Spectrometers, Detectors and Associated Equipment*, 557(2):607 – 614, 2006. ISSN 0168-9002. doi: 10.1016/j.nima.2005.11.182. URL `http://www.sciencedirect.com/science/article/pii/S0168900205023156`.

[40] E. Dietz, M. Matzke, W. Sosaat, G. Urbach, and M. Weyrauch. Neutron response of an Helium-3 proportional counter. *Nuclear Instruments and Methods in Physics Research Section A: Accelerators, Spectrometers, Detectors and Associated Equipment*, 332(3):521 – 528, 1993. ISSN 0168-9002. doi: 10.1016/0168-9002(93)90309-6. URL `http://www.sciencedirect.com/science/article/pii/0168900293903096`.

[41] William C. Sailor, Stanley G. Prussin, and Mark S. Derzon. Monte-Carlo calculation of the response function for a Helium-3 neutron spectrometer. *Nuclear Instruments and Methods in Physics Research Section A: Accelerators, Spectrometers, Detectors and Associated Equipment*, 270:527 – 536, 1988. ISSN 0168-9002. doi: 10.1016/0168-9002(88)90726-7. URL `http://www.sciencedirect.com/science/article/pii/0168900288907267`.

[42] S. Shalev, Z. Fishelson, and J. M. Cuttler. The wall effect in Helium-3 counters. *Nuclear Instruments and Methods*, 71(3):292 – 296, 1969. ISSN 0029-554X. doi: 10.1016/0029-554X(69)90317-6. URL `http://www.sciencedirect.com/science/article/pii/0029554X69903176`.

[43] T. Iguchi, N. Nakayamada, H. Takahashi, and M. Nakazawa. Neutron spectrometry using a Helium-3 gas ionization chamber. *Nuclear Instruments and Methods in Physics Research Section A: Accelerators, Spectrometers, Detectors and Associated Equipment*, 353:152 – 155, 1994. ISSN 0168-9002. doi: 10.1016/0168-9002(94)91625-X. URL `http://www.sciencedirect.com/science/article/pii/016890029491625X`.

[44] Richard L. Bramblett, Ronald I. Ewing, and T.W. Bonner. A new type of neutron spectrometer. *Nuclear Instruments and Methods*, 9 (1):1 – 12, 1960. ISSN 0029-554X. doi: 10.1016/0029-554X(60) 90043-4. URL `http://www.sciencedirect.com/science/article/pii/0029554X60900434`.

[45] R. Bedogni. Neutron spectrometry with bonner spheres for area monitoring in particle accelerators. *Radiat. Prot. Dosimetry*, 146(4):383–94, 2011.

[46] F. D. Brooks and H. Klein. Neutron spectrometry - historical review and present status. *Nuclear Instruments and Methods in Physics Research Section A: Accelerators, Spectrometers, Detectors and Associated Equipment*, 476:1 – 11, 2002. ISSN 0168-9002. doi: 10.1016/S0168-9002(01)01378-X. Int. Workshop on Neutron Field Spectrometry in Science, Technology and Radiation Protection.

[47] Vladimir Mares and Hans Schraube. Improved response matrices of Bonner sphere spectrometers with lithium iodine scintillation detector and Helium-3 proportional counter between 15 and 100 MeV. *Nuclear Instruments and Methods in Physics Research Section A: Accelerators, Spectrometers, Detectors and Associated Equipment*, 366(1):203 – 206, 1995. ISSN 0168-9002. doi: 10.1016/0168-9002(95)00555-2. URL `http://www.sciencedirect.com/science/article/pii/0168900295005552`.

[48] P. H. McGinley and M. S. Miner. A history of radiation shielding of x-ray therapy rooms. *Health Phys*, 69(5):759–65, Nov. 1995.

[49] Benjamin R. Archer. Recent history of the shielding of medical x-ray imaging facilities. *Health Phys*, 88(6):579–86, Jun. 2005.

[50] William Herbert Rollins. *Notes on X-light.* Boston, Mass., 1903.

[51] *Handbook, Bureau of Standards.* U.S. G.P.O., Washington, 1934.

[52] *NCRP report.* 1951-1966: National Bureau of Standards handbook. U.S. Dept. of Commerce, National Bureau of Standards, Washington, D.C.

[53] *Structural shielding design and evaluation for medical use of X-rays and gamma rays of energies up to 10 MeV: recommendations of the National Council on Radiation Protection and Measurements.* NCRP report ; no.

49. The Council, Washington, 1976. ISBN 0913392316.

[54] *Radiation protection design guidelines for 0.1-100 MeV particle accelerator facilities: recommendations of the National Council on Radiation Protection and Measurements*. NCRP report ; no. 51. The Council, Washington, 1977. ISBN 0913392332.

[55] *Radiation protection for particle accelerator facilities: recommendations of the National Council on Radiation Protection and Measurements*, volume no. 144. National Council on Radiation Protection and Measurements, Bethesda, Md., 2003. ISBN 0929600770.

[56] IAEA. *Radiation protection in the design of radiotherapy facilities*. IAEA report ; no. 47. International Atomic Energy Agency (IAEA), 2006.

[57] E. Tochilin and P. D. Lariviere. Attenuation of Primary and Leakage Radiation in Concrete For X-rays From a 10 MV Linear Accelerator. *Health Physics*, 36(3), 1979.

[58] Patton H. McGinley and K. E. Hufmann. Photon and neutron dose equivalent in the maze of a high-energy medical accelerator facility. *Radiation Protection Management*, 5(6):20 – 23, 2000.

[59] RC McCall, PH McGinley, and KE Huffman. Room scattered neutrons. *Medical Physics*, 26(2):206–207, February 1999.

[60] David S. Followill, Marilyn S. Stovall, Stephen F. Kry, and Geoffrey S. Ibbott. Neutron source strength measurements for Varian, Siemens, Elekta, and General Electric linear accelerators. *J. Appl. Clin. Med. Phys.*, 4(3): 189–94, 2003. doi: 10.1120/1.1571671.

[61] X. S. Mao, K. R. Kase, J. C. Liu, W. R. Nelson, J. H. Kleck, and S. Johnsen. Neutron sources in the Varian Clinac 2100C/2300C medical accelerator calculated by the EGS4 code. *Health Phys*, 72(4):524–529, Apr 1997.

[62] K. R. Kase, X. S. Mao, W. R. Nelson, J. C. Liu, J. H. Kleck, and M. Elsalim. Neutron fluence and energy spectra around the Varian Clinac 2100C/2300C medical accelerator. *Health Phys*, 74(1):38–47, Jan 1998.

[63] P. H. McGinley and E. K. Butker. Evaluation of neutron dose equivalent levels at the maze entrance of medical accelerator treatment rooms. *Medical Physics*, 18(2):279–281, Mar-Apr 1991.

[64] R.E. Maerker, F.J. Muckenthaler, and OAK RIDGE NATIONAL LAB TENN. *Neutron Fluxes in Concrete Ducts Due to Incident Epicadmium Neutrons: Calculations and Experiments*. Oak Ridge National Laboratory, 1967.

[65] Kersey R. W. Estimation of neutron and gamma radiation doses in the entrance mazes of SL75-20 linear accelerator treatment rooms. *Medicamundi*, 24(3):151–155, 1979.

[66] Raymond K. Wu and Patton H. McGinley. Neutron and capture gamma along the mazes of linear accelerator vaults. *J Appl Clin Med Phys*, 4(2): 162–71, 2003. doi: 10.1120/1.1561954.

[67] R. C. McCall. Shielding for thermal neutrons. *Med Phys*, 24(1):135–6, Jan 1997.

[68] Frank Verhaegen and Jan Seuntjens. Monte-Carlo modelling of external radiotherapy photon beams. *Phys Med Biol*, 48(21):R107–64, Nov 2003.

[69] D. M. Lovelock, C. S. Chui, and R. Mohan. A Monte-Carlo model of photon beams used in radiation therapy. *Med Phys*, 22(9):1387–94, Sep 1995.

[70] C. M. Ma, E. Mok, A. Kapur, T. Pawlicki, D. Findley, S. Brain, K. Forster, and A. L. Boyer. Clinical implementation of a Monte-Carlo treatment planning system. *Med Phys*, 26(10):2133–2143, Oct 1999.

[71] C. M. Ma, J. S. Li, T. Pawlicki, S. B. Jiang, J. Deng, M. C. Lee, T. Koumrian, M. Luxton, and S. Brain. A Monte-Carlo dose calculation tool for radiotherapy treatment planning. *Phys Med Biol*, 47(10):1671–89, May 2002.

[72] Rebecca M. Howell, Stephen F. Kry, Eric Burgett, Nolan E. Hertel, and David S. Followill. Secondary neutron spectra from modern Varian, Siemens, and Elekta linacs with multileaf collimators. *Med Phys*, 36 (9):4027–38, Sep 2009.

[73] R. A. Forster, L. J. Cox, R. F. Barrett, T. E. Booth, J. F. Briesmeister, F. B. Brown, J. S. Bull, G. C. Geisler, J. T. Goorley, R. D. Mosteller, S. E. Post, R. E. Prael, E. C. Selcow, and A. Sood. MCNP Version 5. *Nuclear Instruments and Methods in Physics Research B*, 213:82–86, January 2004. doi: 10.1016/S0168-583X(03)01538-6.

[74] C. Ongaro, J. Rodenas, A. Leon, J. Perez, A. Zanini, et al. Monte-Carlo simulation and experimental evaluation of photoneutron spectra produced in medical linear accelerators. pages 2531–2533, 1999.

[75] C. Ongaro, A. Zanini, U. Nastasi, J. Ródenas, G. Ottaviano, C. Manfredotti, and K. W. Burn. Analysis of photoneutron spectra produced in medical accelerators. *Phys Med Biol*, 45(12):L55–61, Dec 2000.

[76] S. Agosteo, A. Foglio Para, and B. Maggioni. Neutron fluxes in radiotherapy rooms. *Med Phys*, 20(2 Pt 1):407–14, 1993.

[77] Omar Chibani and Chang-Ming Charlie Ma. Photonuclear dose calculations for high-energy photon beams from Siemens and Varian linacs. *Med Phys*, 30(8):1990–2000, Aug 2003.

[78] Rebecca M. Howell, Michele S. Ferenci, Nolan E. Hertel, and Gary D. Fullerton. Investigation of Secondary Neutron Dose for 18 MV Dynamic MLC IMRT Delivery. *Med Phys*, 32(3):786–93, Mar 2005.

[79] R. Barquero, R. Mendez, H. R. Vega-Carrillo, M. P. Iniguez, and T. M. Edwards. Neutron spectra and dosimetric features around an 18 MV linac accelerator. *Health Phys*, 88(1):48–58, Jan 2005.

[80] M. K. Saeed, O. Moustafa, O. A. Yasin, C. Tuniz, and F. I. Habbani. Doses to patients from photoneutrons emitted in a medical linear accelerator. *Radiation Protection Dosimetry*, 133(3):130–135, February 2009. doi: DOI10.1093/rpd/ncp029.

[81] J. Pena, L. Franco, F. Gómez, A. Iglesias, J. Pardo, and M. Pombar. Monte Carlo study of Siemens PRIMUS photoneutron production. *Phys Med Biol*, 50(24):5921–33, Dec 2005. doi: 10.1088/0031-9155/50/24/011.

[82] E. Carinou, V. Kamenopoulou, and I. E. Stamatelatos. Evaluation of neutron dose in the maze of medical electron accelerators. *Med Phys*, 26 (12):2520–5, Dec 1999.

[83] Xudong Wang, Carlos Esquivel, Elena Nes, Chengyu Shi, Nikos Papanikolaou, and Michael Charlton. The neutron dose equivalent evaluation and shielding at the maze entrance of a Varian Clinac 23EX treatment room. *Med Phys*, 38(3):1141–1149, Mar 2011.

[84] Stephen F. Kry, Jennifer L. Johnson, R. Allen White, Rebecca M. Howell, Rajat J. Kudchadker, and Michael T. Gillin. Neutron-induced electronic failures around a high-energy linear accelerator. *Med Phys*, 38(1):34–9, Jan 2011.

[85] Clifford Dugal. Application of Monte-Carlo to Linac Bunker Shielding Design. Master's thesis, Carleton University, 2006.

[86] R. A. Schwarz and L. L. Carter. The visual creation and display of MCNP geometries and lattices for criticality problems. *Transactions of the American Nuclear Society*, 80:162, 1999.

[87] X-5 Monte Carlo Team. *MCNP5 - A general Monte Carlo N-Particle transport code, version 5*. Los Alamos National Laboratory, Los Alamos, New Mexico, 2003.

[88] A. Facure and W. F. Franca. Optimal shielding design for bunkers of compact cyclotrons used in the production of medical radionuclides. *Medical Physics*, 37(12):6332–6337, December 2010. doi: DOI10.1118/1.3515458.

[89] John Kildea. An evaluation of NCRP report 151 - radiation shielding design for radiotherapy facilities, and a feasibility study for 6 MV open-door treatments in an existing high-energy radiation therapy bunker. Master's thesis, McGill University, 2010.

[90] Asghar Mesbahi, Hosein Ghiasi, and Seyed Rabee Mahdavi. Photoneutron and capture gamma dose equivalent for different room and maze layouts in radiation therapy. *Radiation Protection Dosimetry*, 140(3): 242–249, August 2010. doi: DOI10.1093/rpd/ncp303.

[91] H. Ing, R. A. Noulty, and T. D. McLean. Bubble detectors - a maturing technology. *Radiation Measurements*, 27(1):1–11, February 1997.

[92] L. Bourgois, D. Delacroix, and A. Ostrowsky. Use of bubble detectors to measure neutron contamination of a medical accelerator photon beam. *Radiation Protection Dosimetry*, 74(4):239–246, 1997.

[93] Detec Radiation. URL `http://www.detec-rad.com/`.